# Université de Lille

Doctoral School **ED Régionale ENGSYS-632**

University Department **IEMN**

Thesis defended by **Anna IPATOVA**

Defended on **February 7, 2023**

In order to become Doctor from Université de Lille

Academic Field **Physique**

Speciality **Acoustique**

# Detachment of immersed microparticles and the collective dynamics of microspheres in evaporating droplets

**Thesis supervised by**   Farzam ZOUESHTIAGH   Supervisor
Alexis DUCHESNE   Co-Monitor

**Committee members**

| | | |
|---|---|---|
| *Committee President* | Elise LORENCEAU | |
| *Referees* | Elise LORENCEAU | Senior Researcher at Université Grenoble Alpes |
| | Mickaël ANTONI | Professor at Aix-Marseille Université |
| *Examiners* | Anne LE GOFF | Associate Professor at Université de Technologie de Compiègne |
| | Benjamin SOBAC | Junior Researcher at Université de Pau et des Pays de l'Adour |
| *Guests* | Christine FAILLE | Senior Researcher at Université de Lille |
| | Harunori YOSHIKAWA | Associate Professor at Université Côte d'Azur |
| *Supervisors* | Farzam ZOUESHTIAGH | Professor at Université de Lille |
| | Alexis DUCHESNE | Associate Professor at Université de Lille |

# Université de Lille

Doctoral School **ED Régionale ENGSYS-632**

University Department **IEMN**

Thesis defended by **Anna IPATOVA**

Defended on **February 7, 2023**

In order to become Doctor from Université de Lille

Academic Field **Physique**

Speciality **Acoustique**

## Detachment of immersed microparticles and the collective dynamics of microspheres in evaporating droplets

| **Thesis supervised by** | Farzam ZOUESHTIAGH | Supervisor |
|---|---|---|
| | Alexis DUCHESNE | Co-Monitor |

**Committee members**

| | | |
|---|---|---|
| *Committee President* | Elise LORENCEAU | |
| *Referees* | Elise LORENCEAU | Senior Researcher at Université Grenoble Alpes |
| | Mickaël ANTONI | Professor at Aix-Marseille Université |
| *Examiners* | Anne LE GOFF | Associate Professor at Université de Technologie de Compiègne |
| | Benjamin SOBAC | Junior Researcher at Université de Pau et des Pays de l'Adour |
| *Guests* | Christine FAILLE | Senior Researcher at Université de Lille |
| | Harunori YOSHIKAWA | Associate Professor at Université Côte d'Azur |
| *Supervisors* | Farzam ZOUESHTIAGH | Professor at Université de Lille |
| | Alexis DUCHESNE | Associate Professor at Université de Lille |

# Université de Lille

École doctorale **ED Régionale ENGSYS-632**

Unité de recherche **IEMN**

Thèse présentée par **Anna IPATOVA**

Soutenue le **7 février 2023**

En vue de l'obtention du grade de docteur de l'Université de Lille

Discipline **Physics**

Spécialité **Acoustics**

<div style="border:1px solid">

# Décrochement de microparticules immergées et dynamique collective de microsphères dans une goutte en évaporation

</div>

| **Thèse dirigée par** | Farzam ZOUESHTIAGH | directeur |
|---|---|---|
| | Alexis DUCHESNE | co-encadrant |

**Composition du jury**

| | | |
|---|---|---|
| *présidente du jury* | Elise LORENCEAU | |
| *Rapporteurs* | Elise LORENCEAU | directrice de recherche à l'Université Grenoble Alpes |
| | Mickaël ANTONI | professeur à l'Aix-Marseille Université |
| *Examinateurs* | Anne LE GOFF | MCF à l'Université de Technologie de Compiègne |
| | Benjamin SOBAC | chargé de recherche à l'Université de Pau et des Pays de l'Adour |
| *Invités* | Christine FAILLE | directrice de recherche à l'Université de Lille |
| | Harunori YOSHIKAWA | MCF à l'Université Côte d'Azur |
| *Directeurs de thèse* | Farzam ZOUESHTIAGH | professeur à l'Université de Lille |
| | Alexis DUCHESNE | MCF à l'Université de Lille |

This thesis has been prepared at Institut d'Électronique, de Microéléctronique et de Nanotechnologie:

**IEMN**

Cité Scientifique
Avenue Henri Poincaré
CS 60069
59 652 Villeneuve d'Ascq Cedex
France

☎         +33 (0)3 20 19 79 79
✉         accueil@iemn.fr
Web Site   https://www.iemn.fr/

**Detachment of immersed microparticles and the collective dynamics of microspheres in evaporating droplets**

**Abstract**

Dirts or microparticles are usually small enough to be invisible to the naked eye, but their effects may be substantial in our daily life. For instance, their presence is often undesirable in various domains such as in food industries where they may act as polluting agents or in microelectronics where they can be a source of faulty microfabrication.

In the first part of this thesis, we investigate experimentally the dependence of particle adhesion on time and temperature using a patch-clamp technique. The widely used adhesion models do not match our experimental data proving that the models are limited to a certain range of experimental conditions. Furthermore, we speculate on the presence of an air bubble underneath the immersed particle that could modify the measured force required to detach the particle from its substrate. To confirm this hypothesis, we undertook numerical and experimental studies of the effect of such a trapped bubble. The bubble-induced force is studied to understand if the bubble facilitates or opposes the particle removal. The results are supported by experiments which demonstrate the presence of a trapped bubble when at least one of the involved surface, particle or substrate, is hydrophobic.

The second part of this thesis is devoted to the collective dynamics of particles contained in an evaporating droplet. We established a specific protocol based on steps reported in literature, and observed a variety of patterns. We identify five possible modes of the contact line motion leading to the formation of these patterns. Among these, a new fingering-like pattern referred to as "braids" is discovered.

**Keywords:** contact line, microparticles, detachment force, patch-clamp, drying, coffee-stain

**Décrochement de microparticules immergées et dynamique collective de microsphères dans une goutte en évaporation**

**Résumé**

Les objets micrométriques sont généralement suffisamment petits pour qu'on puisse les distinguer à l'œil nu, mais leurs effets indésirables peuvent être majeurs dans notre vie quotidienne. Par exemple, dans l'industrie agroalimentaire, des bactéries micrométriques sont une source de contamination tandis que dans l'industrie microélectronique la présence de toute poussière peut provoquer un défaut dans la microfabrication.

Dans la première partie de ce manuscrit, on étudie expérimentalement l'adhésion sur un substrat de microparticules initialement contenues dans une gouttelette. Cette étude s'intéresse aux effets de conditions de séchage telles que la durée et la température sur cette adhésion. En utilisant la technique de patch-clamp, nous avons mesuré les forces requises pour détacher des microparticules de leurs substrats. Nous avons ensuite comparé nos résultats expérimentaux avec des modèles théoriques existants et avons constaté des différences substantielles. Nous avons associé ces différences à la présence de bulles d'air qui auraient été piégées sous les microparticules lors de leurs immersions avant les mesures en patch-clamp. Afin de confirmer cette hypothèse, nous avons développé un modèle numérique pour estimer la force exercée par de telles bulles sur les particules. Des expériences menées en complément aux résultats numériques sont venues ensuite confirmer la présence de bulles piégées lorsqu'au moins une des deux surfaces, celle de la particule ou de son substrat, est hydrophobe.

Dans la deuxième partie du manuscrit, nous nous intéressons à la dynamique collective des particules contenues dans une goutte en état d'évaporation. Pour cela nous établissons d'abord un protocole expérimental spécifique en nous basant sur ceux proposés dans la littérature. En suivant ce protocole, plusieurs patterns ont été observés que nous avons associé à cinq modes de mouvement de la ligne de contact. Parmi ces patterns, on distingue un relevant du type "fingering", que l'on nomme "braids" et qui n'avait jamais été rapporté dans la littérature.

**Mots clés :** ligne de contact, microparticules, force de décrochement, patch-clamp, séchage, tâche de café

# Acknowledgments

# Table of contents

# List of Tables

# List of Figures

# Introduction

Dust, dirt, or bacteria are common micron-sized objects that are parts of our life environment and are usually hard to circumvent. Despite the small size, their presence is often undesirable since they are usually considered as a source of pollution. For instance, in food industries, micron-sized bacteria and spores are at the origin of food contamination, whereas in microelectronics, the presence of dust can induce faulty microfabrication. Their removal is, therefore, of primary importance in various domains of applications and has yet to undergo technological improvements in order to reduce energy and water/detergent consumptions.

In this work, we attempt to address some of the issues associated with the removal of spores of bacteria in the food industry. To date, hot water with detergents is primarily used to clean surfaces subjected to contamination by microorganisms (Fig. 1), for instance, milk production lines. After this first cleaning, the surfaces should be washed again to remove the residual chemicals, which makes this procedure energy- and water-consuming and requires technological solutions to reduce the environmental impact.
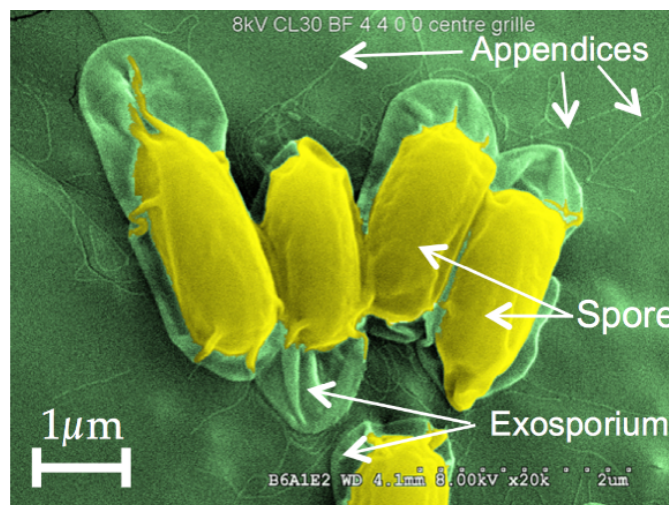


Figure 1: *Bacillus cereus* spores. Photo from Christine Faille.

To this end, and in order to simplify the complex wall-spore interactions on a contaminated surface, we mainly focus our study on the ideal case of a microparticle deposited on a substrate. This drastic simplification enabled us to have better control over the wetting properties of the tested particles and substrates. It also enabled us to work on simplified theoretical and numerical models that could bring physical understating of a real system.

In the first part of the thesis, we will focus on the interaction of a particle with a surface. In Chapter 2, we will use an adapted patch-clamp technique to measure the force required to detach a microparticle that was previously deposited on a substrate by means of an evaporating droplet. We particularly investigate the dependency of this force with respect to drying conditions (temperature and duration) of the droplet that lead to particle emplacement on the substrate. Despite some trends observed for the detachment force with the drying conditions, the results appear at odds with existing theoretical models from the literature. We attribute this discrepancy to the presence of an air bubble that would have been trapped below the immersed particle prior to our measurements. In order to verify this hypothesis, we quantify the effect of such bubbles using a numerical model in Chapter 3. The results show that such a situation can lead to the retention or the repulsion of the particle from the substrate and, consequently, modify the measured detachment force. The findings are then supported by companion experiments that demonstrate the presence of a trapped bubble when at least one of the involved surfaces, particle or substrate, is hydrophobic.

In the second part of this thesis, we will investigate the collective dynamics of particles contained in an evaporating droplet. While trying to reproduce the classical coffee-stain patterns, we notice in the literature the absence of a common experimental protocol for substrate preparation, suspension mixing, or drop deposition. In Chapter 5, we establish our own specific protocol by selecting the best solution for each step reported in the literature. Surprisingly, we observe a variety of patterns developing under an identical protocol. In Chapter 6, we carry out careful observations of different stages of developing patterns under the moving contact line of the evaporating droplet. We identify five possible modes of the contact line motion leading to the formation of these patterns. Among them, a new fingering-like pattern referred to as "braids" is discovered.

# Part I

# Detachment of immersed microparticles

# Chapter 1

# State of the art

Surface contamination by micron-sized particles is a major challenge that begs technological solutions in various domains from microtechnology [114, 161, 30, 18], automotive [160, 12] to food [103, 7, 170, 25] industries. Understanding the mechanisms of particle-surface interaction is the key to effective surface cleaning.

This chapter describes the previous works about the particle-substrate interaction. In the first part of this chapter, we present the classical models for particle adhesion that relate the adhesion force to the radius of the contact zone. In the second part, we show the existing methods for the adhesion force measurement. Lastly, we discuss these methods and introduce our hypothesis about the air bubble trapping under a particle.

## 1.1 Particle-substrate interactions

When a particle comes into contact with a substrate, one or both of the materials can deform. This deformation arises from [18] (i) long-range attractive interactions, such as van der Waals forces (will be detailed below), electrostatic forces (bulk excess charge image forces and electrical double layer forces) and magnetic attractions, which act to bring the particle to the substrate and establish the contact area (ii) other forces which, along with the forces from the first group, establish the contact area (e.g., liquid bridges, external applied load), and (iii) short-range interactions which can add to adhesion only after the establishment of an adhesive contact area (e.g., chemical bonds).

In the current work, we will be particularly interested in a particle under the effect of the long-range attractive interactions and the external applied load. It was shown that van der Waals forces dominate over electrostatic ones for particles smaller than about 50 µm in diameter, and vice versa for particles greater than about 50 µm in diameter [18]. Throughout this work, the particles in consideration are of 1 µm to 12 µm in diameter, so that the long-range interactions are dominated by the van der Waals forces.

**Van der Waals forces**

Van der Waals forces are caused by spontaneous electrical and magnetic polarizations when surfaces are positioned sufficiently close together. The polarizations develop a fluctuating electromagnetic field that is generally attractive in nature, yielding the van der Waals forces [39].

Van der Waals forces include three types of interactions [120]: (i) Keesom force between two permanent dipoles, (ii) Debye force between a permanent dipole and a corresponding *induced dipole*, and (iii) London dispersion force between two *instantaneous* dipoles. An instantaneous dipole occurs due to Heisenberg's Uncertainty Principle that suggests the always non-zero energy of electrons, since they are constantly moving around their orbital. Moreover, according to the Schrödinger equation for an electron in a closed space (well-known problem of a particle in a box), it is probable to find the electron anywhere in the orbital of the atom. Since all electrons are constantly moving in atom, at some moment of time, it is likely to have more electrons on one side of the atom than from the other (Fig. 1.1, a). This is how **instantaneous** (or spontaneous) **dipoles** occur. As these electrons are continuing to constantly move, the positive and negative poles are not fixed and can alter. When a dipole (instantaneous or permanent) approaches a neutral polarizable atom (i.e., capable to acquire an electric dipole moment when subjected to an electric field), it can cause the atom to also produce dipoles (Fig. 1.1, b). The originally neutral atom is then considered as an **induced dipole**.
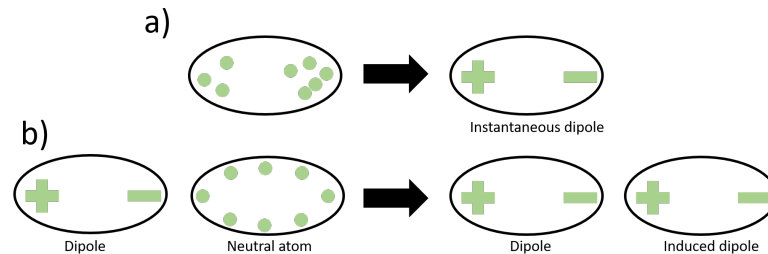


Figure 1.1: Atom (black oval) with electrons (green dots). The positive or negative signs represent local charge. (a) Formation of instantaneous dipole due to nonuniform electron distribution in atom. (b) Dipole induces dipole to a neutral atom.

In summary, van der Waals forces exist even between electrically neutral objects that do not carry electric or magnetic moments [21]. In nature, van der Waals forces allow geckos to climb on flat but polarizable surfaces [5].

## 1.2   Models of contact between a particle and a substrate

The first attempt to model the particle deformation (Fig. 1.2) under an external applied load $P$ was done by Heinrich Hertz [66] in 1882. He solved the contact problem of two elastic bodies with curved surfaces under the applied load. However, his model considered only non-adhesive contact, i.e., all interactions (and particularly van der Waals) except for the external load were neglected. This model will be discussed in section 1.2.1. Later in the 1970s, two other models were developed by Johnson, Kendall & Roberts [78] (JKR model) and Derjaguin, Muller & Toporov [49] (DMT model). Both of these models incorporate the adhesion in Hertzian contact. JKR (see section 1.2.2) and DMT (see section 1.2.3) are complementary models that are chosen depending on Tabor's parameter or Maugis parameter, which establishes the range of applicability of the two models.
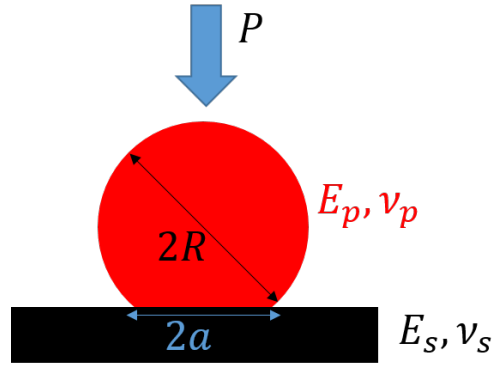
Figure 1.2: Scheme of a contact between a particle having a radius of $R$ and a plane. The Young's moduli and Poison's ratios of contacting materials are $E_p$, $E_s$ and $\nu_p$ and $\nu_s$, respectively. The radius of contact zone (contact radius) is denoted by $a$. The applied load is $P$.

### 1.2.1 Hertz model

Hertz considered only the non-adhesive elastic contact. The materials of contacting solids are supposed linearly elastic, and all components of the strains are small, and the higher-order terms are disregarded. For the contact between a sphere of a radius $R$ and a half-space, the relation between the radius of the contact area $a$ caused by the applied load $P$ reads

$$a^3 = \frac{PR}{K}, \tag{1.1}$$

where $K$ is the effective Young modulus with the factor 4/3:

$$K = \frac{4}{3} \left( \frac{1-\nu_p^2}{E_p} + \frac{1-\nu_s^2}{E_s} \right)^{-1}, \tag{1.2}$$

and $E_p$, $\nu_p$ and $E_s$, $\nu_s$ are Young's moduli and Poisson's ratios associated with the particle and the substrate, respectively. The deformation (indentation), $\delta$, is related to the contact radius, $a$, as follows:

$$\delta = \frac{a^2}{R}. \tag{1.3}$$

The combination of Eqs.(1.1)&(1.3) gives loading curve $P$-$\delta$:

$$P = KR^{\frac{1}{2}}\delta^{\frac{3}{2}}. \tag{1.4}$$

The Hertz loading is presented in Fig. 1.3. According to Fig. 1.3, a particle will have a deformation, $\delta_0$ (and the radius of a contact area, $a_0$), under the applied load of $P_0$, and a deformation $\delta_1 > \delta_0$ ($a_1 > a_0$) under the applied load $P_1 > P_0$.

### 1.2.2 JKR model

To incorporate the effect of adhesion in the Hertz model, Johnson, Kendall & Roberts [78] considered the total energy of the contact system $U_T$, as made up of three terms: the stored elastic energy $U_E$, the mechanical energy in the applied load $U_M$, and the loss in surface energy
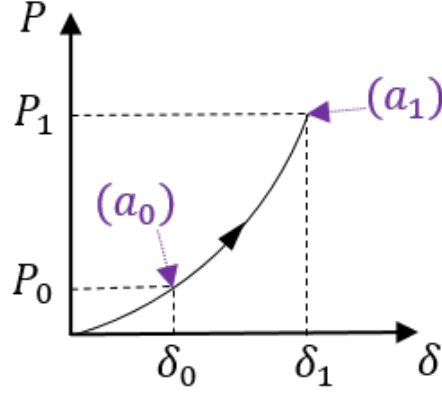
Figure 1.3: Loading diagram according to Hertz model (Eq.(1.4)).

$U_S$ (where van der Waals forces are implicitly taken into account). The total energy, therefore, reads

$$U_T = U_E + U_S + U_M. \tag{1.5}$$

In the JKR model, the contact radius $a_1$ under the applied load $P_0$ is greater than that predicted by Hertz $a_0$ due to the presence of surface forces of attraction that deform contact surfaces even in the absence of the applied load.

We will detail the derivation of the JKR model because, even in the most comprehensive derivation we have found [15], some points remain unclear for those who are not elasticity experts. The JKR model assumes that the contact system has come to its real state in two steps (Fig. 1.4). First, the system is loaded according to the Hertz load-displacement relation Eq.(1.4). The authors suppose that a real contact radius $a_1$ is caused by some apparent Hertz load $P_1$ (with an apparent depth of indentation $\delta_1$). Second, the system is unloaded following Boussinesq load-displacement relation Eq.(1.6) up to the real applied load $P_0$. According to the JKR model, the particle is in the $(\delta_2, P_1)$ state on the diagram presented in Fig. 1.4. Eq.(1.6) supposes the change in the indentation depth $\delta$ under the unchanged contact radius $a_1$ through the unloading.

$$P = \frac{3}{2}K\delta a_1 \tag{1.6}$$

The elastic energy $U_E$ (i.e., energy stored as the particle is subjected to elastic deformation) is calculated in two steps according to the loading diagram (Fig. 1.4). First, we apply a load $P_1$ following the Hertz load (Eq.(1.4)). The corresponding indentation depth is $\delta_1$. Therefore, the stored energy $U_l$ (red dashed area in Fig. 1.4) is calculated as

$$U_l = \int_0^{\delta_1} P_{loading} d\delta = \left( P_1 \delta_1 - \int_0^{P_1} \delta dP \right). \tag{1.7}$$

Second, the system is unloaded, releasing energy $U_u$ (blue dashed area in Fig. 1.4). This energy can also be calculated as an integral. The difficulty is that the unloading branch presented in Fig. 1.4 is the Boussinesq equation shifted along $\delta$-axis in such a way that it passes through the $(\delta_1, P_1)$. To simplify the calculation of the integral, we translate the unloading branch along $\delta$-axis (Fig. 1.5), so that we have an original Boussinesq equation (Eq.(1.6)). The area (blue dashed zone in Fig. 1.5) under the linear curve remains unchanged. This area is equal to the area of the
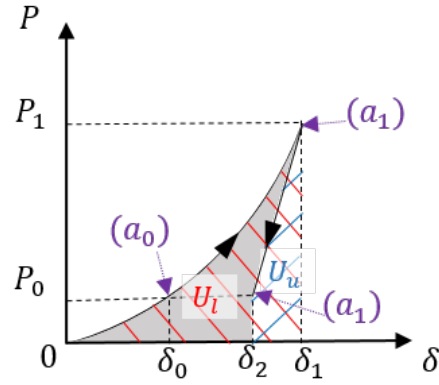
Figure 1.4: Loading diagram according to the JKR model [78, 15]. The loading branch follows the Hertz load-displacement relation Eq.(1.4), and the unloading branch satisfies the Boussinesq solution for contact between an elastic half-space and a flat punch Eq.(1.6). The gray zone corresponds to the elastic energy $U_E$.

trapezoid limited by the Boussinesq curve, $P = P_0$, $P = P_1$, $\delta = 0$ (green dashed area in Fig. 1.5). Thus, the expression for $U_u$ simply reads
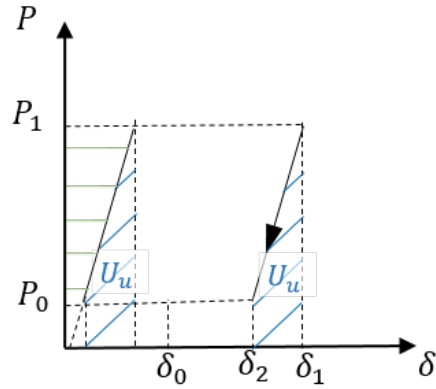


Figure 1.5: Translation of the unloading branch.

$$U_u = \int_{\delta_1}^{\delta_2} P_{unloading} d\delta = \int_{P_0}^{P_1} \delta dP, \tag{1.8}$$

where the deformation is given by the original Boussinesq equation (Eq.(1.6)). Therefore, one can work out the total stored elastic energy $U_E$, which is the difference between the elastic energy

stored after loading, $U_l$, and the elastic energy released during unloading, $U_u$:

$$U_E = U_l - U_u = \underbrace{\left( P_1 \delta_1 - \int_0^{P_1} \delta\left(P\right) dP \right)}_{\substack{\delta(P) \text{ according to} \\ \text{the Hertz load}}} - \underbrace{\int_{P_0}^{P_1} \delta\left(P\right) dP}_{\substack{\delta(P) \text{ according to the} \\ \text{Boussinesq equation}}} . \tag{1.9}$$

Using the diagram Fig. 1.4, the mechanical energy $U_M$ reads

$$U_M = -P_0 \delta_2, \tag{1.10}$$

and the loss in surface energy, $U_S$:

$$U_S = -\pi w a_1^2, \tag{1.11}$$

where $w$ is the adhesion energy (sometimes also referred to as "surface energy") of both surfaces.

The JKR model assumes that the equilibrium at contact satisfies the equation $\frac{dU_T}{da_1} = 0$, which leads to the following relation between an apparent Hertz load $P_1$ and a real applied load $P_0$:

$$P_1 = P_0 + 3w\pi R + \sqrt{6w\pi R P_0 + (3w\pi R)^2}. \tag{1.12}$$

Substituting the apparent Hertz load $P_1$ (Eq.(1.12)) in the Hertz model (Eq.(1.1)), we obtain the relation between the real applied load $P_0$ and the contact radius $a_1$:

$$P_0 = \frac{K}{R} a_1^3 - \sqrt{6\pi w K a_1^3}. \tag{1.13}$$

In the absence of external load $P = 0$, the deformation still occurs due to long-range attractive interactions, and the contact radius $a_0$ is non-zero:

$$a(P = 0) = \sqrt[3]{\frac{6\pi w R^2}{K}}. \tag{1.14}$$

According to Eq.(1.13), when the applied load is negative, i.e., the force is pulling the particle upward, the contact radius decreases. The separation between the particle and its substrate would occur at the lowest achievable contact radius:

$$a_d = \sqrt[3]{\frac{3\pi w R^2}{2K}} \approx 0.63 a(P = 0) \tag{1.15}$$

Substituting $a_d$ in Eq.(1.13), one can obtain the applied load required to detach a particle from the substrate $P_d$:

$$P_d = -\frac{3}{2} \pi w R. \tag{1.16}$$

The adhesion force is, thus, equal to $1.5\pi w R$.

**Extension to plastic deformations**

Maugis and Pollock [104] (MP) generalized the JKR model to include plastic deformations. According to the MP model, the contact radius $a$ between a particle of radius $R$ and a substrate is related to the hardness of the material $H_0$, adhesion energy $w$, and an external applied load $P$ as

$$P + 2\pi w R = \pi a^2 H_0. \tag{1.17}$$

**Adhesion energy**

One can obtain the adhesion energy $w$ theoretically or experimentally.

To obtain the adhesion energy theoretically, one can use the relation between the adhesion energy and the surface energies of a particle and a substrate, $\gamma_p$ and $\gamma_s$, respectively [45]

$$w = \gamma_p + \gamma_s - 2\beta_e\sqrt{\gamma_p\gamma_s}, \tag{1.18}$$

where $\beta_e$ is a factor that has been empirically determined to have values ranging from 0.5 to 1.2 but is often supposed to be equal to 1 [57].

Experimentally, the adhesion energy, $w$, is obtained using the JKR or MP model with no external load. These models predict that $a$ vary as $R^{2/3}$ (JKR) or $R^{1/2}$ (MP). For different particles radii $R$, the contact radius $a$ is measured (Fig. 1.6). Then, using Eq.(1.14) or Eq.(1.17), the adhesion energy, $w$, can be determined.
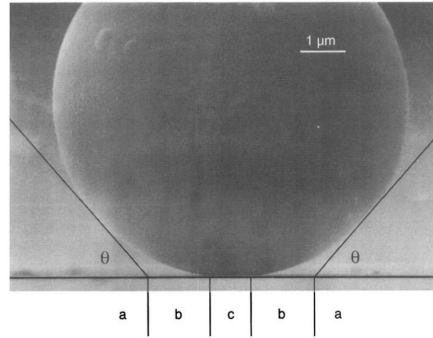


Figure 1.6: An example of high tilt SEM micrograph of a polystyrene sphere on a silicon substrate. Area "c" is the particle-substrate contact. Image taken from [17].

Table 1.1 summarizes the values of the adhesion energy found in literature.

| Reference | adhesion energy $w$, J/m$^2$ | material of particle/substrate | method of obtaining (model used) |
|---|---|---|---|
| Dejesus *et al.*[45] | 0.04 | polyester/ceramer | theoretically |
| Rimai & Busnaina [134] | 0.17 | soda-lime glass/polyurethane | experimentally (JKR) |
| DeMejo *et al.*[46] | 0.17 | glass/polyurethane | experimentally (JKR) |
| Rimai *et al.*[135] | 0.068 | polystyrene/polyurethane | experimentally (MP) |
| Rimai *et al.*[137] | 0.32 | polystyrene/silicon | experimentally (MP) |

Table 1.1: Values of adhesion energy found in literature.

However, the obtained values are not very accurate, especially those obtained with the MP model, as the exact value of hardness is usually unknown. The difference between the estimated and actual hardnesses can result in significant differences in the calculated adhesion energy [137]. For example, in 1990, Rimai *et al.*[136] obtained $w = 0.72$ J/m$^2$ for polystyrene particles on silicon

substrate, but later in 1993 the same authors updated this value to $w = 0.32\,\mathrm{J/m^2}$ [137] because of revised values of silicon hardness.

**Non-spherical particles**

Dejesus *et al.* [31] studied the adhesion of non-spherical particles. The authors followed Fuller & Tabor approach [59] to consider the contact area as the sum of $n_{asp}$ asperities having a Gaussian distribution about a mean radius $r_{asp}$. Thus, the applied load required to detach a particle $P_d$ reads:

$$P_d = \frac{3}{2}\pi w n_{asp} r_{asp}. \tag{1.19}$$

### 1.2.3 DMT model

Derjaguin, Muller & Toporov [49] proposed another model for adhesive contact. They introduced **non-contact** forces acting across the gap between a particle and a substrate. These forces do not induce additional deformations to the particle but make its detachment more difficult. The adhesion force due to surface-surface interactions is added, and the contact radius is increased with respect to that predicted by the Hertz model because of these interactions. The applied load is thus balanced by elastic response and adhesion force:

$$P = \frac{K}{R}a^3 - 2\pi R\Phi, \tag{1.20}$$

where $\Phi$ is the molecular force potential expressed as

$$\Phi = \frac{H}{12z_0^2\pi}, \tag{1.21}$$

where $H$ is the Hamaker constant, and $z_0$ is the separation distance (i.e., the least possible spacing between the surfaces of the particle and the substrate), which is typically between $3 \times 10^{-10}\,\mathrm{m}$ and $4 \times 10^{-10}\,\mathrm{m}$ [113]. The separation of a particle from the substrate occurs when the contact radius $a$ is equal to 0, and the force required to detach a particle is:

$$P_d = -2\pi R\Phi. \tag{1.22}$$

**Hamaker constant**

Here, for the case of a particle on a substrate, the Hamaker constant $H_{132}$ is represented by a coefficient accounting for the van der Waals interaction between two materials 1 and 2 embedded in a medium 3. It is related to the Hamaker constants of the individual materials (i.e., interaction between two bodies of the same material in a vacuum). It has the following approximate expression [171]:

$$H_{132} \approx \left(\sqrt{H_{11}} - \sqrt{H_{33}}\right)\left(\sqrt{H_{22}} - \sqrt{H_{33}}\right), \tag{1.23}$$

where $H_{ii}$ is the interaction Hamaker constant of two bodies of same material $i$ in a vacuum. Usually, the Hamaker constants are measured experimentally. A large amount of data on measured Hamaker constants for different materials is collected in a review by Visser [171]. However, the variation in the obtained constants is very important. For instance, the induvidual Hamaker constant for polystyrene (i.e., polystyrene-polystyrene interaction in vacuum) ranges from $5.6 \times 10^{-20}\,\mathrm{J}$ to $54.9 \times 10^{-20}\,\mathrm{J}$ [171].

### 1.2.4 What model to choose?

**Tabor's parameter**

Both the adhesion energy $w$, introduced by JKR, and the molecular force potential $\Phi$, introduced by DMT, have the same idea of interaction energy between two solids. This energy can be referred to as $\Delta\gamma$ ($\Delta\gamma = w$ for the JKR model and $\Delta\gamma = \Phi$ for the DMT model). In this case, the adhesion force $F_{ad}$ ($F_{ad} = -P_d$ in both models) is proportional to $\pi R \Delta\gamma$ with the coefficient 1.5 (JKR) or 2 (DMT). The choice of this coefficient (and, consequently, the model) is decided by the so-called "Tabor's parameter" $\mu_T$ [158]:

$$\mu_T = \left( \frac{16 R \Delta\gamma^2}{9 K^2 z_0^3} \right)^{1/3},\qquad(1.24)$$

which is the ratio between the normal elastic deformation caused by adhesion $\left( \frac{16 R \Delta\gamma^2}{9 K^2} \right)^{1/3}$ and the spatial range of the adhesion forces $z_0$. If $\mu_T \geq 1$, the non-contact forces of attraction can be ignored, and the JKR model should be applied. On the other hand, if $\mu_T < 1$, the DMT model is more appropriate.

It was then shown [159, 48] that the JKR model ($\mu_T \geq 1$) should be valid for soft materials (i.e. those whose Young's modulus is less than approximately $10\,\mathrm{MPa}$) while the DMT model ($\mu_T < 1$) should hold for hard materials (i.e., those whose modulus is greater than approximately $1\,\mathrm{GPa}$).

**Maugis parameter**

The improvement to the Tabor approach was proposed by Maugis [105]. The author introduced another parameter $\lambda_M$ referred to as a "Maugis" or "transitional" parameter related to Tabor's one as follows:

$$\lambda_M = 1.1570 \mu_T.\qquad(1.25)$$

The JKR model appplies if $\lambda_M > 5$, and the DMT model is valid, if $\lambda_M < 0.1$. If $0.1 < \lambda_M < 5$, we are in the transition region between the JKR and DMT models.

### 1.2.5 Challenges

Although adhesion has been studied for more than 50 years, many uncertainties still remain. Some of them will be discussed in this section.

First of all, any "flat" surface has morphological irregularities (i.e., surface roughness). Multiple asperities of different heights are randomly distributed on the surface, making the surface look like a mountain-valley. When two surfaces are in contact, the "mountains" from different surfaces touch one another, while the "valleys" do not [129]. As a result, the real contact area is smaller than what we can estimate from SEM images (Fig. 1.6). Moreover, a variation in the adhesion force may arise from the number of asperities involved in the contact. The higher the number of asperities involved in the contact, the more accurate the estimation of the adhesion force [129].

If a particle is partially immersed in liquid or condensation of the surrounding vapor took place between the particle and its substrate, the adhesion will be different [131]. First, the liquid bridge can additionally attach the particle [116, 131], and the medium itself affects the net interactions between two materials in contact [131]. The DMT model takes this effect into account through the Hamaker constant, but the JKR theory ignores it. However, the Hamaker constant is not

properly measured, leading to wide data scattering [171]. The uncertainty of the adhesion energy used in the JKR theory is also observed [137].

Moreover, there are some problems with experimental validation for both models. Indeed, the validation of the JKR model was done by examining whether the contact radius $a$ varies as $R^{2/3}$ (e.g., [134]). To the best of our knowledge, there are no comprehensive studies that include both comparison of the contact radius and the detachment force of particles on the same sample. Similarly, no experimental comparisons have been found in the literature for the DMT model. This is probably due to the application range of the DMT model, which is valid on very rigid bodies, and hence the contact radius is too small, making its measurement on SEM hardly possible.

Finally, none of the presented models take into account the dependency of adhesion on time. Dejesus *et al.*[44] found that the adhesion force often increases with time over periods ranging from days to months. This increase has generally been associated with the occurrence of either plastic or viscoelastic deformation of at least one of the materials in contact. In addition, deviations from perfect sphericity have also been shown to decrease the detachment force from that predicted by the JKR theory.

## 1.3    Adhesion force measurement

The force of interaction between a particle (or cell) and a substrate is essential for several industries, especially in the control of surface hygiene. Today, many different methods have been developed to evaluate the interaction force between a particle and a substrate. These methods can be classified into three main categories: (i) centrifugation, (ii) hydrodynamic shear, and (iii) single-particle manipulation [29].

### 1.3.1    Centrifugal method

The centrifugal methods are used for the interaction force measurements since 1950s [89]. These methods rely on the analysis of whole populations and, therefore, the measurement of averaged responses. In centrifugation tests, the substrate with cells is placed in a centrifuge perpendicularly to the rotation axis. The centrifugal force, perpendicular to the surface, separates adherent particles [125]. The scheme of a centriguge assay is presented in Fig. 1.7.
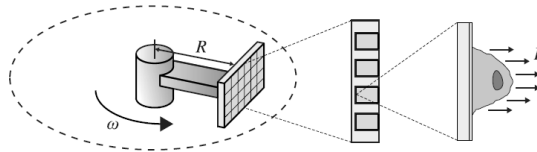


Figure 1.7: Schematic of a typical centrifuge assay. A multiwell plate is sealed and spun with the wells facing outwards. A body force, acting normal to the well bottom, is applied on the cells to cause detachment. Image taken from [29].

These techniques are limited to the analysis of weakly adherent cells due to the low magnitude of gravitational forces ($< 1\,\mathrm{nN}$) realistically generated using a benchtop centrifuge [29]. Usually, this technique is suitable for particles smaller than a few microns [164]. Besides, the centrifugal method allows one to estimate only the interaction force of particle or cell populations (i.e., a percentage of cells resistant to detachment under a given force), but not the force required to detach an individual particle or cell.

### 1.3.2  Shear stress method

Shear stress methods are usually based on fluid flows or air jets. In all these methods, particle detachment is induced by shear stresses parallel to the contaminated surface, resulting from fluid flow, which is usually maintained in a laminar regime. It is worth to note that shear stress methods only give the shear stress required to detach particles, but they are not suitable for the detachment force measurements.

Numerous devices have been designed to implement hydrodynamic methods and involve the application of well-controlled fluidic shear stresses to adhered particles. These include spinning disks [68, 60], flow chambers (radial [61, 9] or rectangular [167]) or even the fluid dynamic gauging technique, initially developed for measuring the thickness of soft solid deposit layers immersed in a liquid environment [62]. Most of these hydrodynamic methods are rather adapted to the analysis of populations, but some flow cells allow the observation of particle detachment kinetics under the microscope, which, in turn, allows to analyze the behaviour of individual cells. It is thus possible to identify variability within populations or to analyze the kinetics of interaction forces in response to various factors.

Air jets have also been extensively used to detach adherent particles [58], because of their relevance in cleaning in areas such as semiconductor industry, contamination control, and homeland security.

The cleaning-in-place, which is the automated cleaning of the interior surfaces of equipment in the food and pharmaceutical industries [34], relies on shear stress methods, and the adjustment of flow parameters (temperature of the cleaning solution, concentration of the cleaning agent, time of cleaning, flow rate) increases its application range [63].

### 1.3.3  Single-particle manupulation

Single-particle micromanipulation methods, as their name implies, are exclusively dedicated to the analysis of the behavior of individual particles. The direct force probing technique is essentially relying on the use of micropipettes [156, 165], optical tweezers [23] and atomic force microscope (AFM) [142] or derived methods. The single-particle micromanipulation methods allow to measure horizontal, vertical, or both detachment forces.

AFM has often been used to quantify the interaction force up to $\sim 100\,\mathrm{nN}$ [142] between particle-coated cantilevers and substrates of interest. They require the preliminary immobilization of a single particle on a cantilever tip (e.g., through glutaraldehyde, poly-L-lysine, or polydopamine [poly-DOPA]) that will be put in contact with the substrate. The cantilever bending, which correlates the interaction between a particle and its substrate is recorded via a laser that is reflected from the cantilever onto a photodiode. The deflection of the bacteria-coated cantilevers can then be converted into interaction force thanks to the spring constant of the cantilever.

The imperfection of this technique is that the improper attachment of particles to the cantilever tip [117] may give rise to inconsistent readings. Moreover, the different steps of this method could induce changes in particle surface properties and/or in the physiological state (if biological particles are tested). For instance, during the particle immobilization step, where the particle can be damaged, or the adhesion step, where particles are overheated by laser reflection during repetitive reading.

Another method derived from the AFM technique is the fluidic force microscopy (FluidFM) [127, 108]. The approach is very similar to that used classically by AFM, except for the immobilization of the particle on the tip of the cantilever, which is achieved by a negative pressure. The micro-channeled AFM cantilevers are connected to a pump through a microfluidic system. The cantilever is brought into contact with a substrate, and the contact is maintained for a given time. The cantilever is then retracted and its deflection recorded to determine the interaction

force between the particle and the substrate. The FluidFM method is schematically presented in Fig. 1.8. By selecting the optimal opening size and spring constant of the cantilever, this method permits measurements of adhesion forces down to $10\,\mathrm{pN}$ and up to $50\,\mathrm{nN}$ [108].
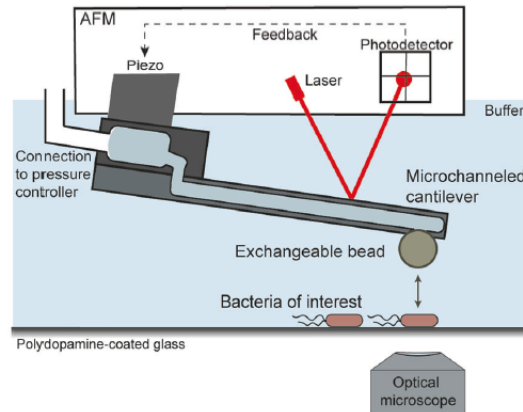


Figure 1.8: Schematic representation of bacteria removal using FluidFM technique. Image taken from [108].

Lastly, some authors reported results on the **lateral** detachment of adherent bacteria using AFM [157]. This method is used to follow the detachment of bacteria adherent to various materials. The tip is placed against an adherent particle, and the interaction force is scanned using increasing tip force until its detachment.

Optical tweezers can also be used to measure the adhesive forces between beads and surfaces. The technique can measure weak forces ranging from sub-picoNewton up to several hundreds of $\mathrm{pN}$ with good accuracy [23].

Micropipette aspiration has been used to measure the adhesion strength [156, 165]. A small micropipette is brought into contact with a particle, and an aspiration pressure is applied. The pipette is then moved away from the cell. If the cell did not detach, then the aspiration pressure is increased, and the process is repeated.

The inconvenience of single-particle manipulation methods is that they can be time-consuming and often require specialized equipment and a high level of expertise. Also, if the aspiration process needs to be repeated many times before detachment, as in [155, 133], the response of the particles due to the multiple loadings may alter the results.

## 1.4 Capillary effects

### 1.4.1 Introduction to surface tension

At equilibrium, the droplet lying on the surface forms the contact radius $R_c$ and the equilibrium contact angle $\theta$ with that surface (Fig. 1.9). The liquid–vapor, the liquid–solid and the solid–vapor interfaces having surface tensions $\gamma$, $\gamma_{sl}$ and $\gamma_{sv}$, respectively, meet at a triple contact line. The microscopic origin of surface tension lies in the intermolecular interactions and thermal effects [10] while macroscopically it can be understood as a force acting along the interface or an energy per unit surface area [101].
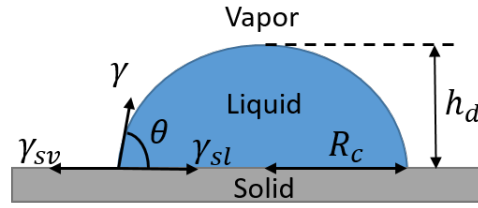
Figure 1.9: Droplet on substrate having a contact radius of $R_c$ and forming a contact angle of $\theta$ with substrate. The liquid–vapor, liquid–solid, and solid–vapor interfaces have the surface tensions of $\gamma, \gamma_{sl}$ and $\gamma_{sv}$.

In 1805, Young [183] proposed a relation between the contact angle and three surface tensions, but no proof of this relation was given. Later, in 1869, Dupré and Dupré [52] expressed this relation mathematically (Eq.(1.26)) and proved it by projecting the surface tensions in equilibrium on horizontal axis. That is why sometimes the relation is called "Young–Dupré equation" instead of the wildly used "Young's equation".

$$\cos\theta = \frac{\gamma_{sv} - \gamma_{sl}}{\gamma} \tag{1.26}$$

For a long time, however, physicists were not sure that surface tension could be considered as forces acting on the wetting perimeter, and hence the proof by [52] was in question. Today, several approaches were proposed to prove this relation. Two of them, energy minimization and variational approaches, are presented in [151].

The contact angle $\theta$ formed by a droplet with a surface can be derived from Eq.(1.26). If $0 < \theta < 90°$, the surface is regarded as wettable (Fig. 1.10, a). If the liquid in use is water and $0 < \theta < 90°$, the surface can also be referred to as hydrophilic. If $90° < \theta < 180°$, the surface is non-wettable (Fig. 1.10, b). If the liquid in use is water and $90° < \theta < 180°$, the surface can also be referred to as hydrophobic. If $\theta = 0°$ or $\gamma_{sv} \geq \gamma_{sl} + \gamma$, i.e., Eq.(1.26) would suggest $\cos\theta \geq 1$, the total (or complete) wetting (Fig. 1.10, c) is observed. If $\theta = 180°$ or $\gamma_{sl} \geq \gamma_{sv} + \gamma$, i.e., Eq.(1.26) would suggest $\cos\theta \leq -1$, the completely non-wetting case (Fig. 1.10, d) is realized.
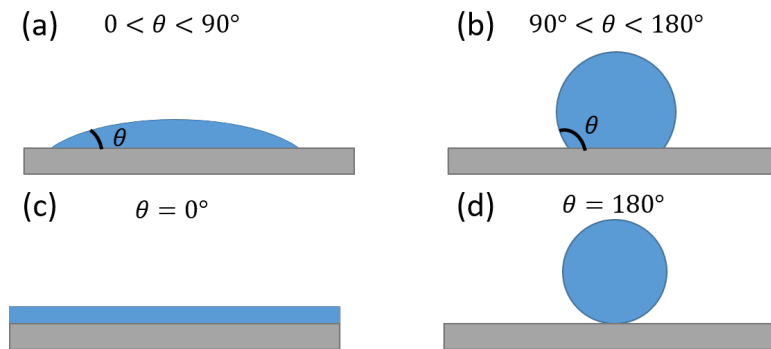


Figure 1.10: Partial wetting: wettable (a) and non-wettable (b); total wetting (c); no wetting (d).

However, Young's equation is valid only for ideal surfaces, which are atomically flat and chemically homogenous [54]. In reality, solid surfaces are seldom truly homogeneous, and defects

may be either geometrical [173, 22, 79] or chemical [147, 76, 177]. If the solid is not ideal, then the hysteresis of the contact angle occurs. This phenomenon was referred for the first time by Lord Rayleigh, while he was examining a liquid drop to advance over or recede from a solid surface in 1890 [140].
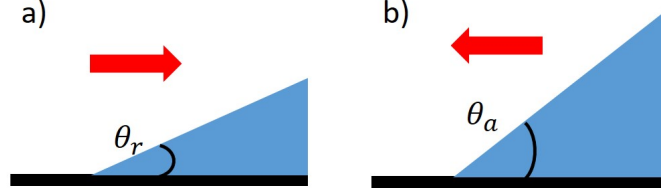


Figure 1.11: Schematic representation of an advancing (a) and a receding (b) liquid front and the corresponding angles. The red arrows represent the direction of the liquid front motion.

On non-ideal surfaces, the contact angle $\theta$ lies between the advancing (maximal) contact angle $\theta_a$ (Fig. 1.11, a) and the receding (minimal) contact angle $\theta_r$ (Fig. 1.11, b). The advancing and receding contact angles are measured when liquid advances or recedes, respectively [152]. The contact angle hysteresis $\theta_h$ is the difference between the advancing and receding contact angles:

$$\theta_h = \theta_a - \theta_r. \tag{1.27}$$

When the droplet is at rest on the substrate, there is a competition between the capillary forces, which tend to give the droplet a spherical shape, and the gravitational force, that tends to flatten the droplet against the substrate. The importance of gravitational forces compared to surface tension forces for the liquid front movement is expressed by the so-called Bond number:

$$\mathrm{Bo} = \frac{\rho_l g L^2}{\gamma}, \tag{1.28}$$

where $\rho_l$ is the density of the liquid, $g$ is the gravity acceleration, $L$ is the characteristic length (e.g., the contact radius $R_c$ of a droplet or the droplet height $h_d$ - see Fig. 1.9), and $\gamma$ is the liquid-air surface tension.

### 1.4.2 Liquid bridge under a particle

It was previously mentioned that the effect of liquid bridges (Fig. 1.12) on particle adhesion can be significant [131]. Hereafter, we will detail the forces that can arise from a liquid bridge (i.e., the liquid membrane between two rigid bodies) located between a particle and its substrate.

Similar to the case of a droplet placed onto a substrate (Fig. 1.10), the balance of surface tensions at liquid-air-particle and at liquid-air-substrate interfaces defines the contact angles $\theta_p$ and $\theta_s$, respectively. So that, the liquid bridge must merge the particle and the substrate at a certain angles, and therefore, the surface tension dictates a shape of the liquid bridge. The curvature of the meniscus, $H_f$, is related to the difference between air pressure, $p_A$, and liquid pressure, $p_L$, by the Young-Laplace equation:

$$p_A - p_L = \gamma H_f, \tag{1.29}$$

where $\gamma$ is the air-liquid surface tension.
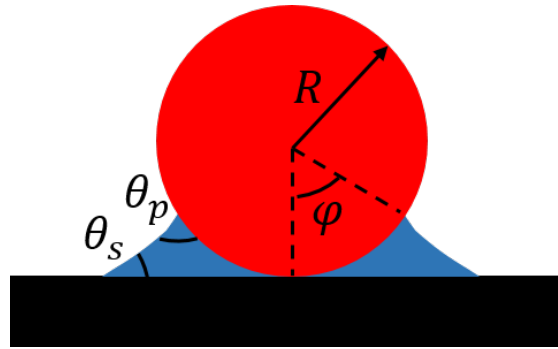
Figure 1.12: Liquid bridge formed between a particle (contact angle $\theta_p$) having a radius $R$ and a substrate (contact angle $\theta_s$). The filling angle is $\varphi$.

The total force exerted through the liquid bridge on the particle results from capillary and Laplace forces [116]. The vertical component of capillary force is

$$F_c = 2\pi R \gamma \sin\varphi \sin(\theta_p + \varphi),$$ (1.30)

and the $z$-projection of the Laplace force reads

$$F_L = 2\pi (p_L - p_A) R^2 \sin^2\varphi.$$ (1.31)

## 1.5 Conclusions

Throughout this chapter, we first discussed the existing models for adhesion force as well as their deficiencies. Although much research has been done, there are no complete answers to many questions, e.g., time-dependent adhesion, effect of medium, lack of experimental validation.

Then, we revised the techniques that are currently used for the adhesion force measurements, as well as their strengths and weaknesses. The most robust single-particle manipulation techniques are AFM-based, which are expensive and require strong skills. In Chapter 2, we will present a new patch-clamp based technique for detachment force measurements. This technique can be a good fit for biology researchers, as no additional expensive devices are required.

Finally, we discussed the additional force acting on a particle if a liquid bridge is formed underneath. We wonder if the inverse situation may occur if a particle is immersed in liquid (Fig. 1.13). And if it is the case, would this bubble affect the force required to detach a particle measured in Chapter 2. The numerical and experimental study of an air bubble trapped under a particle is presented in Chapter 3.
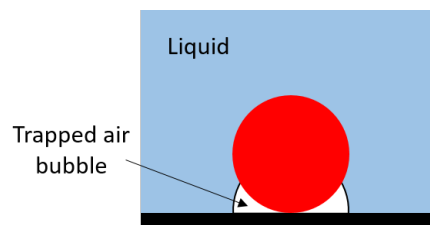


Figure 1.13: Schematic representation of an air bubble trapped under a particle.

# Chapter 2

# Experimental study of detachment forces

In this chapter, we present the patch-clamp technique used to measure the detachment force of particles from their substrates. We demonstrate the implementation of the patch-clamp technique, including the calibration of the pipette resistance - tip area curve. Using the aforementioned technique, we investigate the effect of particle size and drying conditions such as temperature and duration on the detachment force. The results are then compared to theoretical models in the literature and the agreements and differences are discussed.

The use of glass micropipettes for the detachment force measurements has already been reported in the literature [156, 165, 155]. In these experiments, the pipettes were mounted on a hydraulic micromanipulator and connected to the pressure pump with an aspiration pressure $\sim 0.1\,\mathrm{mbar}$. However, to the best of our knowledge, no work has been reported on the modification of the patch-clamp technique for the detachment force measurements, as will be presented in this chapter. The proposed technique uses a patch-clamp setup with the mounted micropipettes, connected to a fluid pump with an aspiration pressure of up to $800\,\mathrm{mbar}$.

## 2.1   Materials

Experiments were performed with monodisperse Red Fluorescent Polystyrene particles (Thermo Scientific) of different diameters: $1\,\mathrm{\mu m}$ (Coefficient of Variation [CV] = 5%), $3\,\mathrm{\mu m}$ $\mathrm{\mu m}$ (CV = 5%), $6\,\mathrm{\mu m}$ (CV = 18%), $12\,\mathrm{\mu m}$ (CV = 18%). The particles have all a density of around $1.05\,\mathrm{g/cm^3}$ and show strong hydrophobic characteristics [56]. The stiffness of the particles were measured by an AFM (Bruker Dimension Icon) in PeakForce mode and the value was found to be $\sim 3\,\mathrm{GPa}$. The microspheres were directly shipped by the supplier either in aqueous solutions ($1\,\mathrm{\mu m}$ and $3\,\mathrm{\mu m}$) or as dry powder ($6\,\mathrm{\mu m}$ and $12\,\mathrm{\mu m}$). A suspension of concentration 0.12% weight per volume was made. Thereafter, a $2\,\mathrm{\mu L}$ droplet of the prepared suspension was gently positioned with a micropipette on a glass coverslip previously cleaned with ethanol. The droplet on the coverslip was then placed in an oven to force its evaporation for 1, 24, 48 or 72 h at a controlled temperature ($40\,^\circ\mathrm{C}$ or $50\,^\circ\mathrm{C}$) in a dry atmosphere (relative humidity below 30%). The coverslip was then immersed in a Hank's Buffered Salt Solution (HBSS[1]) contained in a recording chamber placed on an inverted TMD Diaphot Nikon microscope. The use of HBSS solution is necessary to

---

[1]HBSS solution composed of (in mmol): 142 NaCl, 5.6 KCl, 1 CaCl$_2$, 1 MgCl$_2$, 10 HEPES, 2 NaHCO$_3$, 0.44 KH$_2$PO$_4$, 0.34 Na$_2$HPO$_4$ with an osmolarity of 300 mOsm/l and a pH of 7.4.

measure the pipette resistance, that will be further used to calculate the detachment force (see below).

The interaction force between a microsphere and a substrate was enabled by an adaptation of the commonly used patch-clamp technique [143, 64] that was developed to study ionic currents in individual cells. As mentioned before, our technique consists of approaching a micropipette to the microparticle, applying a negative pressure, then pulling away the micropipette and observe the eventual detachment of the particle. Fig. 2.1 and 2.2 show a sketch of the experimental setup and the associated procedure, respectively. The negative pressure was provided by means of a
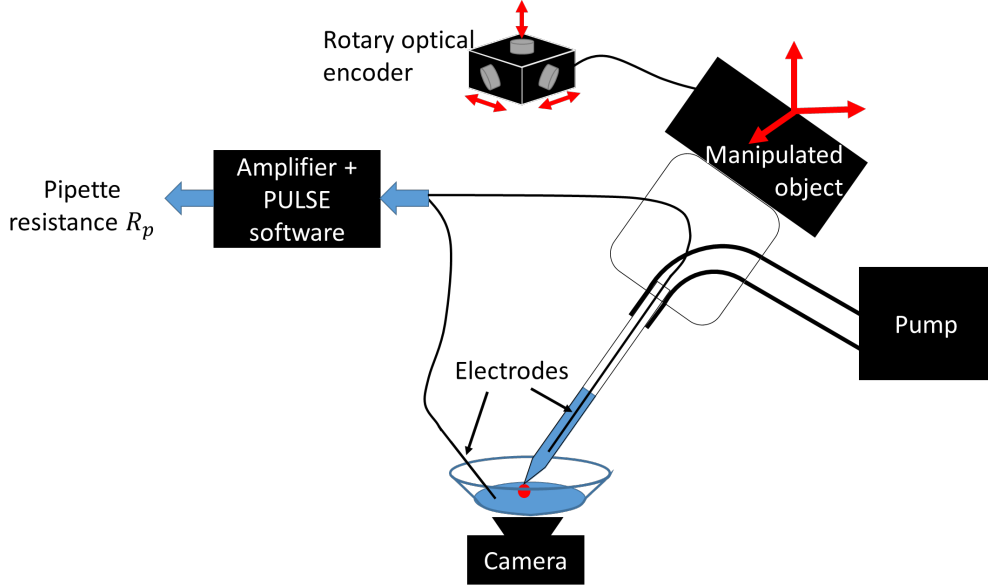


Figure 2.1: Scheme of the setup. The pipette is approached to a microparticle using patch-clamp equipment. The depression inside the pipette is created using the pump (which is not used for simple patch-clamp). Similar to simple patch-clamp, the pipette resistance is measured using patch-clamp amplifier. The process is recorded from the bottom with a camera.

microfluidic pump Fluigent LineUp Flow EZ (Fluigent SA, Le Kremlin Bicêtre, France) connected to the pipette. The motion of the latter was controlled by a motorized micromanipulator (MP 285, Sutter Instruments Company, Novato, CA, USA).

In the present method, the size of the tip of the micropipette had to be adapted according to the tested particle diameter. In this regard, we used a pipette puller (P97 pipette puller, SUTTER Instruments Co) to manufacture the desired tip size from borosilicate capillary tubes (1B150F-3, WPI, Sarasota, Fl, USA). It is from the tip area, $A_{tip}$ ($\mu m^2$), of the pipette that we deduce the force ($F_d$ in nN) applied to the particle,

$$F_d = 10^{-1} \cdot A_{\text{tip}} \cdot p \cdot \sin(\alpha) \tag{2.1}$$

where $p$ is the pressure in (mbar), $\alpha$ is the inclination of the pipette (see Fig. 2.2, $\alpha = 45°$ in our case). The factor $10^{-1}$ appears to compensate the use of "prefixed" SI units ($\mu m$) and non-SI units (mbar). It is to note that the adhesion force between the particle and the pipette tip is neglected, as the contact area (and, consequently, the van der Waals interactions) of glass-particle is too small next to the contact area particle-substrate.
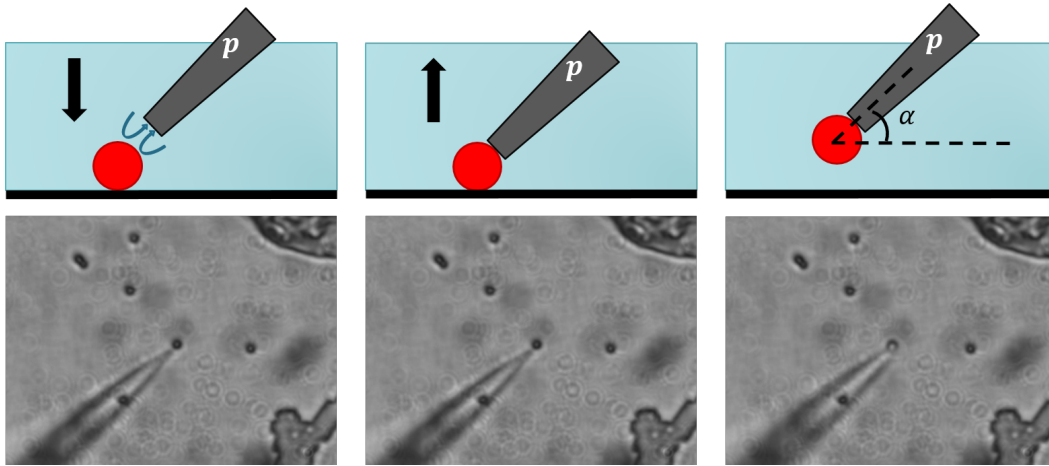
Figure 2.2: Working principle (top) and real images (bottom) from the camera of $1\,\mu m$ particle removal. The pipette with a certain depression is approached to a microparticle (left). The pipette touches the particle (center). The pipette is pulled away with the particle.

From the above equation, the importance of an accurate knowledge of $A_{\text{tip}}$ to estimate $F_d$ can be noticed. To ascertain the precise size of the tip at each run, the electric resistance across the tip was measured by means of an electrode placed in the pipette and another one in the liquid of the recording chamber (see Fig. 2.1). The electrodes, connected to an amplifier (RK300 patch-clamp amplifier, Bio-Logic Company, Grenoble, France), enabled the monitoring of this resistance. Similarly to the work of Sakmann & Neher [144], we establish the relationship between the tip area, $A_{\text{tip}}$, and the measured resistance through a calibration using a scanning electronic microscope (SEM), ZEISS Ultra55. Fig. 2.3 shows a SEM image taken of a pipette tip. Pipettes with different tips matching our needs in the experiments with respect to particles diameters were SEM scanned and their resistances measured. Fig. 2.4 shows the experimentally measured data of resistance as function $A_{tip}$. In this data, the measured resistances ranged from 0.7 to $25.6\,M\Omega$. It appears that the points do not deviate significantly from the fitting curve, when the pipette resistance is within the range 0.7 to $4\,M\Omega$. Starting from $4\,M\Omega$, a scatter of values is observed which is probably due to the decreasing of the tip. A least squares curve was fitted to data using MATLAB fit function. The model used was $\ln(A_{\text{tip}}) = k \cdot \ln(R_{\text{pip}}) + b$, where the values coefficients were found as $k = -1.3$ and $b = 2.1$ with 95% confidence bounds. The obtained relation between tip area and pipette resistance reads, therefore:

$$A_{\text{tip}} = \frac{8.16}{R_{\text{pip}}^{1.3}}. \tag{2.2}$$

The pipette resistance ranged from $0.6\,M\Omega$ to $25\,M\Omega$, corresponding to tip diameters of $5\,\mu m$ down to $350\,nm$, respectively. In the present experiments, we set the target pipette diameter to $d_p = 0.45\,\mu m$ (the corresponding pipette resistance is $R_{\text{pip}} = 20\,M\Omega$) for $1\,\mu m$ particles,

---

[2]In this figure one can note a small "defect" that corresponds to the cross-section of a so-called filament. In this figure one can note a small "defect" that corresponds to the cross-section of a so-called filament. The purpose of this filament (which is a glass rod positioned at the inner wall of the capillary tube) is to prevent the formation of bubbles in the tube once the pipette is immersed in liquid. The section of this filament depends on the heat value used to pull pipettes and ranges from $2000\,nm^2$ for smaller pipettes up to $9000\,nm^2$ for bigger pipettes. This area does not exceed 3.7% of the total area and can be neglected.
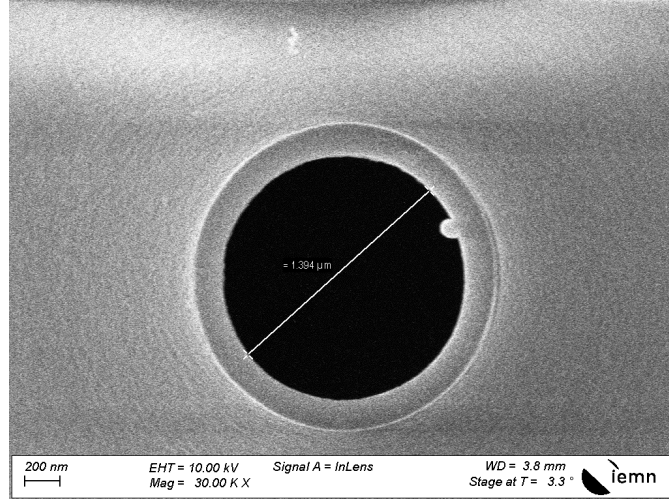
Figure 2.3: SEM Image (x30000) obtained for a pipette having a resistance of $3.5\,\text{M}\Omega$ and a tip diameter of $1.394\,\mu\text{m}^2$.
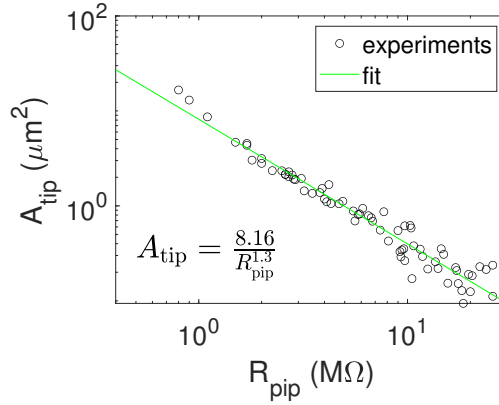


Figure 2.4: Experimental data (black points) and fitting curve (green line) for the tip area $A_{\text{tip}}$ as a function of pipette resistance $R_{\text{pip}}$.

$d_p = 0.6\,\mu\text{m}$ ($R_{\text{pip}} = 13\,\text{M}\Omega$) for $3\,\mu\text{m}$ particles, $d_p = 1\,\mu\text{m}$ ($R_{\text{pip}} = 6\,\text{M}\Omega$) for $6\,\mu\text{m}$ particles, $d_p = 1.3\,\mu\text{m}$ ($R_{\text{pip}} = 4\,\text{M}\Omega$) for $12\,\mu\text{m}$ particles. Substituting the pipette tip area calculated with these values using Eq.(2.2) and the maximum depression of $-800\,\text{mbar}$ into the Eq.(2.1), we obtain the maximum applied force of $F = 9\,\text{nN}$ for $1\,\mu\text{m}$ particles, $F = 16\,\text{nN}$ for $3\,\mu\text{m}$ particles, $F = 44\,\text{nN}$ for $6\,\mu\text{m}$ particles and $F = 75\,\text{nN}$ for $12\,\mu\text{m}$ particles.

## 2.2 Method

First, we evaluate the tip area, $A_{\text{tip}}$, of the pipette by measuring the resistance. Second, the pipette is approached to the surface of a microparticle creating a close contact between the pipette and the microparticle. In our case, the measured resistance was slightly increased when

touching the microsphere showing that no high resistance seal could be created between the glass and the microsphere. Thereafter, a defined negative pressure (ranged from $-1\,\mathrm{mbar}$ to $-800\,\mathrm{mbar}$) is applied through the pipette by means of our microfluidic pump. The pipette is then vertically uplifted at the constant velocity of $3\,\mathrm{\mu m/s}$ in the attempt to detach the microparticle from the substrate. If the microparticle does not detach from the substrate, the pipette is brought back on the top of the microparticle and larger depression applied. This procedure was repeated until the detachment was observed (Fig. 2.2) or we reached of the maximum depression provided by the microfluidic pump ($-800\,\mathrm{mbar}$). All pipette manipulations were made under microscopic observation (x100 lens, total magnification: x1000). The whole procedure was monitored and recorded by a CMOS camera (IDS UI-3250ML-M-GL) to assess the detachment of the microparticle. For the next run on another microparticle, a new micropipette is used.

## 2.3  Experimental results

In this section, we present the results of experiments carried out on polystyrene microspheres of different diameters ($1\,\mathrm{\mu m}$, $3\,\mathrm{\mu m}$, $6\,\mathrm{\mu m}$ and $12\,\mathrm{\mu m}$) which were contained in $2\,\mathrm{\mu L}$ droplet that dried for certain time ($1\,\mathrm{h}$, $24\,\mathrm{h}$, $48\,\mathrm{h}$ or $72\,\mathrm{h}$) at a controlled temperature of either $40\,^{\circ}\mathrm{C}$ or $50\,^{\circ}\mathrm{C}$. Each prepared sample was then characterised by the droplet containing particles of a given size, deposited on a coverslip that dried at a prescribed temperature and duration. We attempt to remove several different particles on each sample. In this procedure, we purposely investigated the detachment on isolated particles on the substrate to avoid any collective effect that could arise from clusters. To obtain one experimental curve, we perform measurements on at least two samples (obtained with the same particle size, dried under the same temperature for the same period of time) bringing the total number of attempts to detach a particle to 30 or more. Throughout this section, it will be shown that the detachment force can significantly vary for particles from the same sample. Therefore, to validate the patch-clamp technique, we have to ensure that the results are reproducible.

Fig. 2.5 (green and black dots) presents the results of the detachment force measurements on two samples for $12\,\mathrm{\mu m}$ particles dried for $24\,\mathrm{h}$ under a temperature of $50\,^{\circ}\mathrm{C}$. The $x$-axis shows the applied force (in nN), and the $y$-axis shows the percentage of particles that remain attached to the substrate at a corresponding applied force. We attempted to detach 16 particles from each sample. On sample 1, all of the attempts were successful, and give 16 green points in Fig. 2.5. On sample 2, only 13 out of 16 particles were removed at the maximum force we could apply with our setup. Then, the data from two samples was combined and gives the total data set (red crosses in Fig. 2.5) with 29 out of 32 particles being removed within the given applied force range. The experimental points from the total data set are fitted using MATLAB fit function. The fitting is done using nonlinear least squares method with the logistic function, which is typically used in literature to fit the adhesion curves (e.g., [60]):

$$f(x) = \frac{100(1+b)}{1 + b\exp^{-kx}} \tag{2.3}$$

where $x$ is the detachment force; $f(x)$ is the percentage of particles remaining on substrate, if the detachment force $x$ was applied. The fitting parameters are $k$ – the logistic growth rate and $b$ – the curve shape coefficient. We derive a mean force $x_{mean}$, that represents the force required to detach 50% of particles from the substrate, as follows

$$x_{mean} = -\frac{1}{k}\ln\left(2 + \frac{1}{b}\right) \tag{2.4}$$
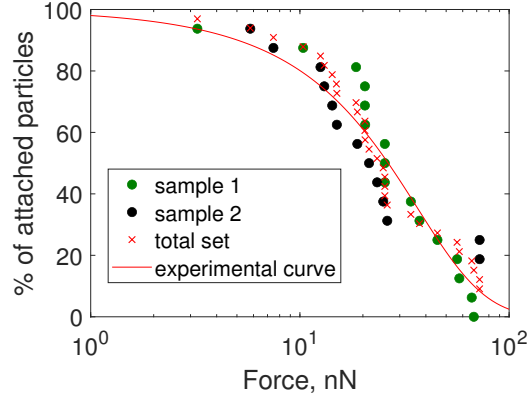
Figure 2.5: Percentage of attached particles as a function of applied force for $12\,\mu m$ particles dried for $24\,h$ under a temperature of $50\,°C$. Green and black points correspond to the experiments performed on the samples 1 and 2, respectively. Red crosses are the points from the total data set (i.e., summarized data from both samples). The red curve is obtained after fitting the total data set with Eq.(2.3).

Using this fitting, we obtain the following mean forces in our example (Fig. 2.5): $28.4\,nN$ for sample 1, $23.8\,nN$ for sample 2 and $26.4\,nN$ for the total data set. As we can see from Fig. 2.5, the experimental points may appear far from the fit for some percentage of attached particles, but the use of statistical curves "smoothes" this difference. Besides, particles of the same diameter of $12\,\mu m$ dried under same conditions require a detachment force ranging from $3\,nN$ up to $72\,nN$, and even under the applied force of $72\,nN$, 3 out of 32 particles were not removed, that is why at the maximum applied force we still have about 10% of attached particles. All of this indicates a wide data scattering and requires statistical approach. In what follows, we will use the mean force for data comparison along with the experimental curve.

### 2.3.1  Effect of temperature

We compared the detachment curves for particles of $1\,\mu m$, $6\,\mu m$, $12\,\mu m$ dried for $1\,h$ or $24\,h$ at a controlled temperatures of $40\,°C$ and $50\,°C$. The bottom temperature was set to $40\,°C$, because the oven we used can only heat, but not cool, and the outside temperature in summer can be around $35\,°C$. The upper temperature was set to $50\,°C$, as polystyrene particles can significantly deform at higher temperatures.

Fig. 2.6 (left) compares the detachment curves for $12\,\mu m$ particles dried for $24\,h$ at $40\,°C$ and $50\,°C$. The mean adhesion force is found $19.9\,nN$ for $40\,°C$, and $26.4\,nN$ for $50\,°C$. It appears then that the higher the drying temperature, the stronger the particle-substrate interactions. This increase in the mean detachment force is about 32% for a change in temperature by $10\,°C$. This variation is not significant if we consider the experimental data dispersion in the mean force observed between the two samples of Fig. 2.5. A more detailed discussion of data scattering is given in Appendix I.

Fig. 2.6 (right) shows the mean detachment force variation for particles of different sized dried for $1\,h$ or $24\,h$. According to this figure, the drying temperature slightly affects the mean deatchment force. Although, we only considered two different drying temperatures ($40\,°C$ and $50\,°C$), whose difference is not too important, the detachment force increases with the growth of the drying temperature for all particle sizes and drying times, except for $6\,\mu m$ particles dried for
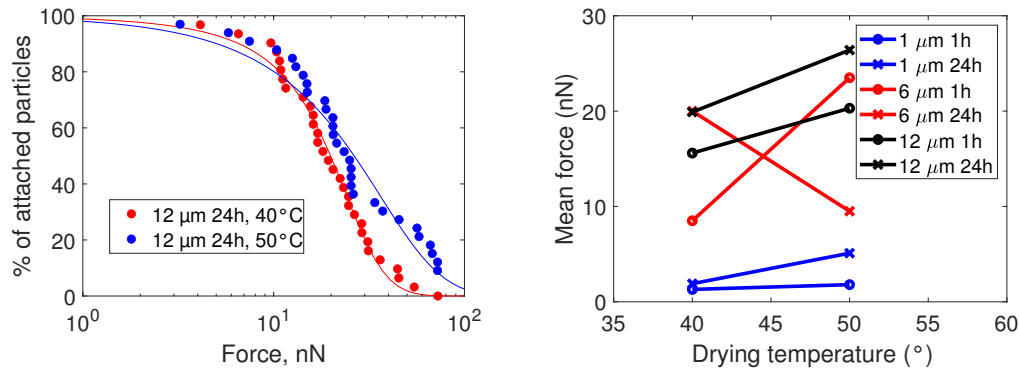
Figure 2.6: (left) Percentage of attached particles as a function of applied force for 12 μm particles dried for 24 h at different drying temperatures of 40 °C and 50 °C. (right) Mean detachment forces variation between 40 °C and 50 °C.

24 h.

Therefore, even if the drying temperature may seem to have some effect on the particle-substrate interaction, we cannot give a firm confirmation of this variation with the small temperature range tested associated with large data dispersion. However, there is a trend and for wider temperature range we may reasonably expect a more noticeable effect but further investigations are needed.

### 2.3.2 Effect of drying time

Now we compare how the drying time affects the adhesion. Droplets containing 12 μm particles were dried for 1, 24, 48 or 72 h at 50 °C. Fig. 2.7 (left) clearly shows the effect of drying time on the adhesion curves. The mean forces are 20.3 nN, 26.4 nN, 46.4 nN and 36.0 nN for 1 h, 24 h, 48 h or 72 h, respectively.

The longer the drying time is, the harder particles stick to the substrate, except for 72 h that seems to slightly decrease compared to data of 48 h. Considering that this decrease remains within the data uncertainty, this is probably the representation of a saturation of particle adhesion to the substrate. In other words, after 48 h, a further increase in drying time does not have a notable effect on the adhesion.

Fig. 2.7 (right) shows the effect of drying time on the mean detachment forces for all tested particle diameters. When comparing the data it appears that there is a trend of increase of adhesion with increasing time until 48 h except for 6 μm that shows first a substantial decrease. We have not been able to fully understand this behaviour and we refrain to make any speculative hypothesis at this stage. As it was mentioned above, it seems there is saturation on the effect of the drying time between 48 and 72 h. Some of the mean detachment forces even show a decrease at 72 h. For a detailed discussion of data scattering, please refer to Appendix I.

### 2.3.3 Effect of particle size

Finally, we studied the effect of particle size on the adhesion. Fig. 2.8 (left) presents the adhesion curves obtained for 1, 6 and 12 μm particles dried for 24 h at 50 °C. The results suggest that smaller the particles, less adherent they are.

In Fig. 2.8 (right), we observe the effect of particle size for all drying times (drying temperature is 50°). The larger the particle is, the more detachment force is required to remove it. The
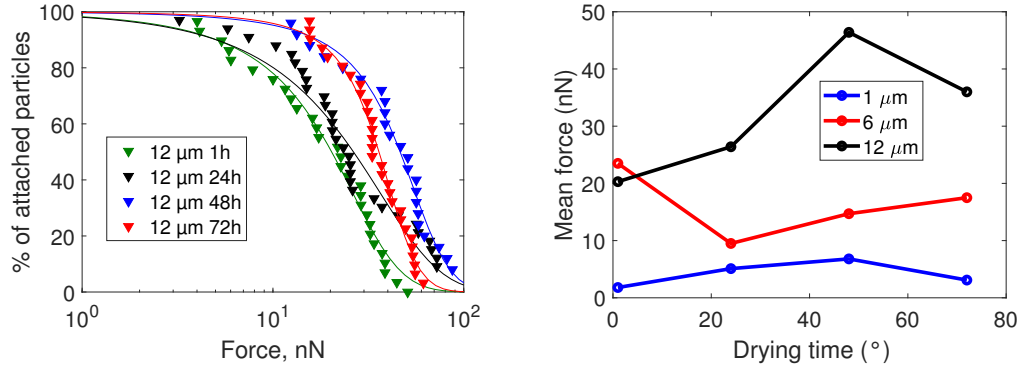
Figure 2.7: (left) Percentage of attached particles as a function of applied force for 12 µm particles dried at 50 °C for 1 h, 24 h, 48 h or 72 h. (right) Mean detachment force variation with the drying time for particles of 1, 6 and 12 µm in diameter dried at 50 °C.
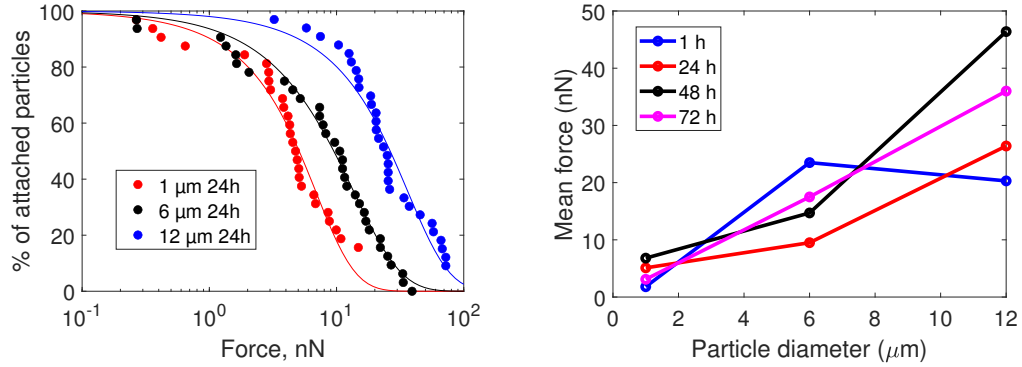


Figure 2.8: (left) Percentage of attached particles as a function of applied force for 1 µm, 6 µm, 12 µm particles dried at 50 °C for 24 h. (right) The dependency of the mean detachment force on the particle size. Particles dried at 50 °C for 1, 24, 48 and 72 h.

exception is 6 µm particles dried for 1 h. The details about data scattering are given in Appendix I.

### 2.3.4 Summary of experiments

The mean forces for different particle sizes and all drying times at 40 °C and 50 °C are summarized in Tables 2.1 & 2.2, respectively. We additionally performed the experiments with 3 µm particles dried at 40 °C in order to have more data for modelling (see next section).

With some exceptions that are put in red or green in Tables 2.1 & 2.2), we observe three trends:

- The detachment force increases with the drying temperature for all particle sizes and drying times, except for 6 µm particles dried for 24 h at 40 °C.

- The longer particles remain on the substrate, the harder it is to separate them from the substrate. As it was discussed above, it seems there is saturation on the effect of the drying

|        | 1h, 40°C | 24h, 40°C |
|--------|----------|-----------|
| 1 µm   | 1.3 nN   | 1.9 nN    |
| 3 µm   | 4.4 nN   | 7.4 nN    |
| 6 µm   | 8.5 nN   | 20.0 nN   |
| 12 µm  | 15.6 nN  | 19.9 nN   |

Table 2.1: Mean detachment forces for particles of a diameter of 1, 3, 6 or 12 µm and dried at 40°C for 1, 24, 48 or 72 h. The number in red is the exception (whose nature we do not fully understand) to the trends discussed above.

|       | 1h, 50°C | 24h, 50°C | 48h, 50°C | 72h, 50°C |
|-------|----------|-----------|-----------|-----------|
| 1 µm  | 1.8 nN   | 5.1 nN    | 6.8 nN    | 3.1 nN    |
| 6 µm  | 23.5 nN  | 9.5 nN    | 14.7 nN   | 17.5 nN   |
| 12 µm | 20.3 nN  | 26.4 nN   | 46.4 nN   | 36.0 nN   |

Table 2.2: Mean detachment forces for particles of a diameter of 1, 6 or 12 µm and dried at 50°C for 1, 24, 48 or 72 h. The number in red (if we do not fully understand) or green (if we suppose the saturation on the drying time effect) are the exceptions to the above-mentioned trends.

time between 48 and 72 h. Some of the mean detachment forces even show a decrease at 72 h.

- We observe the effect of particle size for both drying temperatures, 40°C and 50°C and for all drying times. The larger the particle is, the more detachment force is required to remove it. The two exceptions are for 6 µm particles dried for 24 h at 40°C and 6 µm particles dried for 1 h at 50°C.

## 2.4 Contact radius measurements

As it was described above, the adhesion force $F_{ad}$ for a given particle radius $R$ depends on adhesion energy $w$ (JKR model) or Hamaker constant $H$ (DMT model). None of the latter parameters are known and have to be worked out experimentally from measurements of the contact radius $a$ expressed in Eqs. (1.13)&(1.20). Thus, to validate the choice of the model, we performed measurements of the contact radius $a$. It has to be noted that to evaluate $F_{ad}$ in either JKR or DMT model, one needs the value of the effective Young modulus with the factor $4/3 - K$ (Eq.(1.2)) on the top of measurements of $a$. We experimentally measured the Young modulus of the microparticles $E_p$ and used the typical values of $E_s$ in the literature for the coverglasses.

The Young modulus of polystyrene particles $E_p$ was measured with AFM (Bruker Dimension Icon) in PeakForce mode and the value was found to be around 3 GPa. For polystyrene, the Poisson's ratio $\nu_p$ was found to be 0.34 to 0.35 for temperatures up to 80°C [111]. The Young modulus of glass typically varies between 40 GPa and 90 GPa [82] and the Poisson's ratio lies between 0.1 and 0.4 [139]. In the models, we took the values $E_s = 70$ GPa and $\nu_s = 0.22$ for glass coverslip and $E_p = 3$ GPa and $\nu_p = 0.34$ for particle, which are within the corresponding ranges. According to Eq.(1.2), $K = 4.3$ GPa. In the present experiments, only the particle experiences a significant deformation as the Young modulus of polystyrene is smaller by one order of magnitude than the glass substrate one.

The contact radius between a typical polystyrene particle with a glass coverslip was measured using a scanning electronic microscope (SEM) (Fig. 2.9). The procedure used to measure the

contact area was as follows. First, we traced a line on one side of the glass coverslip with a diamond tip. Second, we deposit a 2 µL droplet on the other side of the glass coverslip pre-cleaned with ethanol so that the scratch stays under the droplet. Then, we let the droplet evaporate at 20 °C for 1 h instead of 40 °C that we used when dried samples for the adhesion force measurements[3]. After that, we break the glass coverslip by the traced line, and the break passes through the droplet leftovers. Finally, we put the glass coverslip in SEM (ZEISS Ultra55), in such a way that the camera observes the coverslip edge with droplet leftovers. We were unable to measure the contact radius for isolated particles as they are detached by electron beam soon after being in SEM focus. So, we could only measure the contact radius for clustered particles (i.e., particles closely attached to the neighboring particles as in Fig. 2.9). It is to note that since clustered particles are in close contact with each other, they experience deformation (elastic or plastic) in the contact zone. The difference in contact radius between an isolated and a clustered particle arises mainly from the deviation from the spherical shape of the latter. Since this deviation due to the presence of neighboring particles is small enough (we estimate it to be of the order of 10%), we suppose that the resulting particle-substrate deformation for a clustered particle will be of the same order of magnitude as that for an isolated one. Additionally, in our measurements, we are trying to select the least deformed particles.
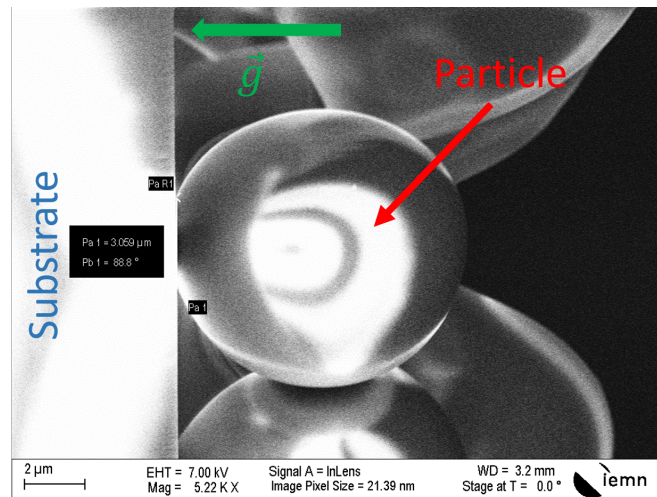


Figure 2.9: SEM image of 12 µm polystyrene particle in contact with the glass substrate. The contact radius is 1.53 µm.

We measured at least 10 particles of each diameter (1 µm, 3 µm, 6 µm, 12 µm). The measured contact radii are presented in Fig. 2.10. The measured contact radii may vary by up to 34% from the average values for particles of 1 µm, 3 µm and 6 µm in diameter and up to 52% for 12 µm particles. The standard deviation is significant for all particle sizes. This variation in contact radii can partially explain the observed wide range of adhesion force.

---

[3]The SEM measurements were performed in IEMN, while the detachment force experiments were carried out in the biological department. IEMN did not have ovens with the required temperature ranges; the only options available had higher temperature ranges that could potentially melt our particles.
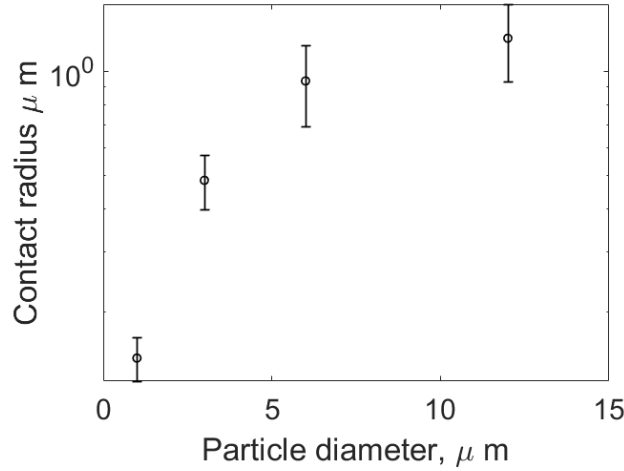
Figure 2.10: Contact radius measurements for different particle diameters. The error bar represents the standard deviation.

## 2.5 Modelling

In the current work, we measured the force required to detach a particle, $F_d$. On the other hand, the models of DMT and JKR predict the adhesion force $F_{ad}$. By assuming that only adhesion impedes the separation of a particle from the substrate, we can invoke that $F_{ad} = F_d$. We can also notice that none of the models takes into account the dependence of adhesion force on the temperature or drying time. For the time being, in the models we will use the case of different size particles dried for $1\,\mathrm{h}$ at $40\,°\mathrm{C}$ (Table 2.1). In this case, the temperature and the drying time have the weaker effect among all cases in consideration.

Below, we confront the results from our experiments with the JKR and DMT models. To this end, we use the previously found $K = 4.3\,\mathrm{GPa}$, and we fit the adhesion force using the nonlinear least squares method with fitting parameters $w$ and $H$ for the models of JKR (Eq.(1.16)) or DMT (Eq.(1.22)), respectively.

### 2.5.1 JKR modelling

If we fit the adhesion force with the Eq.(1.16) with the surface energy as a fitting parameter, we obtain $w = 5.7 \times 10^{-4}\,\mathrm{J/m^2}$ which is smaller at least by two orders of magnitude compared to any reported data in the literature (Table 1.1). For instance, literature reports values for the adhesion energy $w$ of polystyrene particles: $w = 0.32\,\mathrm{J/m^2}$ (silicon substrate [137]) and $w = 0.068\,\mathrm{J/m^2}$ (polyurethane substrate [135]). Our experimental results with the fitting curve are presented in Fig. 2.11 (left).

With the obtained adhesion energy $w = 5.7 \times 10^{-4}\,\mathrm{J/m^2}$, it is possible to predict the contact radius $a$ according to Eq.(1.13). This is shown in Fig. 2.11(right). In this figure the red line corresponds to fit with the model and the circles representing the experimentally obtained mean adhesion force with the error bars showing the force required to detach 10% (lower limit) up to 90% (upper limit) of particles from the substrate. One can see that the model and experiments do not match and show difference of several orders of magnitude.
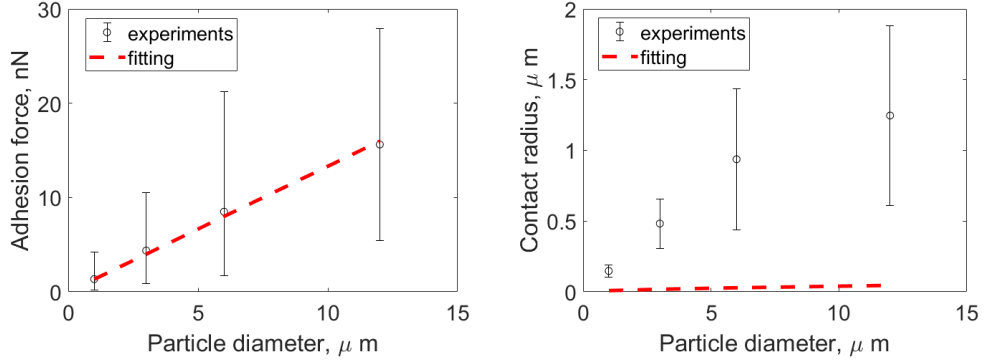
Figure 2.11: Fitting of adhesion force (left) and contact radius (right) with the same adhesion energy $w = 5.7 \times 10^{-4}\,\mathrm{J/m^2}$ using JKR model.

### 2.5.2   DMT modelling

Now we fit the adhesion force with the Eq.(1.22) using the Hamaker constant as the fitting parameter. The separation distance $z_0$ was set to $4 \times 10^{-10}\,\mathrm{m}$. The Hamaker constant obtained is $H = 2.6 \times 10^{-21}\,\mathrm{J}$ (Fig. 2.12, left). The Hamaker constants for polystyrene and glass in water medium obtained in different studies were reported by Visser [171] in which large discrepancy are observed. If we calculate the Hamaker constant for the polystyrene-glass interaction in water from the presented data, we obtain $H \sim 10^{-20}\,\mathrm{J}$ (Eq.(1.23)). Hence, the Hamaker constant obtained by fitting seem to be correct.

However, when again deriving the contact radius using prediction from DMT model (Eq.(1.20)), values obtained are far from experiments (Fig. 2.12, right).
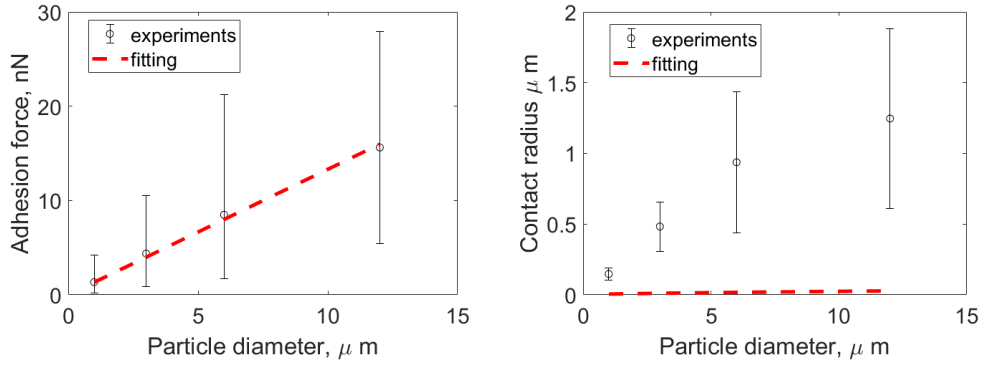


Figure 2.12: Fitting of adhesion force (left) and contact radius (right) with the same Hamaker constant $H = 2.6 \times 10^{-21}\,\mathrm{J}$ using DMT model.

### 2.5.3   Tabor's and Maugis parameters

After obtaining the Hamaker constant $H = 2.6 \times 10^{-21}\,\mathrm{J}$, we calculate the molecular force potential $\Phi = 4.3 \times 10^{-4}\,\mathrm{J/m^2}$. With the interaction energy $\Delta\gamma = 5.7 \times 10^{-4}\,\mathrm{J/m^2}$ for the JKR model and $\Delta\gamma = 4.3 \times 10^{-4}\,\mathrm{J/m^2}$ for the DMT model, we calculate the Tabor's parameter $\mu_T$

and the Maugis parameter $\lambda_M$ according to Eqs.(1.24)&(1.25). For any particle radius used in the experiments, both $\lambda_M$ and $\mu_T$ are of the order of 0.1 for both interaction energies $\Delta\gamma = 5.7 \times 10^{-4}\,\mathrm{J/m^2}$ (JKR) and $\Delta\gamma = 4.3 \times 10^{-4}\,\mathrm{J/m^2}$ (DMT). This suggest that the DMT model should be applied in our case.

## 2.6  Discussion and conclusion

In the first part of the current work, we presented a patch-clamp based technique for the detachment force measurement. We measured the detachment force for particle of different diameters dried at either $40\,^\circ$C or $50\,^\circ$C for $1\,\mathrm{h}$ up to $72\,\mathrm{h}$. We observed a wide range of measured detachment force values regardless particle size or drying conditions.

In the second part, we tested the models, namely JKR and DMT, from the literature on our experimental data. To end this, we measured the contact radius of particles lying on their substrates. The comparison of the experiments with either model exhibited disagreements. We, hereafter, may enumerate the possible reasons of these differences.

First, the measured contact radius do not probably represent the reality. Indeed, experimentally, the surface of the particles and the substrates are probably far from being ideally smooth as considered in the models. This would rather induce contacts on the asperities (convex parts of a surface), while on other places there is no contact (concave parts of the surface) [129]. Therefore, the effective contact area may be smaller than the measured one. Second, in our case, the particles, initially contained in a droplet, are deposited on the substrate from the evaporation of the liquid in which they were in suspension. In the final stages of the evaporation process, liquid bridges form around the particle foot. This induces capillary forces acting on the particles that may provoke strong deformations at small scales and increase in contact radius by up to 300%. However, it is still not enough to explain the disagreement with the models, which is two orders of magnitude.

Another remark that can be made about the experiments, is the relatively large data dispersion of measured detachment forces. Of course, the surface asperities and the effective contact radius that we just described, could be part of the data dispersion explanations. However, we think that the wide range of the detachment force and also the disagreement with the models are derived from a phenomena that we did not suspect when we ran the experiments. Indeed, we recently realized that air bubbles could be trapped underneath a particle when immersing the latter after the drying step, to perform the patch-clamp experiments. This phenomena will be deeply studied in the next chapter.

In conclusion, we may state that the patch-clamp technique seems convenient to measure the force to detach a particle from its substrate, even though care should be taken. The present results show large dispersion and that make difficult to draw firm conclusions even though trends are seen, for instance, on the drying time. Further experiments are also needed but above all, we think that the patch-clamp technique, at least when using the present procedure, should be limited to configurations where both the particles and the substrates are hydrophilic. This would correspond to the situation where it is highly unlikely that a bubble can be entrapped between the particle and the substrate as it will be demonstrated in the next chapter.

## 2.7  Perspectives

The presented patch-clamp technique can also be used to measure the detachment force for spores. Fig. 2.13 shows the results of experiments carried out for drying times of $1\,\mathrm{h}$ for hydrophobic spores (two different strains, Bs py79 spsA and Bc 98/4 pyl300, were tested) and for

1 h and 24 h for hydrophilic spores (Bs py79 GPF) on hydrophilic coverglasses. The reason there is no data for a drying time of 24 h for hydrophobic spores is that the setup could not deliver enough force to detach these spores from the substrate. Also, we could only detach about 30% of population after 1 h of drying. After 24 h of drying, the detachment within our pressure range was impossible for these spores. Nevertheless, the effect of drying time for the same spores is much more clearly noticeable.
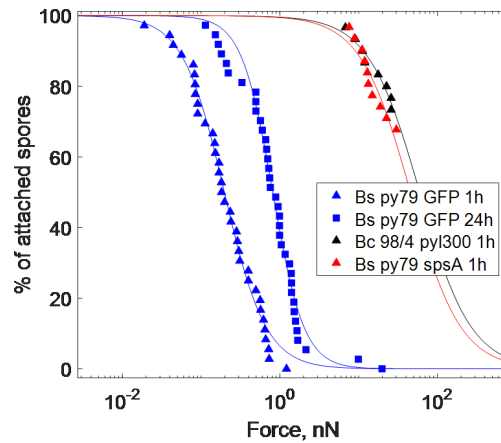


Figure 2.13: Percentage of detached particles and spores as a function of applied force. Different colors correspond to different spores.

# Chapter 3

# Study of an air bubble under a particle

In Chapter 1, we discussed about interaction forces between a microparticle and a substrate as well as the existing adhesion models for particle. Altough the effect of liquid bridges on the particle adhesion was studied, the inverse situation of an air bubble trapped between the particle and the substrate was not considered. This situation may well occur at the substrate-liquid immersion throughout, for instance, a classical cleaning procedure.

A bubble can be easily trapped under a particle, if we add liquid to a dry particle stuck on a substrate, especially if one of the involved surfaces is hydrophobic. Another possible option for a bubble entrapment is the presence of dissolved gases in liquid. If liquid releases the excess of gas molecules, the latter may coalesce and form bubbles.

In this chapter, we show how a bubble can greatly modify the attachment force of a particle to the substrate depending on their associated wetting characteristics.

To investigate the problem associated with such situation, we developed a theoretical model, ran numerical computations and carried out experiments. The model is based on considerations of involved forces in static situations.

## 3.1   Models

As it was mentioned before, the adhesion force is a combination of several different mechanisms. However, for simplicity, the present models only consider the adhesion caused by the presence of an air bubble without any other forces in the system. Although, this may not reflect the whole reality, it gives insights of the contributing role of a trapped bubble on the retaining or repulsing a particle from a substrate.

Here, only micrometric particles of a radius of $R \lesssim 10\,\mu\mathrm{m}$ are considered. The Bond number, $\mathrm{Bo} = \rho g R^2/\gamma$, comparing gravity to capillary effects remains small ($\mathrm{Bo} \lesssim 10^{-4}$ for typical values of liquid density ($\rho \sim 10^3\,\mathrm{kg/cm^3}$) and surface tension ($\gamma \sim 10^{-1}\,\mathrm{N/m}$)), and, therefore, the gravity can be neglected. The liquid and air pressure, $p_L$ and $p_A$, are thus supposed to be uniform.

In this section, we will first present a theoretical energy-based model that predicts the bubble configuration after particle detachment from its substrate, i.e., bubble either sticking to the particle, to the substrate or both. Second, we will present a numerical model that estimates the bubble-induced force with respect to particle and substrate wetting characteristics.

### 3.1.1 Energy analysis model

This model was mainly developed by our colleague Harunori Yoshikawa from Côte d'Azur University.

The aforesaid objective of the present study is to investigate the conditions for particle removal from a substrate while a bubble is trapped in between. Three possible configurations can be identified for particle detachment: (i) a detachment with the entire bubble (Fig. 3.1a), (ii) a detachment without the bubble (Fig. 3.1b), (iii) or a mixed case where the bubble splits between the particle and the substrate (Fig. 3.1c).
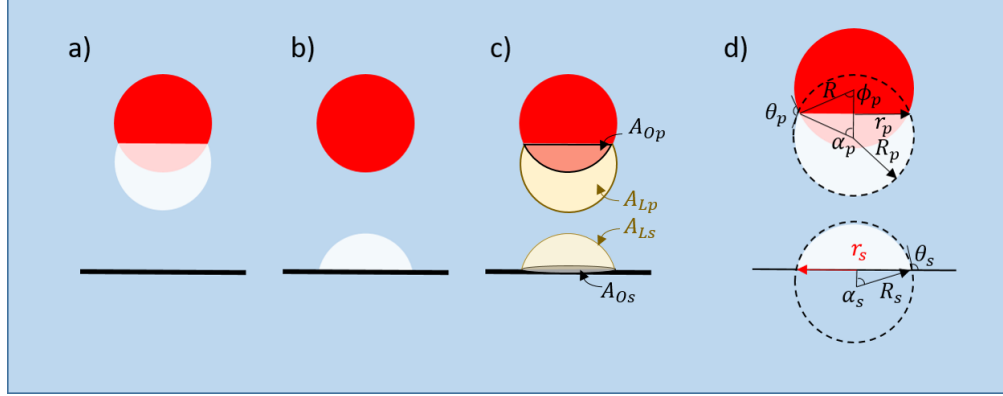


Figure 3.1: Definitions of the geometries of two bubbles after the detachment of a particle. (a) Detachment with the bubble, (b) detachment without the bubble, (c) bubble splits between the particle and the substrate. (d) Definitions of the geometry of the two bubbles scenario.

In this subsection, we investigate the possible detachment scenario that may occur with respect to the wetting properties of solid surfaces, i.e., those of the particle and the substrate. The study is based upon equilibrium states where the real system complexity such as eventual contactline pining and, hence, the contact angle hysteresis is disregarded for the sake of simplicity. Furthermore, the model does not provide any information of the required force to detach a particle from a substrate. Nevertheless, it will give us insights of the possible configuration that may occur in the removal of a particle under which a bubble is trapped.

Although the interfacial dynamics involved in the particle detachment process is highly nonlinear and may depend on the motion of detaching particle and its history, the bubbles configuration of the minimum energy could be considered as a representative state of the bubble after the particle detachment.

We assume that the bubble only contains a non condensing ideal gas. The total surface energy $U$ of a stationary particle-bubble system shown in Fig. 3.1d) is given by

$$
U = \overbrace{\underbrace{\gamma A_{Lp}}_{\substack{\text{creation of an}\\\text{liquid-gas interface}}} + \underbrace{\gamma_{Op}A_{Op} - \gamma_{Lp}A_{Op}}_{\text{creation of a dry interface}}}^{\text{bubble on the particle}} + \overbrace{\underbrace{\gamma A_{Ls}}_{\substack{\text{creation of an}\\\text{liquid-gas interface}}} + \underbrace{\gamma_{Os}A_{Os} - \gamma_{Ls}A_{Os}}_{\text{creation of a dry interface}}}^{\text{bubble on the substrate}} + U_{\text{ref.}},
$$

$$(3.1)$$

where $A_L$ and $A_O$ stand respectively for the areas of liquid-gas and liquid-solid interfaces of a bubble. The surface energy densities of wetted and dry solid surfaces are denoted by $\gamma_L$ and $\gamma_O$, respectively. The subscripts $p$ and $s$ indicate to which solid surface, either particle ($p$) or

substrate ($s$), the quantities are concerned with. The energy $U_{\text{ref.}}$ refers to the system with no bubble, which we take as a reference.

Invoking the Young-Dupré equations, $\gamma_{Op} - \gamma_{Lp} = \gamma \cos\theta_p$ and $\gamma_{Os} - \gamma_{Ls} = \gamma \cos\theta_s$, we cast Eq.(3.1) into

$$U = \gamma \left( A_{Lp} + A_{Op} \cos\theta_p \right) + \gamma \left( A_{Ls} + A_{Os} \cos\theta_s \right) + U_{\text{ref.}}. \tag{3.2}$$

For a given surface tension $\gamma$, given contact angles $\theta_p$ and $\theta_s$, and a given radius of particle $R$, the energy $U$ depends only on the radii $r_p$ and $r_s$ of bubble on the particle and the substrate (Fig. 3.1d), $U = U(r_p, r_s)$, since the areas $A_{Li}$ and $A_{Oi}$ ($i = p, s$) are related geometrically to these radii and $\theta_p$ and $\theta_s$:

$$A_{Lp} = 2\pi R_p^2 (1 + \cos\alpha_p), \tag{3.3}$$

$$A_{Op} = 2\pi R^2 (1 - \cos\phi_p), \tag{3.4}$$

$$A_{Ls} = 2\pi R_s^2 (1 - \cos\alpha_s), \tag{3.5}$$

$$A_{Os} = \pi R_s^2 \sin^2\alpha_s, \tag{3.6}$$

where $R_p$, $R_s$, $\alpha_p$, $\alpha_s$ and $\phi_p$ are geometrical parameters defined in Fig. 3.1d) and given by $R_p = r_p / \sin\alpha_p$, $R_s = r_s / \sin\alpha_s$, $\alpha_p = \theta_p - \phi_p$, $\alpha_s = \pi - \theta_s$ and $\phi_p = \sin^{-1}(r_p/R)$.

On the other hand, as bubbles contain only non condensable gas, they are subject to the mass conservation:

$$p_p V_p + p_s V_s = p_0 V_0, \tag{3.7}$$

where $p_i$ and $V_i$ are the pressure and volume of the bubble on the solid surface $i$ ($= p, s$). The volume $V_0$ is that of the given amount of gas when it is maintained at the surrounding pressure $p_0$.

The bubble pressure $p_i$ is determined by the pressure balance at the interface: $p_i - 2\gamma/R_i = p_0$. The bubble volumes $V_p$ and $V_s$ only depend on, respectively, $(R, \theta_p, r_p)$ and $(\theta_s, r_s)$:

$$V_p = \frac{\pi R_p^3}{3}(1 + \cos\alpha_p)^2 (2 - \cos\alpha_p) - \frac{\pi R^3}{3}(1 - \cos\phi_p)^2 (2 + \cos\phi_p), \tag{3.8}$$

$$V_s = \frac{\pi R_s^3}{3}(1 - \cos\alpha_s)^2 (2 + \cos\alpha_s). \tag{3.9}$$

Thus, for a given $(\gamma, \theta_p, \theta_s, R)$, Eq.(3.7) represents a relationship between $r_p$ and $r_s$ that has to satisfy the mass conservation and can be rewritten as:

$$\Psi(r_p, r_s) = 0. \tag{3.10}$$

Seeking the radius values $(r_{p,\text{min}}, r_{s,\text{min}})$ minimizing $U$ (Eq.(3.2)) under the constraint (Eq.(3.10)) infer the representative configuration after the particle detachment: if $r_{s,\text{min}} = 0$, the bubble detaches from the substrate with the particle (Fig. 3.1a); if $r_{p,\text{min}} = 0$, the bubble remains at the substrate (Fig. 3.1b); if both $r_{s,\text{min}}$ and $r_{p,\text{min}}$ don't vanish, two daughter bubbles are attached to the particle and substrate (Fig. 3.1c).

Figs. 3.2a and 3.2b summarize in two maps the values of respectively $r_{p,\text{min}}$ and $r_{s,\text{min}}$ in the $\theta_p$-$\theta_s$ plane for a given $(R, \gamma, p_0, p_0 V_0)$. These maps were computed for the ratio of liquid to capillary pressure of $p_0 R/\gamma = 2$ and the bubble-particle size ratio $p_0 V_0 / \gamma R^2 = 0.4$. In these maps, the gray areas indicate $r_p = 0$ in Fig. 3.2a and $r_s = 0$ in Fig. 3.2b. They respectively represent the situations illustrated in Fig. 3.1a&b. The configuration Fig. 3.1c with the presence of daughter bubbles can be easily worked out by taking the difference of two maps of Fig. 3.2a&b. The red lines in Fig. 3.2 indicate the wetting characteristics explored in the experiments reported below.
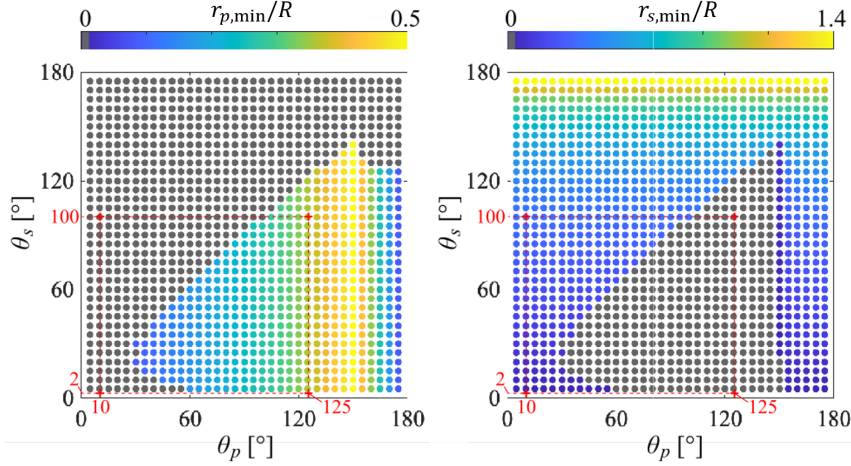
Figure 3.2: Bubble foot radii $r_{p,\min}$, $r_{s,\min}$ minimizing the surface energy $U$ for $p_0 R/\gamma = 2$, $p_0 V_0/\gamma R^2 = 0.4$.

For hydrophobic particles $\theta_p = 125°$, it appears that for the substrate with $\theta_s = 2°, \theta_s = 100°$, the system would show a bubble fully sticking to the particle in the detachment process (Fig. 3.2a). For hydrophilic particles $\theta_p = 10°$, in contrast, we have $r_p = 0$, i.e., the entire bubble remains on the substrate after the detachment (Fig. 3.2b). These values of $\theta_p$ and $\theta_s$ are selected according to the materials used in experiments described below. The configuration Fig. 3.2c is achieved for any substrate when we deal with highly hydrophobic particles $\theta_p \geq 160°$ and for hydrophobic particles with $\theta_p = 155°$ placed onto a substrate having $\theta_s \geq 25°$.

The energetic consideration presented above remains of qualitative nature. The radii $r_p$ and $r_s$ minimizing the energy $U$ depend on the dimensionless pressure $p_0 R/\gamma$ and the dimensionless amount of air $p_0 V_0/\gamma R^2$. However, we have no access to the latter information by the present experiment for comparison. Furthermore, the theory does not take into account the dynamics during the particle detachment that may also affect the final bubble configuration. These points would be considered by future theoretical and experimental work.

### 3.1.2   Force analysis model

In this subsection, we investigate the force that a bubble may apply on a particle and explore the circumstances in which this force can act as an additional force for retaining or repulsing a particle from a substrate. Below, we first present the equations modeling a bubble trapped between a particle and a substrate. In a second time, numerical computations based on these equations are carried out.

**Forces acting on the particle**

We consider a spherical particle of a radius $R$ immersed in a liquid and being in contact with a solid wall at equilibrium (Fig. 3.3). We introduce $r$ – coordinate along the solid wall, and the central axis $z$ perpendicular to the wall. We assume an axisymmetric system, i.e., the shape of the bubble is invariant against any rotation around the particle central axis $z$. An air bubble is plugged between the particle and the wall with a given distance $r_s$ of the contact line from the symmetry axis (Fig. 3.3). The surfaces of the particle and the wall are smooth and their

wettabilities are characterized by the static contact angles $\theta_p$ and $\theta_s$, respectively. For simplicity, at this stage, the hysteresis of the contact angle is neglected.

The angle formed between $z$-axis and the radius of the particle drawn from its center to the contact line (in studies of liquid bridges under a particle [116, 3], this angle is so-called "filling angle") is denoted by $\varphi$. The radius $r_p$ represents the distance of the contact line from the symmetry axis: $r_p = R\sin\varphi$. A constant $\beta$ indicating the angle of the particle-liquid-bubble interface measured from the symmetry axis is introduced for brevity: $\beta = \pi/2 - (\theta_p - \varphi)$.
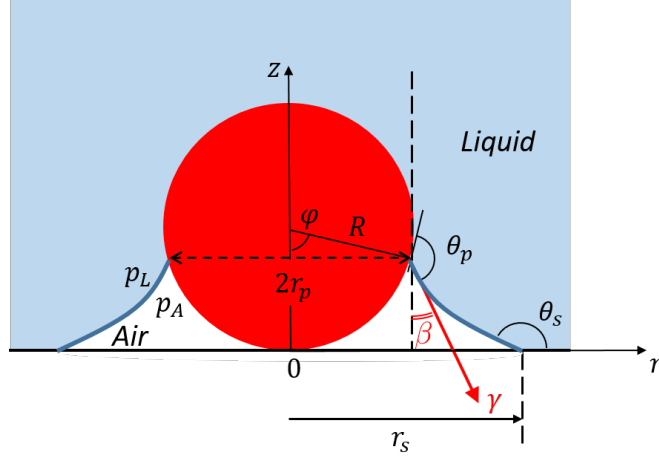


Figure 3.3: Air bubble trapped underneath a particle of radius $R$ with the filling angle $\varphi$. The liquid-air interface respects the liquid contact angle on both the particle $\theta_p$ and the substrate $\theta_s$. In cylindrical coordinates $(r, z)$, the triple contact line is located at $r = r_s$ and $r = r_p$ for the substrate and the particle, respectively.

Considering only capillary forces, the $z$-component of the force acting on a particle at the particle-bubble interface is given by

$$
\begin{aligned}
F_p = F_{p,l} + F_{p,c} &= -\pi r_p^2 \Delta p - 2\pi r_p \gamma \cos\beta \\
&= -\pi R^2 \sin^2\varphi \Delta p - 2\pi R\gamma \sin\varphi \sin(\theta_p - \varphi),
\end{aligned}
\tag{3.11}
$$

where $F_{p,l}$ is the Laplace pressure force, $F_{p,c}$ is the tensile force acting on the particle contact line at $r = r_p$, $p_L$ is the liquid pressure, $p_A$ is the air pressure and $\Delta p = p_L - p_A$ is the pressure difference.

We compute $F_p$ for given contact angles $(\theta_p, \theta_s)$ at a chosen distance $r_s$ from the symmetry axis. The contact angle position $\varphi$, involved in Eq.(3.11) as well as the pressure difference $\Delta p$ are determined from the shape of the bubble governed by the Young-Laplace equation:

$$
\Delta p = -\gamma \left(\nabla \cdot \vec{n}\right),
\tag{3.12}
$$

where $\vec{n}$ is the unit normal vector to the interface, and $\nabla \cdot \vec{n}$ supposes a divergence of $\vec{n}$ over dimensional coordinates. On the geometrical basis, in cylindrical coordinates, $\vec{n}$ can be expressed as a function of air-liquid interface $r = f(z)$ as

$$
\vec{n} = \frac{\vec{e}_r - f_z \vec{e}_z}{(1 + f_z^2)^{1/2}},
\tag{3.13}
$$

where $f_z = \frac{df}{dz}$ and we have assumed a bubble axisymmetric around the $z$-axis.

Substituting Eq.(3.13) into Young-Laplace equation (3.12), one obtains the equation determining the shape of the air-liquid interface

$$\frac{f_{zz}}{(1+f_z^2)^{3/2}} - \frac{1}{f\,(1+f_z^2)^{1/2}} = \frac{\Delta p}{\gamma}. \tag{3.14}$$

This equation is to be solved under the boundary conditions at the substrate and particle surfaces:

$$f = r_s, \quad f_z = \cot\theta_s, \quad \text{at } z = 0, \tag{3.15}$$

$$f_z = -\cot(\theta_p - \varphi), \quad \text{at } z = R(1 - \cos\varphi). \tag{3.16}$$

The pressure $p_A$ is computed as

$$p_A = p_L - \Delta p, \tag{3.17}$$

where $\Delta p$ is obtained by integrating Eq. (3.14) using boundary conditions expressed in Eq. (3.15) & Eq. (3.16) and the pressure $p_L$ is set at $1 \times 10^5\,\text{Pa}$, assuming a pressure in liquid close to the atmospheric pressure.

**Numerical solution**

The geometry of the system, set by the parameters $(\theta_p, \theta_s, r_s)$, enables the determination of $(\Delta p, \varphi)$ through the integration of Eq. (3.14) with respect to boundary conditions (3.15) & (3.16). We solve the problem numerically using shooting method. First, we choose $r_s$, for which we search for the solution. For the $k$-th iteration, we use $\Delta p^{(k-1)}$ (obtained from the $(k-1)$-th iteration or supposed, if $k = 0$) to integrate the equation (3.14) with the boundary conditions (3.15). The integration stops when the solution crosses the particle at some point. At this point, we calculate the filling angle $\varphi$ and $\psi(\Delta p^{(k-1)}) = f_z + \cot(\theta_p - \varphi)$, that corresponds to the boundary condition at the particle surface (3.16). To find a root of $\psi(\Delta p) = 0$, we use Newton's method with the relaxation coefficient 0.5. Such pressure difference $\Delta p^{(n)}$, satisfying $|\psi(\Delta p^{(n)})| < \varepsilon$ and $|\Delta p^{(n)} - \Delta p^{(n-1)}| < \varepsilon$, is the required pressure difference, and the corresponding $f(z)$ describes the meniscus shape. We repeat the same procedure for a wide range of $r_s$, as the experimental $r_s$ is unknown.

The force $F_p$ (Eq. (3.11)) is, then, computed and its positive or negative contribution on holding a particle on the substrate is deduced.

Semi-analytic solution of the boundary value problem (3.14) with boundary conditions (3.15-3.16) was proposed by Orr *et al.* [116] in 1975.

## 3.2   Numerical results

In the following, we investigate the effect of various wetting properties of the particle and the substrate on $F_p$. The results will then enable us to cast the positive or negative role of $F_p$, hence the bubble, in holding the particle on the substrate. The variation of wetting properties is done by fixing $\theta_p$ and varying $\theta_s$. In the coming paragraphs, we will first study the case of a hydrophobic and then hydrophilic particle. Hydrophobic and hydrophilic characteristics are accounted for the particle by setting $\theta_p$ values to 125° and 50°, respectively. The value of $\theta_p = 125°$ was chosen as it matches the wetting property of the particles tested experimentally and which data will be presented later in this thesis. With respect to hydrophilic property represented by $\theta_p = 50°$ value, it is arbitrary chosen but in such a way to reduce the numerical difficulties as low $\theta_p$

values could not provide mathematical solutions satisfying the boundary conditions. All the numerical computations are performed for a particle of a radius of $R = 1\,\mu m$ surrounded by water ($\gamma = 0.073\,N/m$).

### 3.2.1 Hydrophobic particle ($\theta_p = 125°$)

Fig. 3.4 illustrates the shape of the air-liquid interface in three different cases of wetting degree of the substrate characterized by contact angles $\theta_s = 100°$ (blue line), $\theta_s = 50°$ (pink line) and $\theta_s = 10°$ (black line). In these example, the position of the contact line on the substrate is fixed here at $r_s = 0.5\,\mu m$. One can see that the interface shape changes dramatically depending on
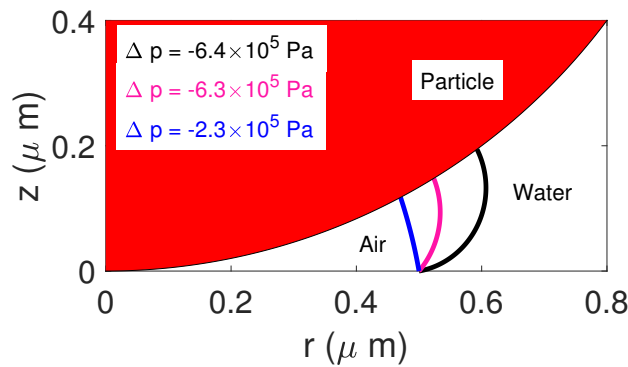


Figure 3.4: Shape of the air-liquid interface between a hydrophobic particle ($\theta_p = 125°$) and a hydrophobic substrate with $\theta_s = 100°$ (blue line), a hydrophilic substrate with $\theta_s = 50°$ (pink line) or $\theta_s = 10°$ (black line). For all these interfaces, $r_s = 0.5\,\mu m$.

the substrate wettability $\theta_s$. For a given $r_s$, it is obvious that the bubble volume is decreasing with the growth of $\theta_s$. The pressure difference $\Delta p$ reflects the wettability of the substrate: for both hydrophilic substrates, it is $\Delta p \approx -6 \times 10^5\,Pa$, while for the hydrophobic substrate $\Delta p \approx -2 \times 10^5\,Pa$, which is about three times less.

For fixed $\theta_p = 125°$, we vary both, $\theta_s$ and $r_s$ to study their effect on $F_p$. The contact angles range from hydrophilic $\theta_s = 2°$ to hydrophobic $\theta_s = 140°$. This range was chosen with respect to exploitable computational solutions. The position of the contact line on the substrate $r_s$ is varied from $r_s = 0.05\,\mu m$ to $r_s = 1\,\mu m$. Fig. 3.5 shows the map of variation of $F_p$ as a function of $r_s$ and $\theta_s$. The red color on the map means that the force induced by bubble is directed up, i.e., would facilitate the detachment from the substrate, while the blue color is used for the force directed down, that would oppose the particle detachment. The gray color indicates the zone where the air pressure $p_A$ calculated via Eq. (3.17) is found negative, i.e., no bubble may physically exist or sustain. The black lines on the maps indicate isoforces with their magnitudes (in nN) displayed on the corresponding line.

The maps show that the contribution of a bubble to the particle detachment clearly depends on the substrate contact angle $\theta_s$ and the position of the contact line on the substrate $r_s$. The force acting on a particle $F_p$ is directed upward for hydrophilic substrates with contact angles up to $\theta_s \sim 55°$ regardless of $r_s$. For $55° \lesssim \theta_s \lesssim 85°$, the positive or negative contribution of $F_p$

depends on $r_s$, in other words in the size of the bubble. For hydrophobic substrates with contact angles greater or equal to $\theta_s \gtrsim 85°$, the force acting on a particle $F_p$ is directed down for any $r_s$.
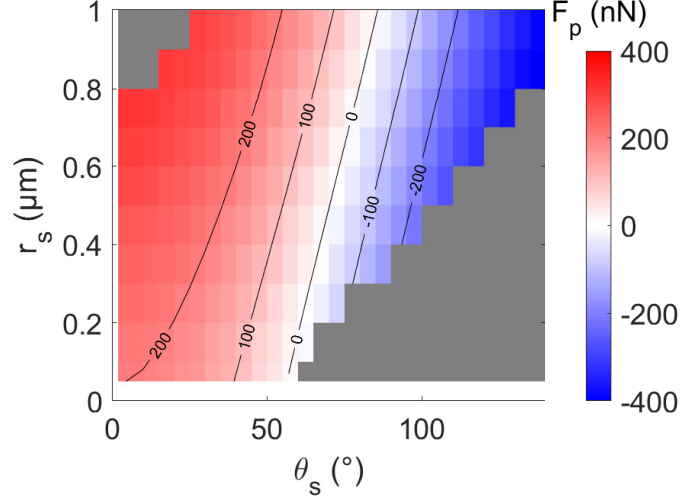


Figure 3.5: Map of the force $F_p$ applied by the bubble on the particle. Red color indicates an upward directed force, i.e., facilitating the particle detachment from the substrate, while blue color represents the force directed downward. The gray color indicates the zone where the pressure in the bubble is found negative and has no physical reality. The particle is hydrophobic with $\theta_p = 125°$.

### 3.2.2  Hydrophilic particle $(\theta_p = 50°)$

Fig. 3.6 illustrates the shape of the air-liquid interface in three different cases of wetting degree of the substrate characterized by contact angles $\theta_s = 100°$ (blue line), $\theta_s = 50°$ (pink line) and $\theta_s = 10°$ (black line). In these examples, the position of the contact line on the substrate is again fixed at $r_s = 0.5\,\mu m$. Similar to the case of hydrophobic particle, the bubble volume decreases with the increase of $\theta_s$, and this is translated into a decrease in pressure difference, $\Delta p$ ($\Delta p \approx -11 \times 10^5\,Pa$ for hydrophilic and $\Delta p \approx -7 \times 10^5\,Pa$ for hydrophobic substrates).

Here, are again varied the substrate contact angle $\theta_s$ (from hydrophilic $\theta_s = 2°$ to hydrophobic $\theta_s = 140°$) and the position of the contact line on the substrate, $r_s$ (from $r_s = 0.05\,\mu m$ to $r_s = 1\,\mu m$). Fig. 3.7 shows the $F_p$ map as a function of $\theta_s$ and $r_s$. The color code is identical to that of Fig. 3.5.

One can see that $F_p$ is almost always directed upward except for a tiny region located on the bottom right corner of the graph where $\theta_s$ has a large value ($\theta_s \gtrsim 135°$) while $r_s$ is small ($r_s \lesssim 0.4\,\mu m$). This means that the presence of a trapped bubble underneath a hydrophilic particle will almost always have a positive effect on the particle detachment except for strong hydrophobic substrates combined with small bubble volumes.
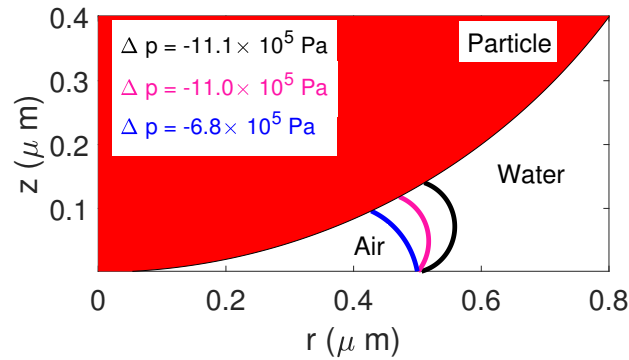
Figure 3.6: Shape of the air-liquid interface between a hydrophobic particle ($\theta_p = 50°$) and a hydrophobic substrate with $\theta_s = 100°$ (blue line), a hydrophilic substrate with $\theta_s = 50°$ (pink line) or $\theta_s = 10°$ (black line). For all these interfaces, $r_s = 0.5\,\mu m$.
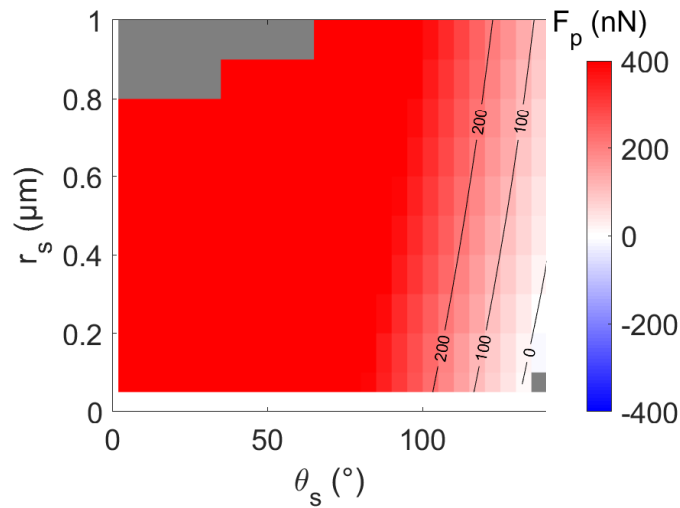


Figure 3.7: Map of the force $F_p$ applied by the bubble on the particle. The color code is identical to that of Fig. 3.5. The particle is hydrophilic with $\theta_p = 50°$.

## 3.3 Experiments

### 3.3.1 Materials and Methods

Two different types of beads were used in our experiments: hydrophilic silver coated silica microspheres (Cospheric) having a diameter of $2\,\mu m$ and hydrophobic polydisperse clear polyethylene microspheres (Cospheric) with a particle diameter ranging from 1 to $4\,\mu m$. When performing our experiments with latter particles, we selected those of diameter of about $2\,\mu m$. The particle

contact angle was measured using the method of placing a droplet on a lawn of particles [56].
Briefly, we passed 1.5 mL of particle suspension through the filter (cellulose esters 0.025 µm) to
form a dense lawn of particles. Then, a water droplet was placed on this lawn and the contact
angle measured using an optical tensiometer (Biolin Theta Lite) in "sessile drop" mode (to
measure static contact angle) and "dynamic contact angle" mode (to measure advancing and
receding contact angles). The same optical tensiometer was used to measure the substrate contact
angle. The results are presented in Table 3.1. Two types of substrate were used in the present
work: hydrophilic piranha treated glass and hydrophobic PFTS coated glass. For hydrophilic
materials, measurements of advancing/receding angles were not possible due to instantaneous
spreading of the droplet over the substrate/lawn. In the table, an important hysteresis can be
seen for polyethylene particles. This probably arises from the pillar-like structure of the particle
lawn, which promotes hydrophobicity while surface asperities pin the contact line and enhance
the hysteresis.

|   | Materials | static c.a. | advancing c.a. | receding c.a. |
|---|---|---|---|---|
| $\theta_s$ | Piranha treated glass | $2°$ [1] | – | – |
|   | PFTS coated glass | $100° \pm 4°$ | $117°$ | $89°$ |
| $\theta_p$ | Silver-coated silica | $10° \pm 4°$ | – | – |
|   | Polyethylene | $125° \pm 5°$ | $162°$ | $83°$ |

Table 3.1: Advancing, receding and static contact angles (c.a.) for substrates (two top lines) and
the particles (two lines) used in the experiments.

In order to place and immerse the particles on substrates of different wettability, we adopted
the following procedure. First, a suspension of microbeads was prepared by dispersing $35 \pm 5$ µg
of dry particles into 500 µL of DI water. For hydrophobic particles, 30 µL of ethanol was added to
the solution to enable the suspension and avoid any particle floating at the liquid-air interface.
Next, a droplet of 2 µL of the solution containing the microspheres was placed onto either a
hydrophilic piranha-treated or hydrophobic PFTS-coated glass coverslip. The coverslip was then
placed in an oven set to $40 °C$ for 1 hour (typically, the complete evaporation of 2 µL water droplet
occurs after 15-20 minutes). After the removal of the coverslip from the oven and its cooling to
room temperature a Hanks' Balanced Salt Solution (HBSS) is gently poured over until the liquid
height is about 3 mm and particles fully immersed. Finally, the coverslip is placed in a vacuum
chamber (Nalgene, volume 4.7 L; vacuum pump Laboport N 86 KN.18) for 10, 20 or 40 minutes
(this step is skipped for experiments without degassing). After this degassing step, the coverslip
was gently brought back to atmospheric pressure prior to its placing on the patch-clamp set-up
to measure the particle removal force.

The detachment force is measured using the patch-clamp technique presented in Chapter 2.
To create the detachment curve, at least 30 particles were removed from their substrates for no
degassing or 20 minutes of degassing cases and at least 10 particles were removed for degassing
during 10 or 40 minutes. The data that will be presented thereafter are averages of these runs.

### 3.3.2 Results

Fig. 3.8 presents the results for experiments carried out on hydrophobic particles placed onto
PFTS-coated hydrophobic (left) and piranha-treated hydrophilic (right) substrate. The graphs

---

[1]As we were using optical tensiometer, the accuracy of the contact angle measurements is low for small contact
angles. The value of $2°$ is the median value in our measurements.

show the percentage of particles ($y$-axis) that we have been able to detach[2] with a given applied force ($x$-axis). Circles correspond to the results obtained in the experiments without degassing; triangles, diamond and square corresponds to degassing for 10, 20 or 40 minutes, respectively. In our experiments, the maximum degassing time was set to 40 minutes since according to the manufacturer, the maximum level of vacuum enabled by pump (about $100\,\mathrm{mbar}$) was reached after about 10 minutes for our vacuum chamber of $4.7\,\mathrm{L}$. Fig. 3.9 shows similar data than previously but for hydrophilic particles.

A nonlinear least square fit is carried out for the experimental data of Fig. 3.8 and 3.9. The fit uses the logistic function

$$y_{fit}(x) = \frac{100 \cdot \left(e^{bx} - 1\right)}{e^{bx} - c},\tag{3.18}$$

where $b > 0$ and $c$ are fitting parameters, $x$ is the applied force (in nN), $y_{fit}$ is the percentage of removed particles at a corresponding applied force $x$. An associated mean detachment force, i.e., a force required to remove 50% of the particles, is worked out from the fitting curve and presented in Table 3.2. In this chapter, we mainly use the mean detachment force values. However, our experimental curves provide additional information about data scattering. You can find the details in Appendix II.
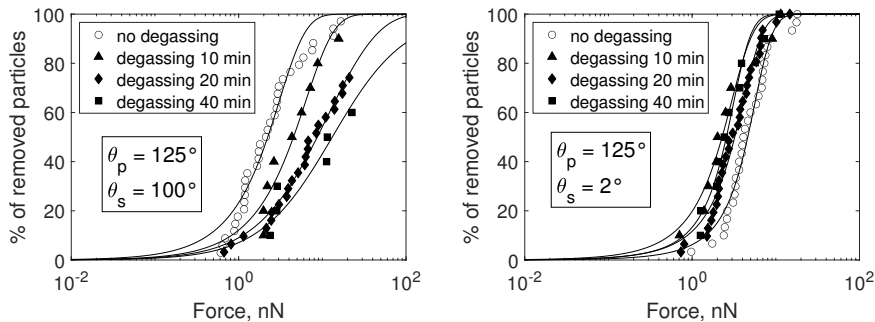


Figure 3.8: Experimental curves obtained for hydrophobic particles placed onto hydrophobic (left) and hydrophilic (right) substrates.

From Fig. 3.8, several observations are made. First, the results show that prior to degasification, the value of the detachment force, $F_d$, is larger on hydrophilic than on hydrophobic substrate (cf. Table 3.2 for detailed value at 50%). This is probably due to the size of the bubble that can be trapped with respect to the wetting properties of the surfaces when immersing the system. Second, while the value of $F_d$ decreases with degasification on hydrophilic substrate, it increases on hydrophobic substrate. This change in $F_d$ value with degasification indirectly demonstrates the presence of bubbles underneath the particles in these systems. Third, the amount of degassing time, $\Delta\tau$, seems non-equivalently affect these two systems. In the case of hydrophilic substrate, $F_d$ remains more or less constant around an average value of $F_d \sim 2.7\,\mathrm{nN}$ regardless $\Delta\tau$ as long as a first degasification has taken place. In the case of hydrophobic substrate, there is a steady increase in $F_d$ from $2.23\,\mathrm{nN}$ to $13.16\,\mathrm{nN}$ with $\Delta\tau$. In other words, for the identical hydrophobic particles, the bubble facilitates or restrains the removal of particles upon the hydrophobic or hydrophilic nature of substrate, respectively.

Experimental data obtained with a hydrophilic particles are shown in Fig. 3.9. Similar to pre-

---

[2]It is to note that in Chapter 2, we had along $y$-axis the percentage of particles that we have NOT been able to detach (percentage of attached particles).
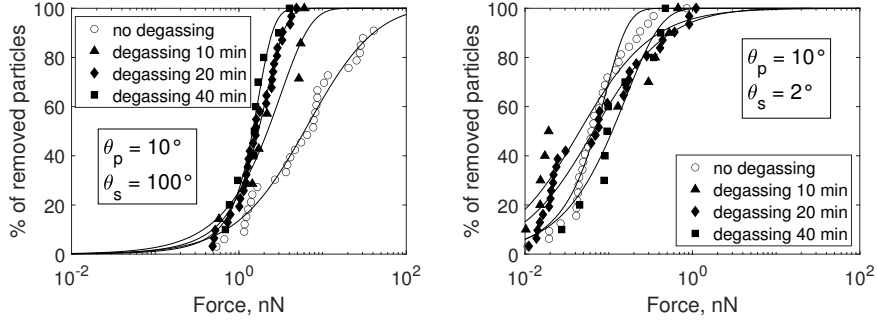
Figure 3.9: Experimental curves obtained for hydrophilic particles placed onto hydrophobic (left) and hydrophilic (right) substrates.

| | Case | 0 min | 10 min | 20 min | 40 min |
|---|---|---|---|---|---|
| hydrophobic particle $\theta_p = 125°$ | hydrophobic substrate $\theta_s = 100°$ | 2.23 nN | 4.52 nN | 8.70 nN | 13.16 nN |
| | hydrophilic substrate $\theta_s = 2°$ | 4.62 nN | 2.28 nN | 3.23 nN | 2.57 nN |
| hydrophilic particle $\theta_p = 10°$ | hydrophobic substrate $\theta_s = 100°$ | 6.05 nN | 2.20 nN | 1.71 nN | 1.46 nN |
| | hydrophilic substrate $\theta_s = 2°$ | 0.07 nN | 0.05 nN | 0.07 nN | 0.11 nN |

Table 3.2: Mean detachment forces obtained from fitting curves (Eq.(3.18)) and corresponding to experiments without or with degassing for 10, 20 or 40 minutes. Data for various combinations of hydrophobic ($\theta_p = 125°$) and hydrophilic ($\theta_p = 10°$) particles with respect to substrate wetting characteristics (PFTS coated, $\theta_s = 100°$ and pirahna cleaned, $\theta_s = 2°$).

vious paragraph, we hereafter cite remarkable observations. First, on hydrophobic substrate, the order of magnitude of 50% detachment force is about 1 nN which is similar to experiments carried out with hydrophobic particles at least for low degassing levels. Second, experiments carried out with both surfaces - particles and substrate - hydrophilic, show a 50% detachment force of the order of $1 \times 10^{-2}$ nN (cf. Table 3.2). This is a much lower value in $F_d$ compared to any other combination of wettability for the involved particle/substrate surfaces that yielded until now a $F_d$ of the order of 1 nN. It has to be noted that the measurement of forces of the order of $1 \times 10^{-2}$ nN was at the limit of the patch-clamp technique and could create reduced accuracy. Third, the degasification seems to have minor or no effect on $F_d$ in the experiments carried out on hydrophilic substrate. Indeed, the detachment force variations given in Table 3.2 can be presumed constant considering the data scatter at the limit of the patch-clamp technique (Fig. 3.9(right)). The absence of effect from the degasification combined with low value of $F_d$ for hydrophilic surfaces, may suggest the absence of trapped bubble. Fourth, in the case of hydrophobic substrate, $F_d$ remains more or less constant around a value of $F_d \sim 2$ nN regardless $\Delta\tau$ as long as a first degasification has taken place.

When looking at all experimental results (Table 3.2), it appears that the order of magnitude of the detachment force is set higher as long as one of the involved surfaces is hydrophobic. The degasification can have initial effect but shortly becomes insenstive to increasing $\Delta\tau$ if one of the surfaces has opposite hydrophobicity. Finally, the effect of degasification, hence a change in bubble volume, is particularly striking when both surfaces are hydrophobic.

The experiments through the difference in the measured detachment force strongly suggest the existence of a bubble when at least one of the surfaces, i.e., the particle or the substrate, is showing a hydrophobic characteristics - the extremely low values of this force for exclusively hydrophilic surfaces may indicate the absence of bubble although that assertion could not be verified experimentally with our equipments. Without considering the presence of a trapped bubble, a physical explanation of the variation in this force with the degassing would be hard and puzzling. Indeed, the degassing promotes at least the shrinking of the bubble size or at best its vanishing. One would then expect a change in the detachment force as observed in the experiments if a bubble is trapped under a microparticle. The variation of this force with the degasification is the signature of the presence of a trapped bubble. However, the scenario of bubble shrinking or vanishing can be complex from the fact that the system is put in a vacuum for degasification and had to be brought back to the atmospheric pressure for measuring the detachment force in the patch-clamp setup. The effects of these experimental steps on the measured force will be discussed in the next section.

## 3.4 Discussion

Looking at the experimental $F_d$ values for a hydrophobic particle on hydrophobic substrate in table 3.2, a good agreement with the computations can be observed. Indeed, for $\theta_p = 125°$ and $\theta_s = 100°$ the computations show that the presence of the bubble brings an extra force to retain further the particle on the substrate regardless the size of the bubble, i.e., the value of $r_s$. More interestingly, by decreasing $r_s$, i.e., by decreasing the size of the bubble, the value of $F_d$ increases. This is in full agreement with the experimental observations where the shrinking bubble size with degasification comes with an increase in $F_d$. However, the agreement remains good on the overall behaviour but limited on the value of $F_d$ which is found of the order of $100\,\mathrm{nN}$ for the computations whereas it is about $10\,\mathrm{nN}$ for the experiment. Indeed, care should be taken when comparing these results: the computations only take into account forces arising solely from the presence of the bubble whereas the measured forces in the experiment reflect also the particle-substrate interactions. Therefore, the difference found in $F_d$ values in the experiments compared to computations is not contradictory to the model. However, for the computed case ($\theta_p = 125°; \theta_s = 100°$) where the force due to the bubble appears to be relatively large ($F_p \sim \mathcal{O}(100\,\mathrm{nN})$), one would have expected the latter to overshadow the force arising from the substrate-particle interactions. This does not seem to occur with respect to measured experimental values of $F_d \sim \mathcal{O}(1 - 10\,\mathrm{nN})$.

For the computational case of ($\theta_p = 125°; \theta_s = 2°$) the differences even cumulate where a shrinking bubble give a decrease in $F_p$ in the experiments while it increases in the computations. The possible roots of these differences will be discussed later in the section.

Regarding the other numerical computations with a hydrophilic particle ($\theta_p = 50°$), the results properly emulate the experimental observations where the bubble facilitates the detachment regardless of substrate's contact angle. At small $\theta_s$ the positive contribution of this extra force reaches its highest values and this also corresponds to the lowest values of $F_d$ measured experimentally. For larger $\theta_s$ values above approximately $90°$, i.e., when the substrate becomes hydrophobic, the computations show a bubble size dependency. In this case the positive contribution of bubble

force $F_p$ decreases and may even become nul with decreasing $r_s$. However, this is not translated in the experiments with an increase but with an decrease in $F_d$ for $\theta_p = 10°, \theta_s = 100°$.

As mentioned, the numerical computations show only a partial agreement with the experimental results and we may now describe their possible causes. First, the numerical computations consider a symmetrically placed bubble under the particle. This, of course, is rarely achievable in a real system and could be part of the source of the differences. Second, the computations consider ideal smooth surfaces whereas such system does not exist in reality. As a consequence, the local contact angle for either $\theta_p$ or $\theta_s$ may not correspond to static contact angles that we assumed numerically. This will also bring asymmetry of the contact angle along the contact line between the bubble and either the particle and/or the substrate. Third, the effect of non ideality of the surfaces on the bubble may well be amplified through the degasification steps during the experiments that we will now describe.

Initially, the air bubble, in the state "0", can be characterized by its pressure $p_{A0}$, volume $V_{A0}$, the position of its contact line on the substrate $r_{s0}$, and the contact angles with the particle $\theta_{p0}$ and the substrate $\theta_{s0}$. With the degasification, one expects the bubble to loose some of its substance or, in the least favorable case, keep its initial characteristics. Within the ideal gas approximation, this translates to

$$p_{A0}V_{A0} \geq p_{A1}V_{A1}, \tag{3.19}$$

with the subscript "1" designing the final state after the degasification. In the following paragraphs, we will describe two distinct transformations that the bubble may undergo during the degasification. The first will consist of a modification in the surface contact angles whereas the second a change in bubble's volume. Note that in the real system, a complex combination of these two events may occur simultaneously but will not be addressed here.

If the positions of the contact lines on the substrate and the particle are locked up, i.e., contact lines are pinned, any change in pressure will automatically induce a shape modification, and consequently, a change in $\theta_p$ and $\theta_s$ values. Of course, in the assumption of an axisymmetric placement of the bubble throughout this study, any change in $\theta_p$ and $\theta_s$ will also modify the volume.

In the case of a decrease in bubble volume while the wetting properties are conserved, i.e., $\theta_{p1} = \theta_{p0}$ and $\theta_{s1} = \theta_{s0}$, the behavior of the detachment force in this situation would essentially depend on the final position of the contact line on the substrate, $r_{s1}$. The system behavior can be figured out from the numerical model by referring, for instance, to low values of $r_s$ in Fig. 3.5 for the case of a hydrophobic particle. As it can be seen on the figure for values of $\theta_s$ larger than approximately $55°$, a decrease in $r_s$ would imply a smaller or even a negative $F_p$ which means one has to apply a larger force $F_d$ to detach the particle from the substrate. This is in agreement with the experiments where in Table 3.2 one can observe that the degasification of the system having both surfaces hydrophobic (particle and substrate) yields a larger detachment force.

Although the agreement with experiments appears to support the above physical explanation, it has to be reminded the possible coexistence of an alternative scenario where the contact angles can also vary due to the hysteresis. Indeed, prior to patch-clamp experiments run under atmospheric pressure, the degasification step induces a temporary enlargement of the bubble. This brings a complication on the final bubble state where either, or both, contact lines $(\theta_p, \theta_s)$ may remain pinned on their positions acquired during the degasification. As a consequence, one would expect in the final state either a larger $r_s$ value and/or a larger contact angle on one or both surfaces.

In order to find the configuration that could match our experimental observations (table 3.2), we carried out numerical computations. The effect of degasification on the detachment force through a modification of the contact angles and/or on the substrate position $r_s$ was investigated.
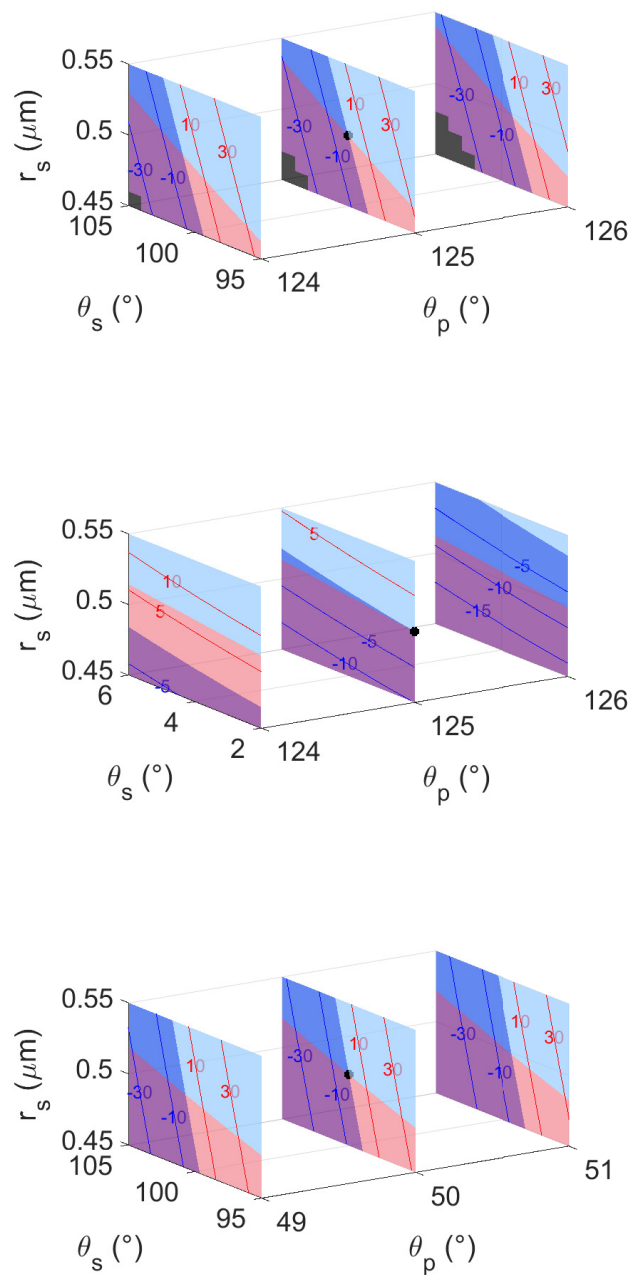
Figure 3.10: Map of bubble states for different initial states: $(\theta_{s0} = 100°, \theta_{p0} = 125°, r_{s0} = 0.5\,\mu\text{m})$ (top); $(\theta_{s0} = 2°, \theta_{p0} = 125°, r_{s0} = 0.5\,\mu\text{m})$ (center); $(\theta_{s0} = 100°, \theta_{p0} = 50°, r_{s0} = 0.5\,\mu\text{m})$ (bottom). The isolines indicate the bubble-induced force that retains (negative values) or repulses (positive values) the particle from the substrate. The black point represents the initial state.

This was done by varying the control parameters ($\theta_p$, $\theta_s$ and $r_s$) around their mean values and for different surface hydrophobicity. For these computations, the substrate position was set to $r_s = 0.5$ while the values of $\theta_p$ and $\theta_s$ used those of measured values of table 3.1 except for $\theta_p = 10°$. Indeed, as mentioned before, due to numerical limitations, for low values of the particle contact angle, we set the latter to $\theta_p = 50°$. Even though this numerical value is higher, it still represents a hydrophilic characteristic of the particle and can enlighten us about the main behavior of the system. Fig. 3.10(a-c) shows three different maps corresponding to various combinations of particle/substrate wetting properties that were tested in the experiments (cf. Table 3.1). The initial state is highlighted by a central black star around which the three parameters are varied. Four regions are highlighted in different colors corresponding to following conditions: (i) $F_{d1} > F_{d0}$ and Eq.(3.19) not valid (light blue); (ii) $F_{d1} \leq F_{d0}$ and Eq.(3.19) not valid (dark blue); (iii) $F_{d1} > F_{d0}$ and Eq.(3.19) valid (pink); (iv) and finally $F_{d1} \leq F_{d0}$ and Eq.(3.19) valid (purple). In the maps, the isolines show the additional force that the system will need in order to detach the particle from the substrate. To avoid any confusion, we may remind that a negative isoline value will mean that the system needs a greater detachment force to remove the particle. The area with no physical solution (i.e., $p_A < 0$) is grey colored.

Fig. 3.10(a) represents the map of a hydrophobic particle ($\theta_p = 125°$) over a hydrophobic substrate ($\theta_s = 100°$). According to the experimental results (table 3.2), the mean force increases with degasification for this set combination of ($\theta_p = 125°; \theta_s = 100°$). In this regard and with respect to the condition Eq. (3.19), only the pink should be considered where an increase in the detachment force corresponds to the area of negative isoline values. Although the maps do not provide a firm affirmation of the way the system behaves exactly, i.e., which of the three parameters contributes to the increase of the experimentally observed $F_d$, it at least indicates in which direction the system is probably heading. With the present map, it shows the region where the combined variations in $r_s$, $\theta_s$ or $\theta_p$ can satisfy and agree with the experimental observation. In this case, a decrease $r_s$ may only occur with an increase in $\theta_p$ and/or $\theta_s$.

Similarly, the maps in Fig. 3.10(b-c) show the results of particle and the substrate having opposite wettability. The associated experimental results ($\theta_p = 125°; \theta_s = 2°$), ($\theta_p = 10°; \theta_s = 100°$) showed a decrease (cf. table 3.2). In this case, the purple color highlights this trend where $F_{d1} \leq F_{d0}$ and the Eq. (3.19) remains valid.

It is worth noting that for all these maps, small variations in $\theta_s$, $\theta_p$ and/or $r_s$ lead to changes in $F_d$ of $\sim 1\,\text{nN}$, which corresponds to the order of magnitude observed in experiments (cf. Table 3.2).

## 3.5   Conclusion

We investigated the possible presence of an air bubble trapped between a particle and a substrate. A theoretical model based on energy considerations was advanced. The model provided insights of the situations that one may encounter when the particle is detached, i.e., bubble either sticking to the particle, to the substrate or both. Another theoretical model supplemented by its companion numerical computations gave access to values of bubble-induced forces with respect to various surface wetting characteristics. In particular, the results showed that the presence of a trapped bubble underneath a hydrophilic particle will almost always help the particle detachment except for strong hydrophobic substrates combined with small bubble volumes. For hydrophobic particles, the positive or negative contribution on particle detachment was found to depend both on the wetting characteristics of the substrate and the size of the bubble. In support to numerical observations, experiments were run with the primary objective of demonstrating the presence of the bubble. This was done thanks to the measurement of the detachment force with and without

a degasification step before the measurement. The observed variation of the measured force with the degasification demonstrated the presence of a trapped bubble. Comparison between computations and experiments showed a partial agreement on the overall behaviour but differed on the magnitude of the found detachment force. Several hypothesis were proposed to explain the differences. In particular, the latter were speculated to arise from the non ideality of the surfaces (roughness) and the non symmetric placement of the bubble at the immersion step of the particle.

The present study showed that a bubble can be trapped under a particle if at least one of the involved surfaces in the system, i.e., that of the particle or the substrate, is hydrophobic. However, this entrapment appears unlikely when all surfaces are hydrophilic. This result is of particular interest to, for instance, food industries where the contamination of surfaces of food processing lines by pathogens and spoilage bacteria is a major issue that has not yet found a proper cleaning and disinfection solution. Knowing that bacteria can present different degree of hydrophobicity [55], the surface treatment with a judicious coating with respect to the wetting properties of the potential pathogens, can greatly facilitate the bacterial removal. Engineering surface coating with respect to the type of bacteria would ease their detachment and prevent the further overuse of chemicals for equipment disinfection and, therefore, contribute to the implementation of greener industrial processes.

# Part II

# Collective dynamics of microspheres in evaporating droplets

# Chapter 4

# State of the art

The purpose of this chapter is to review previous research works on droplets with and without particles. We consider the entire life cycle of a droplet, from deposition to complete drying. In the first part of this chapter, we consider a droplet without particles and describe the flows developing within the droplet during evaporation. In the second part, we look at the differences in droplets containing particles. We will additionally address the question of suspension stability, the effect of particles on the evaporation process and on the flow inside a droplet. A large part is devoted to droplet leftovers observed after the liquid evaporation as well as the factors leading to the formation of various patterns.

## 4.1 Sessile droplet without particles

The theoretical description of a static or moving droplet on a substrate was given in Chapter 1. Therefore, in order to avoid redundancy, we advise the reader to refer to the section 1.4.1. Thereafter, we rather review the physics behind an evaporating droplet. It is to note that in this chapter we will restrict the description to partial wetting situations (i.e., hydrophilic and hydrophobic substrates).

### 4.1.1 Dynamics of evaporation

A droplet left on a substrate experiences evaporation, if the atmosphere around is not saturated with the liquid's vapor. The process of a sessile droplet evaporation was widely studied due to its numerous applications, such as cooling [149] or coating [85]. Previous studies [126, 185, 4, 106] show that typically droplets follow one of four evaporation modes illustrated in Fig. 4.1: (a) a constant radius mode, (b) a constant angle mode, (c) a mixed mode, or (d) a stick-slip mode.

The constant radius mode (Fig. 4.1 a) corresponds to a pinned contact line where the area between the droplet and substrate remains constant, while the contact angle decreases with time. This mode is often seen with sessile droplets on rough substrates, as the contact line tends to pin onto surface defects [38, 40]. This is the expected behavior for liquid-solid couples with a significant contact angle hysteresis [126].

When the droplet follows the constant angle mode (Fig. 4.1 b), the wetted contact area shrinks while the contact angle remains unchanged. This evaporation mode is typically observed when the droplet is placed on a smooth hydrophobic substrate. This is the expected behavior for an ideal
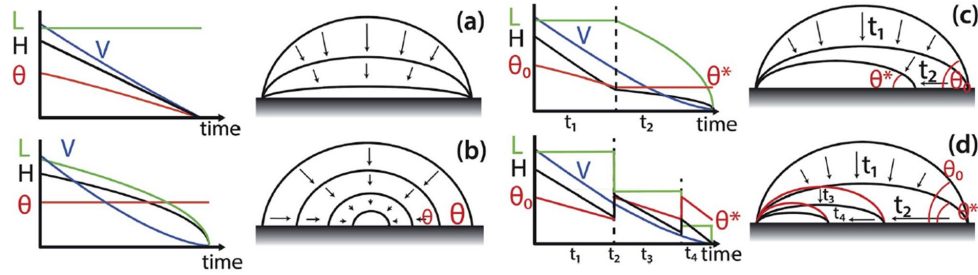
Figure 4.1: Evaporation modes: (a) Constant contact radius, i.e., a strong pinning of the contact line prevents the droplet radius shrinkage. (b) Constant contact angle, i.e., the droplet shrinks while the contact angle remains constant. (c) Mixed mode, i.e., the droplet alters between constant radius and contact angle modes. (d) Stick-slip mode, i.e., the droplet evaporates in contact radius mode, then it suddenly shrinks and continues in constant contact radius mode evaporation. Image taken from [185].

system with equilibrium between liquid, solid, and vapor, where there is no difference between advancing and receding contact angles [126].

The mixed evaporation mode (Fig. 4.1 c) supposes that both contact radius and contact angle decrease simultaneously. This behavior was reported in [185]. This evaporation mode can arise when there is only slight hysteresis.

The droplet in "stick-slip" mode (Fig. 4.1 d), alternates between two phases. During the "stick" phase, the droplet follows the constant radius evaporation mode. Then, the contact angle reaches its minimum value, and the contact line suddenly depins and slips into a new position ("slip" phase), leading to contact radius decrease. Then, the droplet is again in the constant radius mode ("stick" phase) until the next "slip" phase. This alteration of phases may occur several times until the evaporation is complete. The stick phase lasts generally longer than the slip phase and accounts for the majority of the droplet lifetime. The stick-slip behavior was reported when a droplet evaporates on pillared subsrate [172] or when particles are added to the droplet (see section 4.2.2).

### 4.1.2 Flows inside a droplet

As the droplet evaporates, a fluid flow develops within it. An outward capillary flow (sometimes also referred to as radial outward flow) and a Marangoni flow are competing to govern the overall flow structure.

#### Capillary flow

Fig. 4.2 a&b schematically presents the local evaporation flux for a droplet placed on a hydrophilic or hydrophobic substrates based on the work of Kadhim *et al.*[80]. The longer arrows illustrate higher evaporation rates. For a droplet placed on a hydrophilic substrate of identical temperature, the liquid molecule would rather escape from the droplet edge than from its center [43] (Fig. 4.2 c). Since the evaporation rate is higher at the droplet edge, the droplet will either shrink (Fig. 4.3 a), or the liquid will move from the droplet center to its edge (Fig. 4.3 b) if the contact line is pinned. This liquid flow towards the pinned droplet edge is known as the outward capillary flow [42]. Although, the local temperature at the droplet surface can change during evaporation, and potentially affect the evaporation rate, temperature gradients due to evaporation
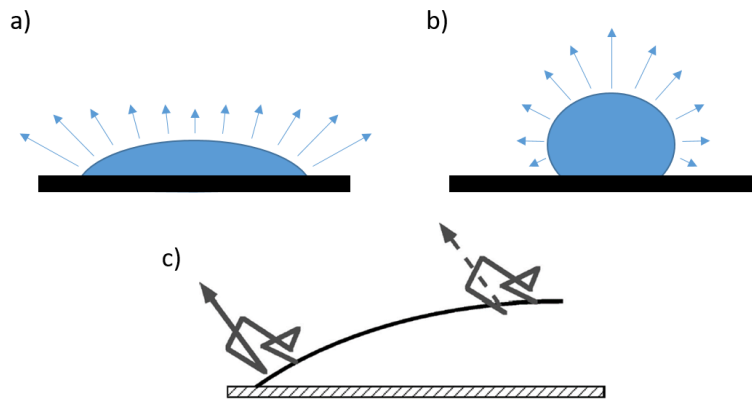
Figure 4.2: Evaporation rate for a droplet placed on (a) hydrophilic and (b) hydrophobic substrates. (c) The probability of escape of a molecule depending on its starting point on droplet placed on hydrophilic substrate (image taken from [43]).

do not seem to play an essential role for water-based droplets placed on a very hydrophilic substrate [43]. For a droplet placed on a hydrophobic substrate, the highest evaporation rate is observed in the droplet center (Fig. 4.2 b), and no capillary flow will develop inside the droplet. The temperature gradients, on the other hand, will be more significant in this case, and Marangoni flow will appear.
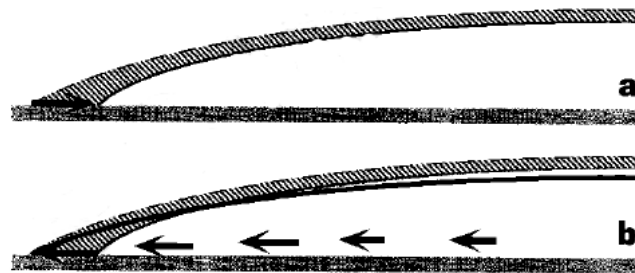


Figure 4.3: (a) Side view of droplet evaporation without capillary flow: droplet shrinks. (b) Evaporation with compensating capillary flow: pinning of the contact line and decrease of the contact angle. Image taken from [42].

**Marangoni flow**

The Marangoni flow appears due the surface tension gradient on the droplet surface [100, 70]. The surface tension gradient can be induced by the nonuniform distribution of temperature [70, 69, 128, 121, 85], surfactant-concentration gradients [69, 121, 150, 85] or the solutal gradients [81, 85, 102]. Since high-surface-tension regions of a droplet pull stronger on the surrounding liquid than low-surface-tension regions, this causes the liquid flow away from the low-surface-tension region. In the absence of a surface tension gradient, e.g., in a drop of pure water with no temperature differences, Marangoni convection is not observed [146, 69].

The rate of transport due to Marangoni flow is described by a non-dimensional Marangoni

number, which is the ratio of the advective transport rate due to surface tension gradient to the diffusive transport rate. Depending on the nature of the Marangoni flow, two Marangoni numbers, solutal $\text{Ma}_\text{S}$ and thermal $\text{Ma}_\text{T}$ are used. The solutal Marangoni number $\text{Ma}_\text{S}$ is expressed as:

$$\text{Ma}_\text{S} = \frac{-\frac{\partial \gamma}{\partial C} L}{\mu_l D} \Delta C \tag{4.1}$$

where $\frac{\partial \gamma}{\partial C}$ is the change in surface tension with the solute concentration $C$, $L$ is the characteristic length (e.g., droplet radius $R_c$), $\Delta C$ is the maximum concentration difference between two points of the droplet, $\mu_l$ is the dynamic viscosity, $D$ is the liquid diffusion coefficient.

In this chapter, we mainly consider pure droplets or pure droplets with the addition of insoluble particles. We will, therefore, not discuss the solutal Marangoni flow further. The thermal Marangoni flow appears in droplets due to the temperature gradient along the droplet's surface because of the variation in the evaporation rate along the droplet's surface (Fig. 4.2 a&b). This temperature gradient induces a surface tension gradient on the droplet surface and generates the Marangoni flow. The thermal Marangoni number $\text{Ma}_\text{T}$ reads:

$$\text{Ma}_\text{T} = \frac{-\frac{\partial \gamma}{\partial T} L}{\mu_l \alpha_T} \Delta T \tag{4.2}$$

where $\frac{\partial \gamma}{\partial T}$ is the change in surface tension with temperature $T$, $\Delta T$ is the maximum temperature difference between two points of the droplet, and $\alpha_T$ is the liquid thermal diffusivity.

When the thermal Marangoni number $\text{Ma}_\text{T}$ is small, i.e., the thermal diffusion dominates, there is no Marangoni flow. For $|\text{Ma}_\text{T}|$ larger than 80, Marangoni-associated convection plays a major role in droplet's internal flows [124, 36]. The direction of the Marangoni convection cell depends on the direction of the surface tension gradient, i.e., on the sign of $\text{Ma}_\text{T}$. However, the Marangoni number is not very useful in practice, as the surface tension gradient is difficult to measure. Ristenpart *et al.*[138] have shown theoretically and supported their findings experimentally that the direction of Marangoni flows depends on (i) the contact angle and (ii) the ratio of the thermal conductivities of the substrate and the liquid. For a given ratio of the thermal conductivities, one can find the critical contact angle at which $\text{Ma}_\text{T} = 0$ (i.e., the direction of the Marangoni convection cell is different below and above this angle). In reality, however, when the droplet height reduces, the Marangoni circulation vanishes for the angle below a critical value [162]. This is expected since for thin droplets the temperature difference along a vertical direction can be neglected, therefore, no convection cell can be created.

**Coexistence of capillary and Marangoni flows**

As mentioned previously, the "total" flow inside a droplet is a result of competition between capillary and Marangoni flows. If the Marangoni number is small $|\text{Ma}_\text{T}| < 80$, there is no significant Marangoni convection, and the droplet internal flow is only dictated by the capillary flow (Fig. 4.4 a). If the Marangoni number is large enough $|\text{Ma}_\text{T}| > 80$, the presence of Marangoni convection changes the flow within the droplet from radially outward to circular (outward or inward) movement [70]. This circular movement either coexist with the capillary flow [118, 121] (Fig. 4.4 b), or suppress it [186] (Fig. 4.4 c) depending on the Marangoni convection cell direction. If capillary and outward flows coexist, a stagnation point (green triangle in Fig. 4.4 b) should appear at the air-liquid interface, below which there is a capillary flow [118]. If the Marangoni number is close to critical, an interplay of capillary and Marangoni flows occurs resulting in contact line instability [37].
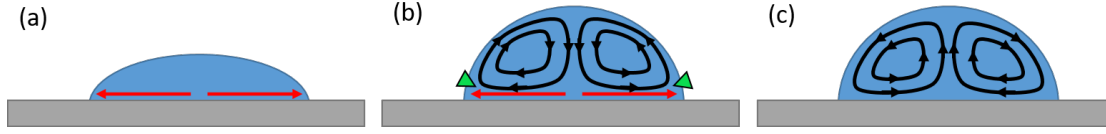
Figure 4.4: Scheme of coexistence of Marangoni (black arrow) and capillary (red arrow) flows: (a) total flow is dominated by outward capillary flow, (b) capillary and Marangoni flows are outward along liquid-substrate interface, (c) Marangoni flow is inward along liquid-substrate interface, the capillary flow is suppressed by Marangoni convection cell.

## 4.2 Sessile droplet with particles

In the current study, we are particularly interested in droplets containing particles at a concentration of less than 5% w/v. This research topic has been widely studied since the pioneering work of Deegan *et al.*[42] and due to its potential numerous applications. For instance, in medicine, drops of blood (that actually contain particles) can be employed for medical diagnostics to determine several types of cancer [132, 180], myeloma and other pathologies of the lymphoid origin [84], and anaemia [20]. In the industry, the study of droplets containing particles is important for inkjet printing [153, 83], coating [85], fabrication of microarrays [50, 91] or for spectroscopy [6]. The use of nanofluid (i.e., fluid with nanoparticles) is also an efficient way to increase critical heat flux [112].

### 4.2.1 Suspension stability and zeta-potential

When one works with a particle suspension, the main issue is the stability of the homogeneous suspension. There are two key threats to stability: (i) sedimentation or floating of particles depending on their density, and (ii) formation of aggregates. It will be shown below that these issues are related.

In the current work, we deal with particles with a density slightly higher than that of the surrounding liquid, and we essentially consider the sedimentation mechanism. The sedimentation time $\tau$ of a particle in an aqueous suspension reads [8]:

$$\tau = \frac{9h_t\mu_l}{2R^2(\rho_p - \rho_l)g} \tag{4.3}$$

where $h_t$ is the height of the tube containing the suspension, $\mu_l$ is the dynamic viscosity of the liquid, $R$ is the radius of the particles, $\rho_p$ is the density of the particles, $\rho_l$ is the liquid density, and $g$ is the gravitational acceleration.

The particle aggregation occurs due to the electric charge at the surface of the particles, that prevents them from dispersing in a liquid [96]. According to Eq.(4.3), aggregates sediment faster, as do larger particles of same properties. Therefore, not only aggregates reduce the homogeneity of the suspension but they also promote sedimentation. The modification of the particle surface charge allows, therefore, to avoid aggregation and hence slow down particle sedimentation.

The interactions of charged particles between themselves as well as with the surrounding medium are described by the theory of suspension stability.

**Theory of suspension stability**

The theory of suspension stability was developed in 1940s by two independent groups of scientists – Derjaguin & Landau[1] [47] and Verwey & Overbeek [169]. The Derjaguin-Landau-Verwey-Overbeek (DLVO) theory describes the interactions between particles in a suspension by attractive van der Waals forces and repulsive electrostatic forces of *double layer* assuming that these forces are independent.

The origin of the van der Waals forces was described in Chapter 1, and we kindly ask the reader to refer to the section 1.1. The **double layer** is formed by ions around a particle (Fig. 4.5) in order to neutralize the charge at the surface of the particle. The first (Stern) layer consists of ions adsorbed onto the particle due to chemical interactions. It is firmly anchored to the surface of the particle. The second (diffuse) layer is composed of ions attracted to the surface charge via the Coulomb force, electrically screening the first layer. The ions of the diffusive layer are loosely connected to the particle and some of them can eventually move out under the influence of the surrounding medium. The slipping plane separates the ions attached to the particle surface from the mobile fluid, and the net electrical charge contained within the region bounded by the slipping plane is the so-called **zeta poterntial**. As two particles approach one another, their double layers overlap, causing repulsion, which would be proportional to the square of the zeta potential.
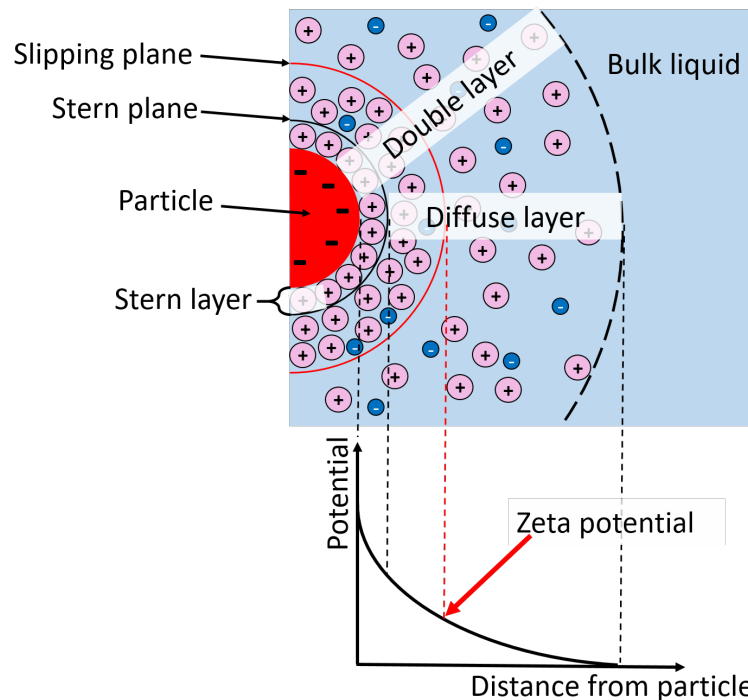


Figure 4.5: Diagram showing the ionic concentration and potential difference as a function of distance from the charged surface of a particle suspended in a dispersion medium.

The dependence of the free energy (which is the sum of the attractive van der Waals and repulsive electrostatic interaction energy) on the distance between particles is given in Fig. 4.6 for high (blue line) and low (red dashed line) absolute values of zeta potential. Some outcomes

---

[1]original work was published in Russian in 1941

can be drawn from this figure. First, when two particles approach one another, a high zeta potential will confer stability, while for a low zeta potential attractive forces may exceed repulsion. Second, as zeta potential increases, the energy barrier to outcome for aggregation (which occurs at the primary minimum, see Fig. 4.6) also increases. Third, for low zeta potential, a secondary minimum could be created, where a weak and potentially reversible adhesion between particles exists. Consequently, suspensions with high zeta potential (negative or positive) are electrically stabilized, while suspensions with low zeta potentials tend to coagulate or flocculate, as outlined in Table 4.1 [65].
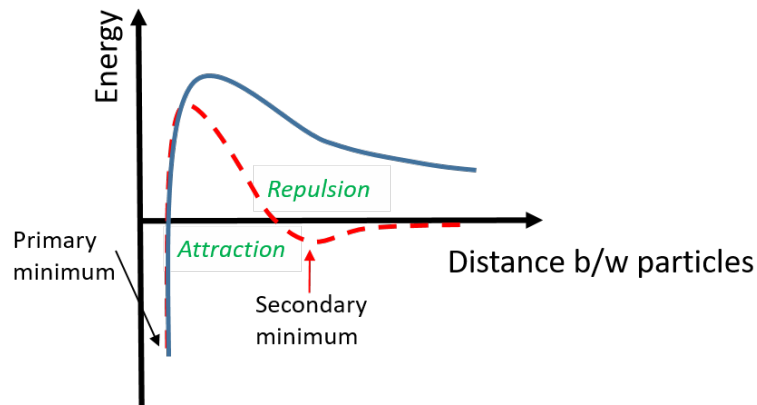


Figure 4.6: Schematic diagram of the variation of free energy with the distance between particles according to DVLO theory at a high zeta potential (blue line) and at a reduced zeta potential (red dashed line).

| Zeta potential (mV) | Stability behavior |
|---|---|
| 0 to ±5 | Flocculation or coagulation |
| ±10 to ±30 | Incipient instability |
| ±30 to ±40 | Moderate stability |
| ±40 to ±60 | Good stability |
| Greater than ±60 | Excellent stability |

Table 4.1: Stability behavior of suspension based on zeta potential value [86].

**Methods of suspension stabilization**

There are three effective methods used to attain stability of solid suspensions [51]: (i) control of pH value; (ii) addition of surface activators or surfactants; (iii) use of ultrasonic vibration. All of them aim to modify surface properties. Usually, zeta-potential is positive at low pH and negative at high pH [67], so zeta-potential goes to more positive values with decreasing pH level [11]. The addition of surfactant can both increase and decrease zeta-potential, so the right concentration should be chosen [145]. The ultrasonication is most often used to homogenize suspensions. It can break the agglomeration and disperse particles in suspensions [182]. The sonication time should as well be optimized [97], and the optimal duration usually varies from 3 h to 60 h depending on particle size and material.

### 4.2.2   Droplet evaporation in the presence of particles

A droplet containing particles would obey one of the five following evaporation modes. Four of them are the same as those described in the section 4.1.1 for a pure droplet and schematically presented in Fig. 4.1, and a fifth one was found by Askounis *et al.* [4]. The authors revealed that graphene platelets in ethanol exhibited unique evaporation behavior (Fig. 4.7) resembling a "stick-slip" phenomena (Fig. 4.1 d). In brief, initially, a droplet evaporates following the constant angle mode. As the liquid evaporates, particle concentration at the contact line increases, resulting in a growth of local viscosity [109]. At some point, perhaps due to enhanced viscosity, the contact line pins to one side while the other side squeezes to an energetically more favorable position [4]. The contact angle jumps to a value that is higher than the initial one similar to the stick-slip mode. However, the contact line slowly drifts during the whole evaporation process (Fig. 4.7) instead of having "stick" and "slip" phases.
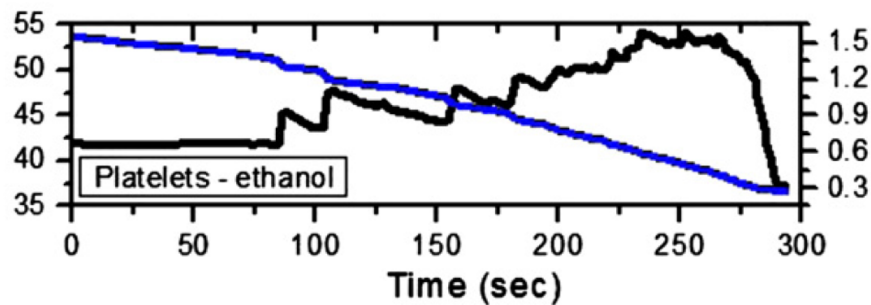


Figure 4.7: Evolution of contact angle (black) and contact radius (blue) with time for 0.1% w/v platelets in ethanol on PTFE. Image taken from [4].

The addition of particles to a pure droplet can affect the evaporation mode (e.g., increase the pinning time in constant radius or stick-slip modes) or even change the evaporation mode (e.g., the same ethanol droplet followed a constant angle evaporation mode without particles but a stick-slip mode with particles [109]).

When a droplet follows the constant radius evaporation mode, the capillary flow develops inside the droplet. If the droplet contains particles, this flow will bring the latter to the droplet edge, providing their accumulation at the contact line. This, in turn, enhances the pinning of the contact line and eventually may become a source of pinning instead of surface roughness or chemical heterogeneities [43, 41]. This process is called "self-pinning". It was also shown [74] that the pinning time of the contact line increases with the particle concentration.

When a droplet follows the stick-slip evaporation mode, particles contained in the droplet can also slightly affect the behavior, especially during the "stick" phase, which is similar to the constant radius evaporation mode. It was shown that in some cases, during the "stick" phase, the contact line drifts slowly instead of being pinned [109, 4]. This effect is called "pseudo-pinning". Two possible explanations have been proposed [109]. First, the contact line may re-pin from initial heterogeneity to "self-pin" at the particle assembly at the droplet edge. And instead of staying pinned (as it would have been in case of a real "self-pinning"), the contact line moves from one particle of the assembly to another. If the drift mechanism is insufficient to maintain the contact angle near to its equilibrium value, the imbalance of overall pinning force and the excess of free energy will result in a "slip" phase. Second, the local viscosity next to the contact line may increase due to the particle concentration growth, which results in higher shear forces or a reduced flowrate.

### 4.2.3  Flows inside a droplet in presence of particles

As previously discussed in the section 4.1.2, three main flow configurations may occur inside a pure liquid droplet. The presence of particles was shown to promote the contact line pinning [43, 41] (Fig. 4.8 a). Consequently, the capillary flow is reinforced and lasts longer in the presence of particles. If both Marangoni and capillary flows coexist (Fig. 4.8 b), the Marangoni flow carries particles from the edge to the apex of the droplet, then down to the substrate and finally to the droplet's edge. The third case of capillary flow suppressed by Marangoni flow was less studied, and the illustration of Fig. 4.8 c is just informative and only based on experiments from [35].
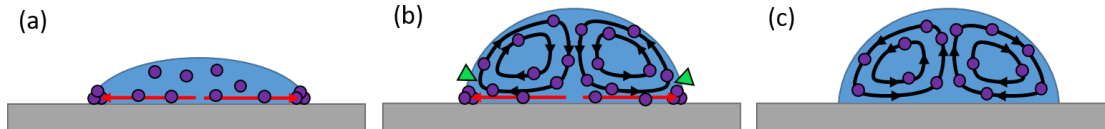


Figure 4.8: Scheme of particle effect on flow within a same droplet: (a) capillary flow brings particles to the droplet edge, (b) Marangoni outward and capillary flows coexist, (c) capillary outward flow is suppressed by Marangoni inward flow.

### 4.2.4  Patterns arising from droplet leftovers

Droplets containing insoluble particles form various deposit patterns on substrates after evaporation (presented in Table 4.2). In what follows, we discuss the conditions leading to the formation of these patterns.

**Coffee-stain pattern (Table 4.2 (a))**

The formation of coffee-stain patterns was first explained in the pioneering work of Deegan *et al.*[42] who made observations of a droplet with particles placed on a hydrophilic substrate with low contact angle. The droplet was evaporating in the constant contact radius mode, i.e., the contact line was pinned. The geometric constraints of a pinned contact line together with the naturally higher evaporation rate at the droplet edge (see Fig. 4.2 a) promote an outward capillary flow within the droplet (see Fig. 4.8 a) that carries particles to the droplet edge and, thus, improves the pinning of the contact line [42]. The microscope observations of particle behavior at the contact line showed the formation of thin layers of aggregates around the droplet (Fig. 4.9). The liquid then evaporates quickly from the upper layer of the aggregates, leading to strong particle adhesion.

To obtain a coffee-ring, it is important that a strong capillary flow has been developed inside a droplet (Fig. 4.8 a&b). If this is not the case, the Marangoni flow reverses the coffee-ring phenomenon (Fig. 4.8 c) and produces deposition at the droplet center rather than at its edge [71]. Moreover, it was shown [90, 94, 166, 121, 154] that coffee-stain patterns are likely to form on hydrophilic substrates, while they hardly form one on hydrophobic substrates.

**Dot-like pattern (Table 4.2 (b))**

The formation of a dot-like self-assembled deposit typically occurs when a droplet follows the constant contact angle evaporation mode. This is likely for a droplet placed on a hydrophobic substrate with the contact line rapidly receding [115, 166]. As drying progresses, the particles within the droplet are compacted and form aggregates [166, 87, 163]. These aggregates sediment
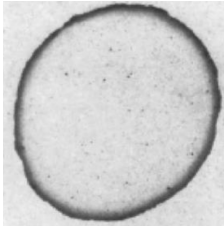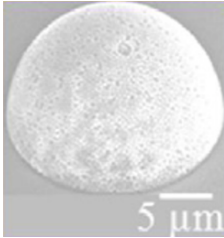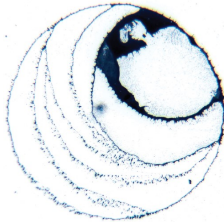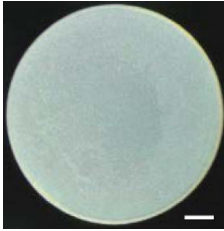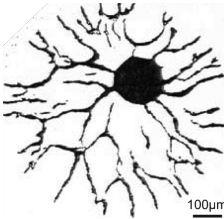
| | Photo | Pattern type & reference | Pattern description |
|---|---|---|---|
| (a) |  | *Coffee-stain pattern.* Image taken from [41]. | The coffee-stain pattern is the particle arrangement in which particles are located at the edge of the droplet, forming so-called "coffee-ring", while in the center there are almost no particles, or at least not large aggregates that could be associated with a shape. |
| (b) |  | *Dot-like (or dome-shaped) pattern.* Images taken from [163]. | In dot-like pattern, all particles are assembled in the droplet center. The deposition can be regular, as presented in the left column, or nonuniform. |
| (c) |  | *Stick-slip pattern.* Image taken from [109]. | The stick-slip pattern consists of several coffee-rings, which are typically pinned to one side of the largest ring. |
| (d) |  | *Uniform pattern.* Image taken from [92]. | The arrangement of particles so that they are evenly spaced is the uniform deposit. |
| (e) |  | *Fingering pattern.* Image taken from [32]. | The fingering pattern is a branch structure induced by the front instability occurring at the contact line with a dewetting behavior. |

Table 4.2: Pattern types arising from the evaporation of a droplet containing particles.

near the contour, but only a small portion of them stick to the substrate, while the majority is swept and finally put at the center of the contact area (Fig. 4.10) [166].

On hydrophobic substrates, the Marangoni flow usually dominates over the outward capillary
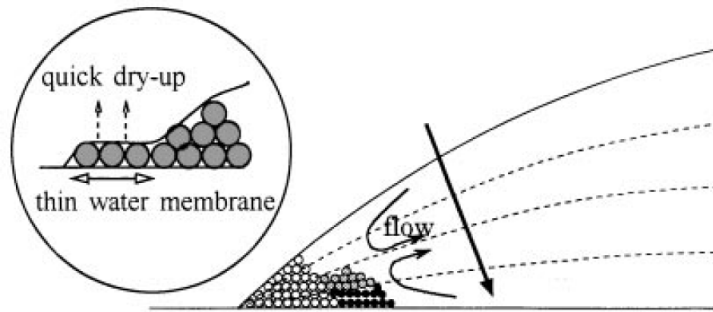
Figure 4.9: Coffee-stain deposit. Image taken from [166].

flow [163] (Fig. 4.8 b). The Marangoni flow makes particles circulate within the droplet and can increase their concentration in the droplet center. This is likely to promote the formation of aggregates. Sometimes, in the late stage of drying, the evaporation can stop the constant contact angle mode, and the contact angle begins to decrease gradually, as it was shown in [163, 87]. By this time, the aggregates are already formed and, despite the reduced effect of Marangoni flow, the dominating outward capillary flow turns out to be ineffective in their transport [163].
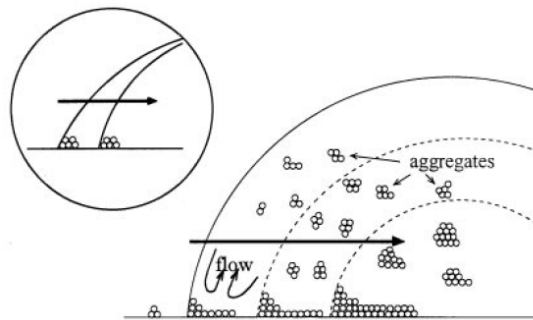


Figure 4.10: Evaporation on a hydrophobic surface. The aggregates are formed and then assembled in the droplet center by the moving contact line. Image taken from [166].

**Stick-slip pattern (Table 4.2 (c))**

Stick-slip pattern results from the stick-slip evaporation mode [109, 4]. The pattern consists of several coffee-rings, which are typically pinned to one side of the largest ring [109]. A set of approximately circular rings appears after complete evaporation. The rings are associated with the "stick" periods, while the "clean surfaces" correspond to "slip" phases [109].

Similar patterns arise in the 5-th evaporation mode (Fig. 4.7) found by Askounis *et al.*[4] (Fig. 4.11). However, compared to the conventional stick-slip pattern, the platelet rings are less uniform and outlined [4].
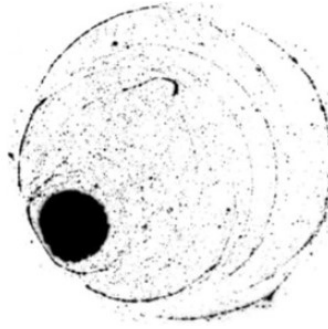
Figure 4.11: Deposit left after the evaporation of ethanol droplet containing graphene platelets. Image taken from [4].

**Uniform pattern (Table 4.2 (d))**

Numerous investigations focused on engineering solutions enabling a uniform deposition, which usually require very specific conditions. We may briefly mention, without going into details, some of the existing methods here. First method combines (i) rapid evaporation and (ii) attractive interaction between particles near the liquid-air interface [14, 92]. The particles are assembled at the droplet interface and then this assembly is deposited on substrate once the liquid is evaporated. The second method relies on the droplet drying in an ethanol vapor atmosphere [98]. The third method proposes the use of very hydrophilic substrates and the proper selection of particle concentration [163]. The forth method suggests the airflow next to the air-liquid interface [181]. More sophisticated approaches propose the reduce pH to create DLVO attraction between particles and a substrate [13] or even change the shape of particles to the ellipsoidal [184].

**Fingering (Table 4.2 (e))**

Various fingering patterns induced by different mechanisms were reported in the literature [122, 123, 168, 32]. A common mechanism leading to such patterns arises from the competition between two different forces [37]. The principle behind instabilities generally relies on local fluctuations in droplet curvature, hence, a variation in the local Laplace pressure. The latter modifies the flow fields [37] resulting from either a gravitational force [53], centrifugal forces [73, 107], temperature gradients [24], or surfactant gradients [150, 37]. For instance, De Dier *et al.*[37] observed fingering formation due to the interplay between capillary and surfactant-induced Marangoni flows. In the first stage, capillary outward flow dominates (Fig. 4.12 a). Then, the surfactant-induced Marangoni vortices develop near the contact line, breaking the axial symmetry of the droplet internal flow (Fig. 4.12 b-d).

The fingering due to the interplay of Marangoni inward flow and outward capillary flow can also arise inside the coffee-ring (Fig. 4.13). The inward flow can be caused by the net capillary force (that pushes particles to the drop center as the contact angle decreases over time) [174, 175], or inward Marangoni flow [175, 37] resulting in "fingers" sticking to the coffee-ring.

### 4.2.5   Effect of particle/substrate properties on droplet leftovers

Throughout the current section, we already mentioned the effect of surface wettability on the obtained deposits. Some other factors, such as the relative humidity, the particle size, the particle concentration, or the particle material, can also affect the deposits. In this subsection, we will
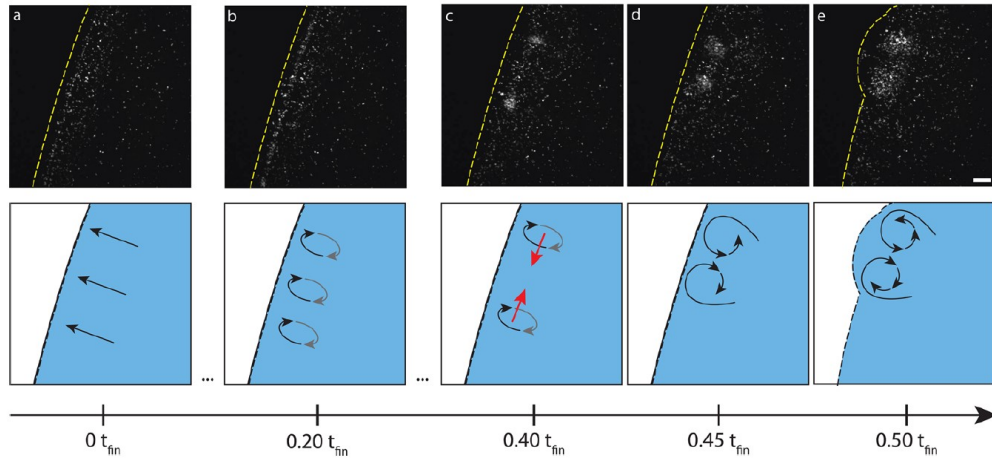
Figure 4.12: The evolution of an evaporating droplet. (a) Particles accumulate at the contact line (dotted yellow line). (b) Surfactant-induced Marangoni vortex develops as sketched qualitatively below. (c and d) Nonaxisymmetric flow near the contact line emerges and creates distinct regions containing a higher concentration of particles that move along the edge and (e) collide upon encounter and locally undulate the contact line of the droplet. The scale bar is 50 µm. Image taken from [37].
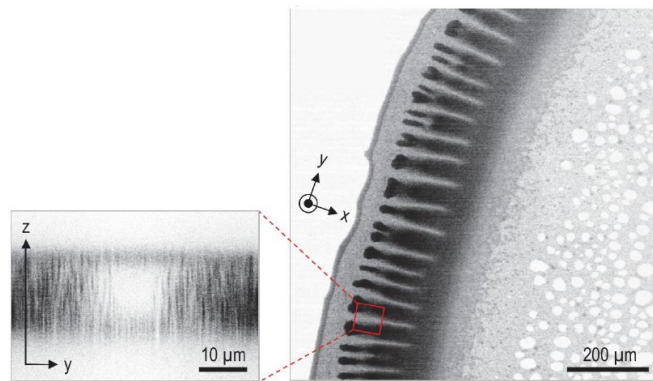


Figure 4.13: Fingering inside coffee-ring. Image taken from [175].

summarize these findings.

**Relative humidity**

Although the relative humidity has no influence on the type of pattern, it has a major impact on an evaporating droplet. First, it affects the liquid-vapor surface tension $\gamma$ [130], which in turn affects the equilibrium contact angle (Eq.(1.26)) [26]. Consequently, the relative humidity affects the droplet spreading area [26, 16], that actually defines the outer ring diameter if coffee-ring or stick-slip patterns are formed. Second, an increase in relative humidity decreases the evaporation rate and vice versa [1, 26]. This affects the drying time of a droplet but not the internal flow motion, which is directly proportional to the evaporation rate, as the intensity of evaporation

scales with the intensity of internal convection [19]. However, the experiments performed by Brutin [19] showed that the spreading area of the droplet with particles was not affected by the change in relative humidity, which contradicts the previous works [26, 16].


**Substrate wettability**

The wettability of a substrate plays an important role in the final particle deposition pattern. Droplet evaporation process is quite different for hydrophilic and hydrophobic substrates. Several authors [90, 94, 166, 121, 154] demonstrated that it is hard to form a coffee-ring deposit on a hydrophobic substrate, while on a hydrophilic substrate it was likely to obtain one. The depinning is typically facilitated by more hydrophobic surfaces [115, 166] where the contact line drags inside the droplet the particle aggregates formed at its edge [166, 163, 87] (see Fig. 4.10). The particle transport inside the droplet is, therefore, different for hydrophobic and hydrophilic substrates, and, consequently, the formed patterns are also different. Patil *et al.*[121] showed that while particles of a drying droplet form a coffee-stain pattern on hydrophilic substrates, they form dot-like patterns on hydrophobic substrates.

Another important factor related to wettability is the contact angle hysteresis. When the substrate has a weak contact angle hysteresis, we observe a self-assembled dot-like pattern after a complete droplet evaporation, while strong contact angle hysteresis contributes to contact line pinning and leads to the formation of coffee-stain deposit [121, 94].


**Particle size**

As one may expect, particle size also affects the resulting patterns [90, 28, 27, 141], but before discussing this, it is worth noting that there are two fundamentally different governing mechanisms with microparticles and nanoparticles. Indeed, particle-particle interactions, liquid evaporation, particle transport by internal flows, and deposit classification are the same for particles down to 5 µm in diameter [141] (Fig. 4.14). However, the patterns are slightly different when obtained using nanoparticles and microparticles of less than 5 µm in diameter (e.g., cracks on coffee rings [19] are mostly specific to patterns obtained with nanoparticles).


**Particle concentration**

The concentration of particles can also affect the deposits, since an increase in the number of particles can change the evaporation mode, by, for instance, increasing the pinning of the contact line. A low number of particles may not lead to enhanced pinning and, evidently, not form any pattern. It was also shown that if the coffee-stain pattern is formed, the ring thickness increases with the increase in the number of particles [148, 19] (Fig. 4.14). At higher concentrations of particles, the pattern can switch from coffee-stain to uniform [90, 163, 141].


**Material of particles**

The material of particles has generally a lesser effect on deposits than the concentration, the particle size, or the substrate wettability. However, it can affect particle-particle interactions as well as particle-substrate interactions through, e.g., zeta-potential. Thus, the material can have some influence on the coffee-ring thickness or on the presence of particle agglomerates in the final deposit [90].
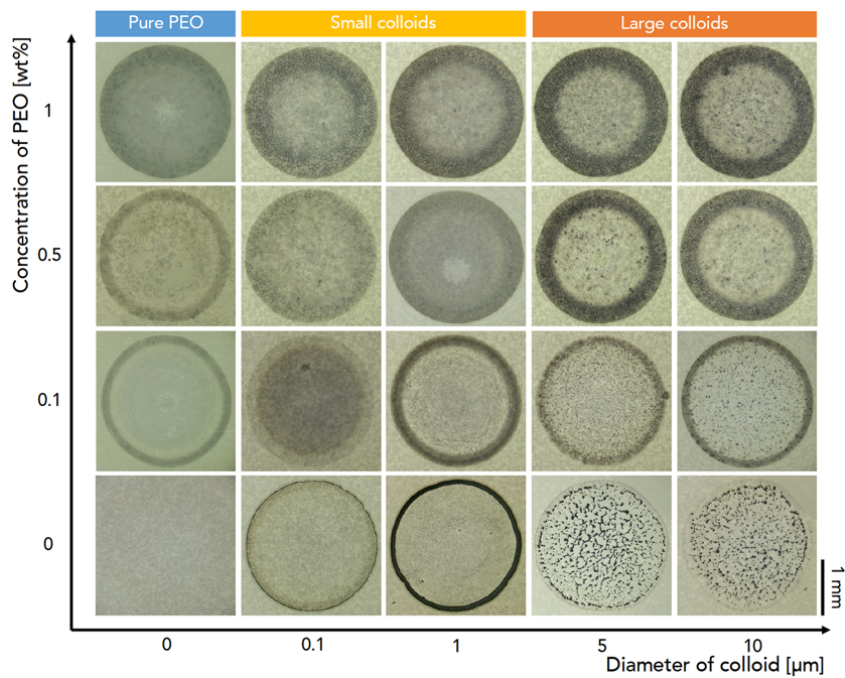
Figure 4.14: Phase diagram for patterns of different particle sizes and concentrations. The particles are polyethylene oxide (PEO) suspended in water with the addition of polymethyl methacrylate. Image taken from [141].

## 4.3 Conclusions

In this chapter, we discussed the life cycle of a droplet with and without particles. We summarized the works done to understand the effects of evaporation, flows inside a droplet, substrate wettability, particle concentration, material, size, and ambient conditions.

In the following chapters, we will attempt to reproduce some of the cited results. We will be mainly interested in very hydrophilic substrates, where the capillary outward flow is strong but the Marangoni flow is negligible. It will be seen that the experimental protocol may greatly affect the developing patterns (Chapter 5). In particular, we will show that the data in the literature are not necessarily reproducible and that a common experimental protocol is required. In Chapter 6 using this protocol, we will uncover a hitherto unknown pattern developing at the contact line.

# Chapter 5

# Implementation of protocol

As previously seen, many reserch works were done to investigate different patterns left after the evaporation of a liquid droplet containing solid particles. Various environmental conditions were tested, and their effect on the final deposit was studied. The point that has attracted less attention from the scientific community appears to be the variety of experimental protocols that were used in these studies. In this chapter, we will draw our attention to the parameters that are rarely mentioned, e.g., aging of particles, presence of surfactant in a purchased suspension, etc., that can potentially affect the final pattern.

In the first section of this chapter, we will discuss the existing protocols. Then, we will establish our experimental protocol to follow. In the following three sections, we explore how changes in drop deposition, suspension and substrate preparations can affect the final pattern.

## 5.1 State-of-the-art

To implement our experimental protocol, we first address the literature regarding how authors prepare their suspensions and how they deposit droplets onto the substrate. In Table 5.1, we present data found in the literature about suspension preparation and drop deposition. As it can be seen, there is no common protocol. The same situation was observed when we investigated the literature to see how the substrates were prepared prior to experimentation.

Here below, we briefly summarize the three unavoidable steps that are associated with the experience of a droplet containing particles.

- Suspension preparation: there are three options for this based on mixing. The first one is the simple manual shaking. This method provides a suspension satisfactory homogeneous, but do not break the eventual particle agglomerates. The second option is the sonication (ultrasonication). The ultrasonic homogenizer generates the ultrasonic high pressure waves in a dispersion. The dispersed phase vibrates in all directions, eventually breaking the particle aggregates. The last option is vortexing. Vortex mixers generate strong velocity gradients. In consequence, the dispersed phase is subjected to viscous shear, that can also break the particle aggregates.

- Droplet deposition: two basic methods were found in the literature. The first one is the deposition using some electronic devices, e.g., an electronic syringe. And the second one

is the manual deposition using a micropipette. The first method is supposed to be more precise, but we will show in the section 5.3 that the difference is not very significant.

- Surface cleaning of the substrate on which the droplets will be deposited: there is no common protocol. Mostly, the substrates are cleaned in order to remove organic contaminants, but sometimes they are used as is. In this case, the substrates are most likely already contaminated with some organic dirts prior to experimentations.

| Reference | Mixing option | Deposition | Substrate cleaning |
|---|---|---|---|
| Askounis *et al.* [4] | sonication for at least 30 min | deposition using a drop shape analyzer equipped with a motorized dosage system | cleaned in an iso-propanol ultrasonic bath and then blow-dried using a jet of compressed air |
| Anyfantakis *et al.* [2] | vortexed for 1 min and mixed 15 s, than sonicated for 1 min and mixed again for 1 min | deposition using a micropipette | as is |
| Bhardwaj *et al.* [13] | sonicated for 5 min | deposition using stainless steel pin | piranha-cleaned |
| Brutin [19] | suspension stability was guaranteed by the presence of carboxylate surface functional groups on the surface of the nanoparticles | deposition using electronic syringe | not mentioned |
| Dadjoo *et al.* [33] | mechanical mixer at several stages, then sonicated for 1 h | not applied | not applied |
| Hu *et al.* [72] | suspension was left to equilibrate for 48 h before use | deposition using a micropipette | acetone and ethanol |
| Jeong *et al.* [77] | not mentioned | not mentioned | as is |
| Iqbal *et al.* [75] | not mentioned | not mentioned | not mentioned |
| Kwark *et al.* [88] | sonicated for 2 h | not applied | not applied |
| Kuncicky & Velev [87] | not mentioned | not mentioned | cleaned in Nochromix, then rinsed with deionized water |
| Lee *et al.*[90] | ultrasonic bath (time not precised) | deposition with a micropipette | ultrasonic bath and then with acetone |
| Li *et al.*[94] | not mentioned | not mentioned | cleaned with deionized water and ethanol |
| Li *et al.*[93] | not mentioned | not mentioned | ultrasonically cleaned first in isopropanol, then in deionized water |
| Li *et al.*[92] | not mentioned | not mentioned | not mentioned |
| Madivala *et al.*[95] | manually shaken for about 1 min | not applied | not applied |
| Majumder *et al.*[98] | not mentioned | deposition with a micropipette | not mentioned |
| Manukyan *et al.*[99] | not mentioned | not mentioned | not mentioned |
| Monteux & Lequeux [110] | not mentioned | not mentioned | rinsed substrates with ethanol and distilled water |

| | | | |
|---|---|---|---|
| Moffat *et al.*[109] | sonicated for 1 h | deposited with the Kruss DSA 100 drop shape analyzer | cleaned by immersing each substrate in an ultrasonic bath of isopropanol for 15 min, then blow-dried using a jet of compressed air |
| Orejon *et al.*[115] | sonicated for 1 h | not mentioned | cleaned in an ultrasonic bath with isopropanol for 15 minutes, then dried with nitrogen stream |
| Patil *et al.*[121] | sonicated for 1 h | deposited using a micropipette | sequentially cleaned by isopropanol and deionized water, then allowed to dry in ambient conditions |
| Pradhan & Panigrahi [128] | not mentioned | not mentioned | not mentioned |
| Sefiane [148] | not mentioned | deposited with the Kruss DSA 100 drop shape analyzer | substrate first immersed in a bath of IPA for approximately 5 minutes, then blow-dried with compressed air |
| Uno *et al.*[166] | not mentioned | not mentioned | cleaned by dipping in concentrated sulfuric acid and concentrated nitric acid solutions and rinsed repeatedly with pure water |
| Wong *et al.*[176] | not mentioned | not mentioned | not mentioned |

Table 5.1: Data found in literature about suspension preparation and drop deposition. The "not applied" statement means that for the studied configuration, this parameter could be omitted (e.g., deposition of suspension in a vessel [33]).

In what follows, we will establish our own protocol and discuss how changes in the protocol can affect the final result.

## 5.2 A basic experimental protocol

### 5.2.1 Suspension preparation

In our experiments, we used Red Fluorescent Polystyrene particles (Thermo Scientific) having a diameter of $d = 1\,\mu m$ (CV $< 5\%$). More precisely, the mean diameters of $1\,\mu m$ particles measured post-production by Thermo Scientific are of $1.1\,\mu m$ but in what follows we refer to them as particles of $1\,\mu m$ in diameter. The particles have a density of $\rho = 1.05\,g/cm^3$ and they are delivered as a suspension having $1\%$ of solids. Unfortunately, we could not measure the zeta potential of our suspension, as we only have a laser-based zeta-meter, which is not appropriate for the fluorescent particles we use. In the literature we found a value around $-40\,mV$ [179] for polystyrene particles of smaller diameter ($40\,nm$) from the same manufacturer at $pH = 7$. This corresponds to a good stability (see Table 4.1). Since zeta potential reflects surface charges, it is not supposed to significantly change with the particle size.

According to the seller, particles delivered in suspension can contain trace amounts of surfactant to inhibit agglomeration and promote stability. When we used the particles as is, these additives made the liquid drop spread extensively (see section 5.4.1 for details). Moreover, the exact

product used as a surfactant as well as its quantity are unknown. So, before use, the particles were washed three times in order to remove surfactant traces and, consequently, avoid the excessive spreading. Each wash consisted of two steps. First, the tube containing particle suspension is put in a centrifuge for 15 min at 1500 rpm to force particle sedimentation. Then, the upper layer of the liquid with the additives is removed using a pipette and the same volume of deionized water is added to the particles. After each wash, the mixture is re-suspended for about 15 s using a vortex mixer and then for 210 s by means of an ultrasonic bath. Since we removed chemical additives from particle suspension, the zeta potential could change, and this is what we observed. In the washed suspension, aggregates form within several weeks, and there is significantly faster particle sedimentation with "phase separation" (i.e., all particles are sedimented to the bottom of a tube containing suspension) compared to the non-washed suspension, where particles and the volume fraction of particles is higher at the bottom of a tube sediment, but "phase separation" was never observed.

After the first step, which consists of the particle wash, we sonicate the suspension for 2 to 5 minutes to make it uniform. Then, we take a small volume of concentrated particles and dilute it in deionized water to have the concentration $N = 2.25 \times 10^9$ particles/mL or concentration $c = 0.1237\%$ w/v or $c = 0.1178\%$ v/v. As one can see above, the concentration can be measured as the number of particles in 1 mL of suspension; as weight per volume (w/v, %), i.e., the ratio between mass of solute (in g) and volume of suspension (in mL); or as volume per volume (v/v, %), i.e., the ratio between the volume of solute and the volume of suspension.

The suspension was sonicated for 2 minutes right before each drop deposition for experimentation. The time required for sedimentation per 1 mm (which is the characteristic height of a liquid layer in a plastic tube, where our suspension is prepared) calculated using Eq.(4.3) was estimated as 9.6 h, which ensures maintaining the suspension homogeneity during droplet deposition within a maximum of 15 min after sonication.

## 5.2.2 Substrate preparation

We used both-sides polished borosilicate glass wafers (Neyco) having a diameter of 76.2 mm and a thickness of 1.1 mm. Before experiments, wafers were washed using piranha solution, which is prepared by adding 1 part of 30% hydrogen peroxide $H_2O_2$ to 3 parts of 96% sulfiric acid $H_2SO_4$ slowly (and not in reverse order!). The glass substrate stays in piranha solution for 2 to 5 minutes, depending on its anterior cleanliness. After that, the substrate is put in the deionized water for several minutes. Finally, the substrate is dried using nitrogen dioxide ($N_2$) jet. After the wash, the substrate is used for experimentations no earlier than 6 hours and no later than 24 hours (the effect of time between the wash and the use is discussed in the section 5.5.1). The contact angle of a piranha-cleaned substrate with pure water is 2° (measured with Biolin Theta Lite). As we were using optical tensiometer, the accuracy of the contact angle measurements is low for small contact angles. Since we will not perform further calculations with the contact angle, we will consider 2° as the representative contact angle value to empathize that the wafers are very hydrophilic. The mean roughness of the substrate surface was found to be 3.4 nm by AFM (Bruker Dimension Icon AFM) measurements.

## 5.2.3 Drop deposition

All experiments were performed in the room with the controlled temperature of 20 °C. The humidity, on the other hand, was not controlled and varied between 30% and 60% depending on environmental conditions.

The droplets have a volume of 15 µL and are manually deposited on a wafer with a pipette.

Before deposition, the horizontal position of the wafer is verified with a spirit level (the error is less than $0.5°$). Typically, we deposit 5 to 8 droplets[1] on the same glass substrate and let them evaporate. The duration of the drying is about 40 min. The scheme of the setup is presented in Fig. 5.1. After the complete evaporation, photos are taken from the bottom of the substrate using a camera (Nikon D750 with the objectif Nikon 25 mm). The resulting image is $6016 \times 4016$ pixels.
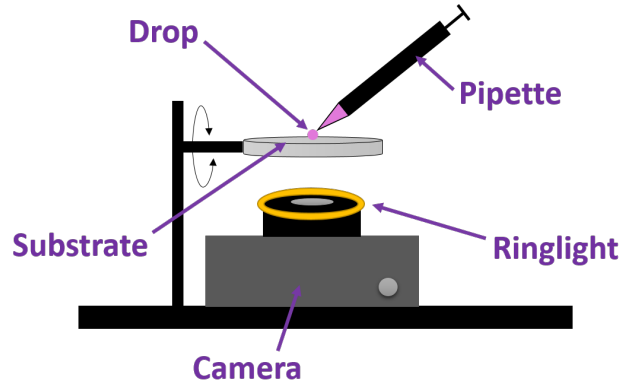


Figure 5.1: Scheme of the setup.

### 5.2.4   Patterns observed under a basic protocol

As mentioned before, the droplet is deposited on a hydrophilic substrate and left to evaporate at a controlled temperature of $20°$C. According to the previous studies [42, 90], we are likely to obtain coffee-stain-like patterns after complete evaporation on a hydrophilic substrate [166]. Fig. 5.2 presents the patterns obtained with the above experimental protocol. From these photos, one can see that the droplet contact radius $R_c$ is about 3.5 mm. This gives a Bond number $Bo \approx 1.65$ calculated from Eq.(1.28) with droplet contact radius taken as the characteristic length.

Here, we can distinguish four main types of patterns. The first one (Fig. 5.2a) is a coffee-ring with a uniform deposition in the center. The second is a coffee-ring, where only a part of the inside of the droplet is uniformly covered with particles. There is a second "ring" (which resembles more to a very elongated ring) inside the main one. The third pattern is presented in Fig. 5.2c. It is a coffee-ring with two zones, a uniform deposition and "instabilities". In the presented photo, there are two instabilities. The first one is located inside the main coffee-ring and has its own edge of increased height. The other instability is attached to the coffee-ring and does not have an edge of increased height. The last type is the totally unstable pattern shown in Fig. 5.2d. It consists of coffee-ring pieces scattered inside the original drop position (before evaporation).

As mentioned, we usually put 5 to 8 drops on one substrate at a time, and the patterns left after these drops drying are very similar. However, if we put identical drops after some time on the same substrate, we obtain a different set of patterns (although they will be similar to each other this time, too). Therefore, we faced the difficulty to do reliable statistics (i.e., the probability of obtaining a particular kind of pattern), as the patterns appeared too random from what we observed. For example, we had a week with only unstable patterns with no coffee-stain

---

[1]Usually, all droplets placed on the same substrate produce similar patterns regardless of the number of neighbors they have. Moreover, we did not observe qualitative changes in obtained patterns, if only one droplet had been placed on the substrate. Therefore, based on our experimental observations, we suppose that the evaporating droplets do not significantly affect each other.
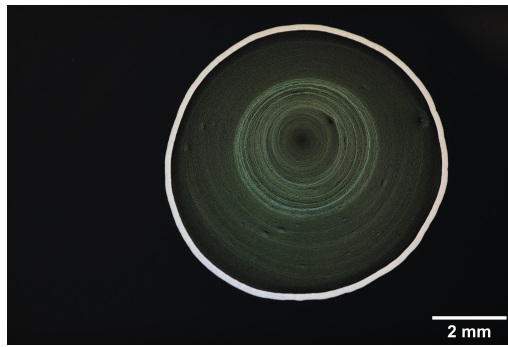
(a) A coffee-ring with uniform particle distribution inside (11 days). The substrate was cleaned 24 hours prior to the drop deposition.
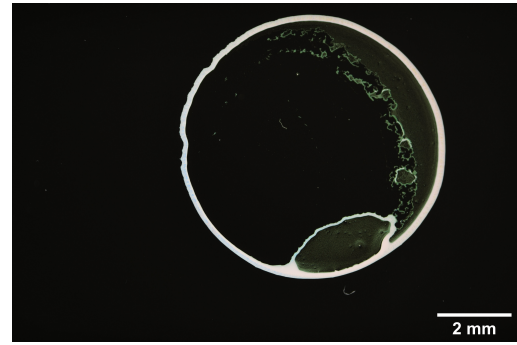


(b) A coffee-ring with partially uniform distribution and a second contour inside (20 days). The substrate was cleaned 17 hours prior to the drop deposition.
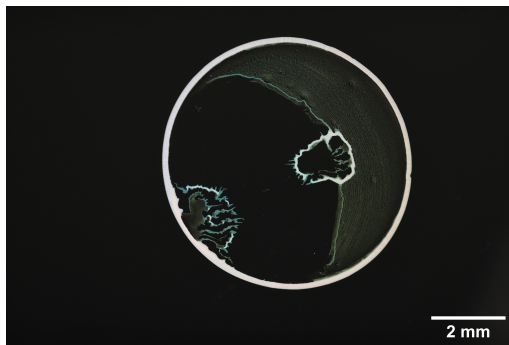


(c) A coffee-ring with a uniform deposition zone and "instabilities" (4 days). The substrate was cleaned 8 hours prior to the drop deposition.
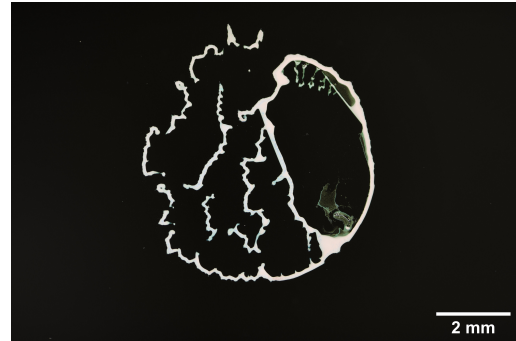


(d) Unstable pattern (20 days). The substrate was cleaned 22 hours prior to the drop deposition.

Figure 5.2: Four different patterns obtained after following our protocol. The time in brackets indicates the suspension age. The time between the substrate cleaning and the drop deposition is also given for each pattern. It will be discussed in detail in the section 5.5.1.

deposits, but the following week it was really hard to obtain the unstable pattern. Our hypothesis is that the patterns may have been affected by the ambient humidity or the air flows in the room from the air conditioner, which were out of our control. Nevertheless, the instabilities that we observed in Fig. 5.2d are original. To the best of our knowledge, this type of instabilities has never been decribed in literature before. We will discuss the formation of these instabilities in detail in Chapter 6.

### 5.2.5 Discussion about suspension age

We use the particles for a certain period of time (about 1 month) after washing. So, before going any further, it is important to understand whether the particle properties had an effect on the obtained patterns. From Fig. 5.2, we cannot see the clear effect of suspension age on particle deposition. The coffee-ring appeared after 4, 11 and 20 days after the suspension wash. Among the presented photos, one can say that the suspension age increases the probability of obtaining the unstable pattern. However, from other sets of experiments, we can claim that the unstable

pattern can be obtained even with 1-day-old suspension. Moreover, Fig. 5.2b and Fig. 5.2d were both obtained 20 days after washing. Additionally, Fig. 5.2c was deposited 4 days after particle wash but still has unstable parts unlike Fig. 5.2a deposited after 11 days.

When our washed suspension becomes too old (about 1 month after washing), we observe "clouds" within a deposit (Fig. 5.3), that can be both, regular coffee-ring or unstable pattern. These clouds arise probably from the organic contaminants developing in the suspention. After wash, the concentrated particles are stored in a plastic tube. Before drop deposition, we take some amount of these concentrated suspension and dilute it, so the tube is accessed multiple times. Probably, this step is a source of contamination.
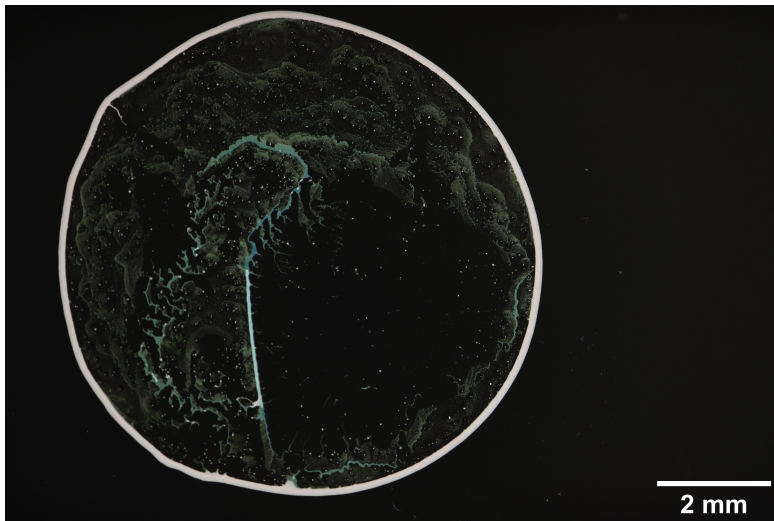


Figure 5.3: The "clouds" observed within the droplet leftovers when using the suspension 1 month and 1 week after particle wash.

We have seen a variety of patterns developing under the basic protocol. In what follows, we investigate how a change in one of the protocol parameters can affect the final deposit. We will vary the following parameters:

- drop deposition method
- presence of surfactant (use of suspension as is or washed)
- mixing option
- time between cleaning of substrate and drop deposition

while the other parameters will remain unchanged.

## 5.3   Effect of drop deposition method

As we could see from the section 5.1, there are two basic options for drop deposition. The first one is the deposition using a motorized dosage system, and the second one is the manual deposition using a micropipette. We did not have the motorized system but created one using a pipette connected, by means of a microfluidic tube, to a syringe placed on a syringe pump (Fig. 5.4).
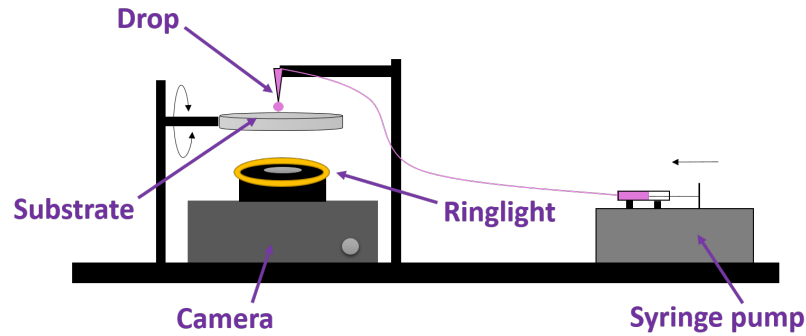
Figure 5.4: Scheme of setup with syringe pump deposition.

The pump injected the fluid at a flowrate of around $2\,\mu\mathrm{L/s}$ through the system until the fall of the droplet formed at the pipette tip, that occurs when gravity dominates over capillary forces. The volume of a droplet, therefore, depends on the pipette tip chosen. We tested several tips and selected one giving the droplet volume of $16.1 \pm 0.1\,\mu\mathrm{L}$, which is close to $15\,\mu\mathrm{L}$ droplet used in the basic protocol deopsited manually with a pipette.

The obtained patterns (Fig. 5.5) were found to be similar to those obtained following the basic protocol (Fig. 5.2). We did not see any patterns of Figs. 5.2c, 5.2d, but we believe that this is due to the reduced number of experiments compared to the basic protocol.
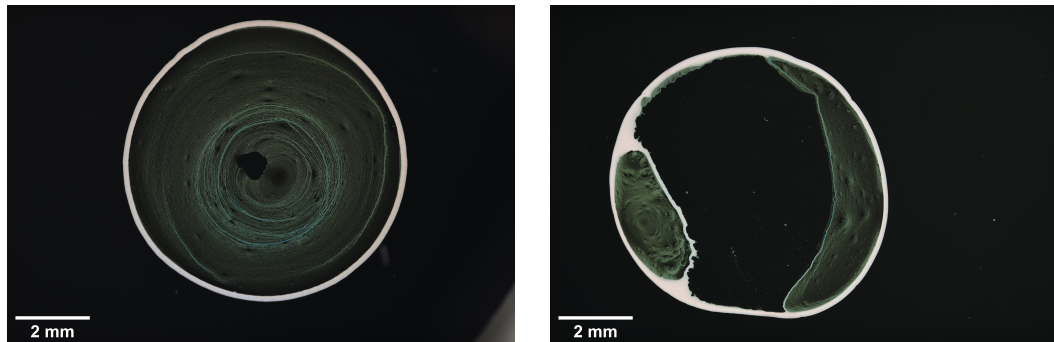


(a) Coffee-ring with uniform particle distribution inside.

(b) Coffee-ring with partially uniform distribution and second contour inside.

Figure 5.5: Patterns obtained when depositing droplets using a syringe pump, as shown in Fig. 5.4.

## 5.4 Effect of suspension preparation

### 5.4.1 Effect of surfactant presence

As stated before, the particles we use as is, can contain some traces of surfactant according to the supplier. If we do not wash the particles following to the described protocol, the obtained patterns are different (Fig. 5.6). The droplet leftover has a larger area with respect to the patterns

obtained following our basic protocol. Also, the coffee-ring is uneven, and the particles inside the coffee-ring form a grid.
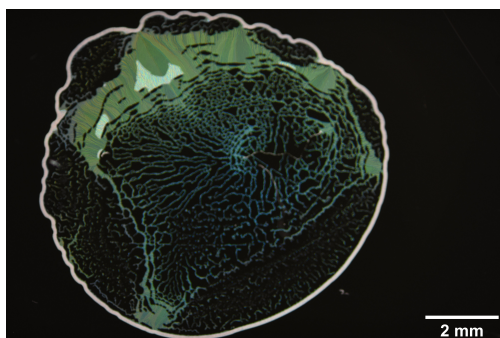


Figure 5.6: Deposit obtained after complete evaporation of a "nonwashed" suspension.

### 5.4.2   Effect of mixing option

We suspended the suspension using vortex mixer (Velp Scientifica ZX3) in continuous mode at 2000 rpm for 2 min instead of sonication. We deposited droplets with the sirynge pump, following the protocol described above. The obtained deposits (Fig. 5.7) are similar to those obtained after sonication (Fig. 5.2).

## 5.5   Effect of substrate preparation

### 5.5.1   Effect of substrate cleaning

As it was mentioned above, we clean our substrates using a piranha solution. In our basic protocol, we deposit droplets 6 to 24 hours after cleaning. In this subsection, we are interested in how the time after cleaning affects the final particle leftovers.

We distinguished several stages of substrate aging: (i) 1 to 5 hours, (ii) 6 to 24 hours, (iii) 1 to 4 days, and (iv) more than 4 days. Between the substrate cleaning and the drop deposition, the substrates are stored in a closed plastic box in a room at a controlled temperature of $20\,°C$ with daylight or electric light during the day and no light during the night.

#### (i) Drop deposition 1 to 5 hours after cleaning

If we deposit a droplet onto the substrate 1 to 5 hours after substrate cleaning, the droplet will spread more than it is usually observed to spread (Fig. 5.8). The coffee-ring is generally irregular and not axially symmetric.

#### (ii) Drop deposition 6 to 24 hours after cleaning

The deposition 6 to 24 hours after substrate cleaning is the protocol we usually follow. The obtained patterns are those already pictured in Fig. 5.2. The exact time between cleaning and drop deposition is noted below each image. One can see that there is no correlation between pattern type and the time between substrate cleaning and drop deposition if this time is within the range of 6 to 24 hours.
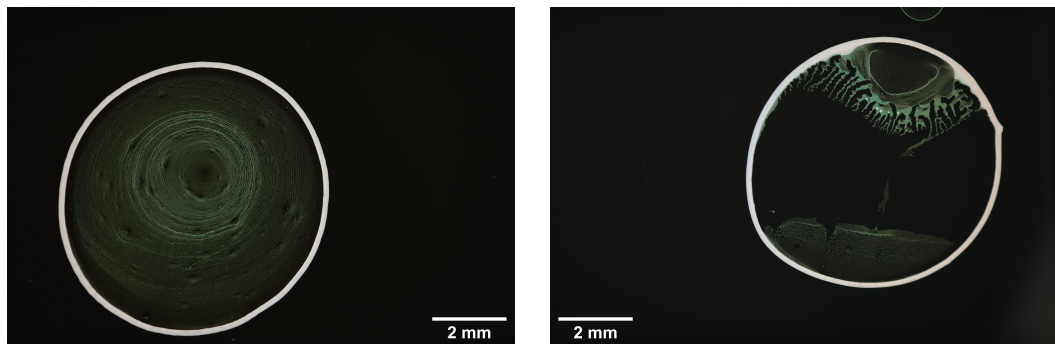
(a) Coffee-ring with a uniform particle distribution inside.



(b) Coffee-ring with a uniform deposition zone and "instabilities".
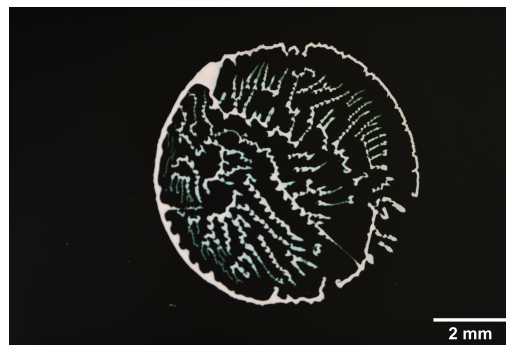


(c) Unstable pattern.

Figure 5.7: Patterns obtained after using a vortex mixer instead of sonication.

### (iii) Drop deposition 1 to 4 days after cleaning

Fig. 5.9 presents droplet leftovers obtained when the droplets were put on the substrate cleaned 3 days prior to the deposition. In this case, we observe a coffee-ring with a nonuniform particle distribution inside (Fig. 5.9 a) as well as an unstable pattern (Fig. 5.9 b).
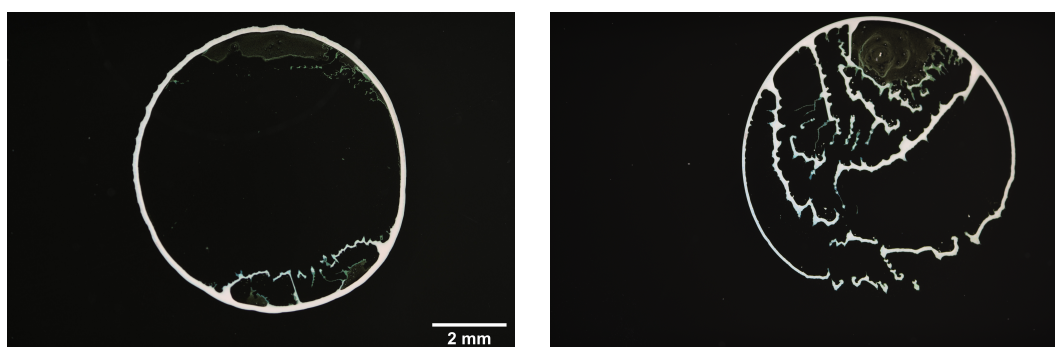


(a)



(b)

Figure 5.9: Patterns obtained when droplets are deposited on the substrate 3 days after cleaning.

(a) (b)
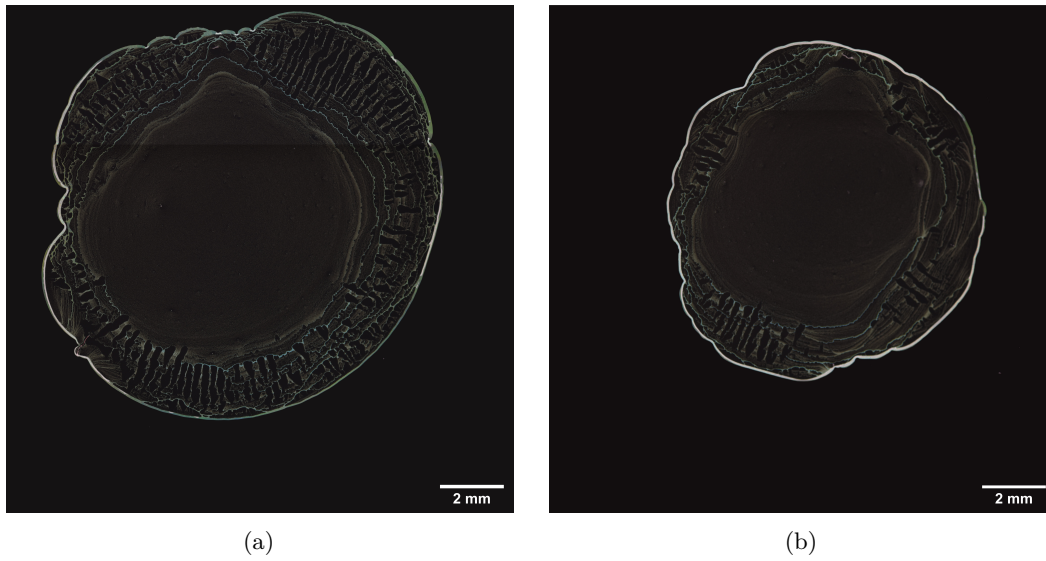
Figure 5.8: Deposits obtained when droplet is put on the substrate 1 to 5 hours after piranha cleaning.

**(iv) Drop deposition more than 4 days after cleaning**

Fig. 5.10 presents deposits obtained 7 days after substrate cleaning. The substrate is probably contaminated with some organic dirt and oxidized, and the obtained patterns are irregular.
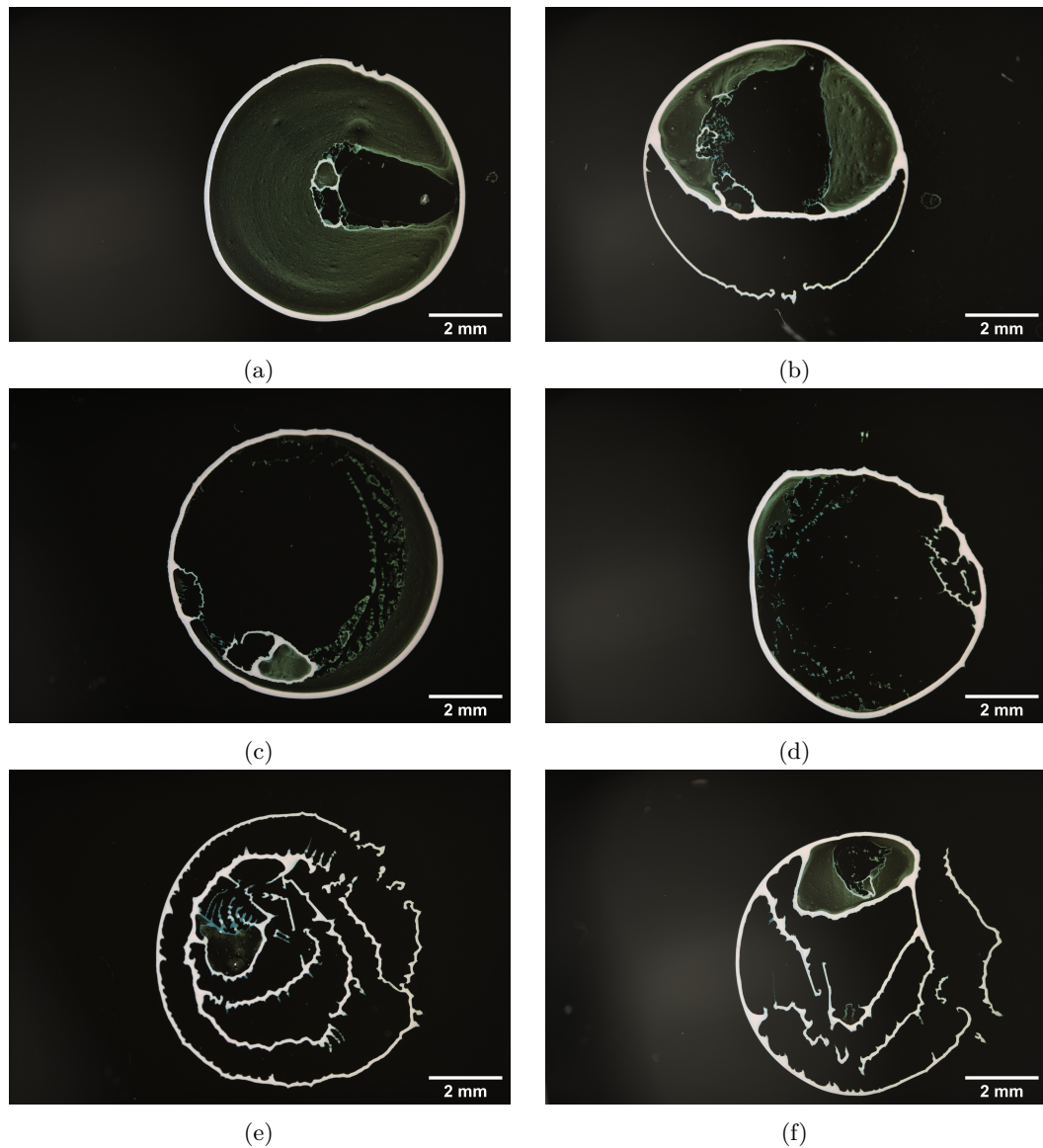
Figure 5.10: Patterns obtained when the droplet is put on the substrate 7 days after cleaning.

We can state that the use of substrates cleaned more than 4 days before the drop deposition significantly increases the probability of having unstable patterns (Figs. 5.10e and 5.10f) and uneven coffee-rings (Fig. 5.10d), while coffee-rings with the uniform particle distribution like that of Fig. 5.2a are very rarely observed. All the patterns presented in Fig. 5.10 have instabilities inside and/or at the edge of the coffee-ring.

### 5.5.2  Effect of non-organic residuals left after polishing

In our experiments, we reuse the glass substrates after the experiment by going through the cleaning procedure. Often (but not every time!), after the deposition of a droplet for the first

time, and subsequent removal of its leftovers with piranha solution, we observed a "wall" molding a part of the contour of the droplet before evaporation. An AFM scan of this "wall" is presented in Fig. 5.11b, and the substrate without a defect is shown in Fig. 5.11a. Probably, this "wall" arises from the residuals (e.g., diamond grit or remains of glass) that are left on the glass after polishment processed by the wafer manufacturer. These residuals are nano-sized particles. They are not removed after piranha cleaning and stay on the substrate. When the droplet containing microparticles is added to the substrate, it covers the residuals. The latter are likely collected by the droplet and start moving, obeying outward capillary flow. Since their size is smaller than that of the tested particles, they are brought farther to the droplet edge by the capillary flow than the micron-sized particles, and a double coffee-ring made by nanoparticles surrounding the micron-sized particles is then formed. The external coffee-ring consists of nanoparticles, and the internal one – of microparticles. This would correspond to the previous studies [77] stating that smaller particles would be carried farther away from the center.
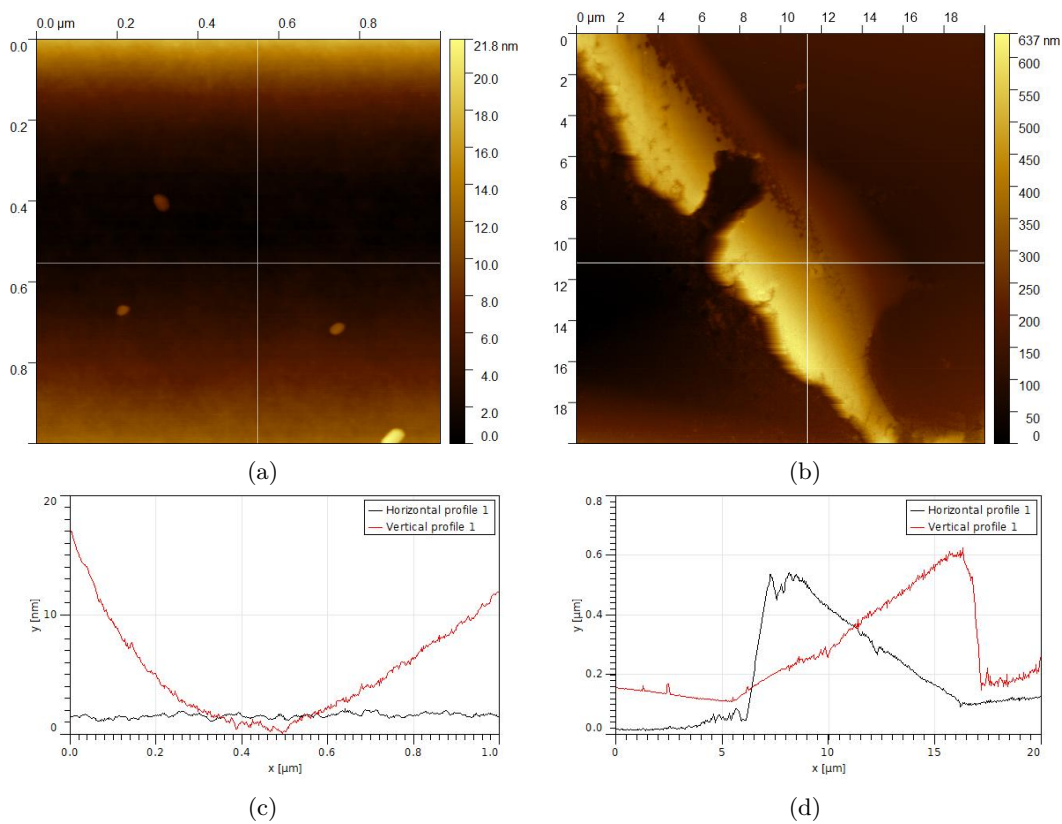


Figure 5.11: AFM scans of the substrate: (a) with no defect, (b) with a wall formed out of residuals. Profiles corresponding to the AFM scan of the substrate: (c) with no defect and (d) with a defect. The "horizontal profile" and the "vertical profile" in the legends of (c) and (d) correspond to the profiles along horizontal and vertical lines of (a) and (b), respectively. The "points" we observe are organic contaminants.

The "wall" height increases linearly from the internal side of the droplet, and suddenly decreases from the external side of the droplet. Probably, it was micron-sized particles that smoothed the internal side of the "wall" of residuals. The wall height is about $0.7\,\mu m$, which is of

the order of our particles size. When we perform our experiments, we try to avoid the spots with these "walls". They are typically visible on a substrate to the naked eye. If we miss such a "wall" and deposit a droplet on it, we will notice the "wall" from the resulting pattern (Fig. 5.12). The particle are only concentrated from one side of the "wall", while other side is empty. Moreover, the arch shape of this "wall" is clear from Fig. 5.12.
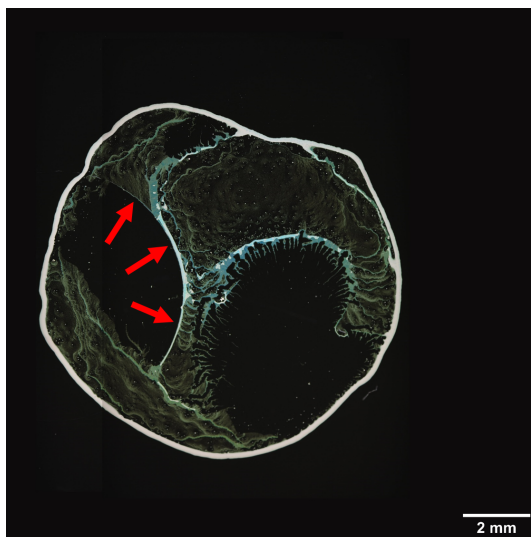


Figure 5.12: Example of pattern affected by the residual "wall". The red arrows indicate the "wall". When this droplet was deposited, the suspension was already 5 weeks old, so we observe "clouds".

## 5.6 Conclusions

In this chapter, we studied the patterns obtained after drying a droplet containing micron-sized particles placed on polished borosilicate glass as well as the sensitivity of these patterns to changes in the experimental protocol. We observed the high variability of patterns. Unlike previous studies, where one type of pattern was usually observed under the same experimental conditions, we had several different patterns for each experimental condition. We also observed an unstable pattern, which, to our knowledge, has not been previously reported in the literature. Unfortunately, we could not clearly identify the conditions that led to the formation of the unstable pattern. We can only speculate that its formation may be related to the smoothness of our substrate as well as the slippage of the coffee-ring over the substrate (we will discuss this in more detail in the next chapter). The relative humidity and air flows in the room could not be controlled and may also affect the resulting pattern.

We tested the sensitivity of our patterns to changes in experimental conditions such as:

- drop deposition method
- presence of surfactant (use of suspension as is or washed)
- mixing option
- time between cleaning of substrate and drop deposition

We found that the following parameters have the greatest influence on the pattern: the washing of the suspension and the time between substrate cleaning and drop deposition. The non-washed

suspension contains an unknown surfactant that promotes the excessive spreading of the drop. Additionally, we discussed the effect of the suspension age. Although the effect on the obtained patterns is not very pronounced for the "young" suspensions under 1 month of age, we saw the formation of particle agglomerates due to contaminants in suspensions older than 1 month. This contamination causes the appearance of "clouds" inside the pattern. The time between the cleaning of the substrate and the drop deposition is also critical, as it controls the droplet spreading over the substrate. Deposition of the droplet immediately after substrate cleaning leads to excessive droplet spreading, while deposition after waiting too long leads to contamination of the substrates and uneven patterns.

From the observations made in this chapter, we propose an experimental protocol that appears to give a variety of patterns This protocol consists of:

- a suspension washed no more than 1 month ago
- a piranha-cleaned substrate aging for at least 6 hours but no older than 24 hours
- a mixing of the suspension during 2 minutes by means of sonication just before the deposition

Following this protocol, we statistically obtained as many coffee-stain patterns as we could. To increase the probability of "unstable" patterns that will be of interest in the next chapter, we will use piranha-cleaned substrates aging more than 1 day.

# Chapter 6

# Experiments and observations

Many studies were devoted to the coffee-ring and other "regular" patterns. The "irregular" patterns observed in the literature [37, 122, 123, 32] are very different from the unstable patterns described in Chapter 5. To the best of our knowledge, these patterns were never reported in the literature. In this chapter, we make careful observations of the formation of different patterns and describe in detail these new unstable patterns (that we call "braids" in this work).

## 6.1   Introduction to instabilities

When a droplet is deposited on a substrate, one generally observes first its spreading prior to observe the effect of evaporation. In the case of an aqueous liquid on a hydrophilic substrate, a radial flow develops inside the droplet that would bring particles, eventually contained in the droplet, near the contact line. As a consequence, a commonly called coffee-ring is formed [42].

In Chapter 5, we showed the emergence of both stable and unstable patterns during the evaporation under the same experimental protocol. It appears that the unstable patterns show some characteristics (Figs. 5.2c,5.2d,5.7c, 5.9 & 5.10) that seem quite different from those hitherto reported in the literature. Indeed, sometimes no coffee-ring is formed (Fig. 5.2d), sometimes the coffee-ring is uneven (Fig. 5.10d) or sometimes instabilities are formed inside the coffee-ring (Fig. 5.2c).

Among all unstable deposits, we distinguish a pseudo-periodic pattern that can occur either after the formation of the main coffee-ring in the inner area (Fig. 6.1a) or simply form instead of some section of a coffee-ring (Fig. 6.1b). Nevertheless, these structures are similar, and we will refer to them as "braids" as they are made up of elements clinging to each other. Sometimes they form a long chain like those in Fig. 6.1b, but they can also be shorter. However, we usually observe multiple pseudo-parallel braids in the same area. We will discuss them in detail below.

To understand the mechanisms leading to instabilities, we performed macroscopic and microscopic observations. To do so, we observed droplets made using the protocol described previously (see section 5.2) but with volumes of 10 µL instead of 15 µL. The change of volume was done to reduce the evaporation time. These droplets behave qualitatively in the exact same way as 15 µL droplets and form the same patterns. This was done to reduce the number of frames acquired during the evaporation of a droplet and thus facilitate the data treatment (the size of the video recorded with the microscope camera usually exceeds 40 GB).

In what follows, we will present the results of macroscopic and microscopic observations of
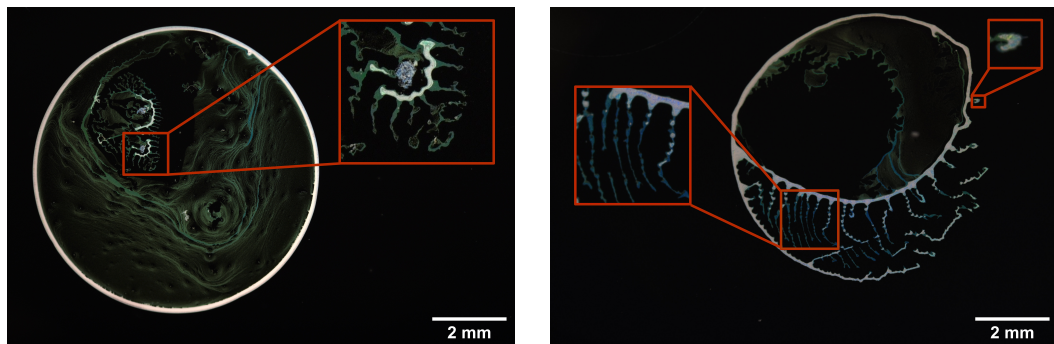
(a) Instabilities in the droplet center.          (b) "Outer" instabilities.

Figure 6.1: "Braids" in the droplet center and at the droplet edge.

evaporating droplets. As it was mentioned in the previous chapter, the relative humidity in the experimental room was out of our control, therefore, the drying time was different for different droplets and ranged from 35 to 50 minutes for droplets of 10 μL.

## 6.2   Macroscopic view

We slightly modified the setup described previously (Fig. 5.1) by replacing the ringlight placed on the camera objective with a light placed from the top, accompanied by a light diffuser (Fig. 6.2). This modification was done to prevent any heating of the substrate during the evaporation process.
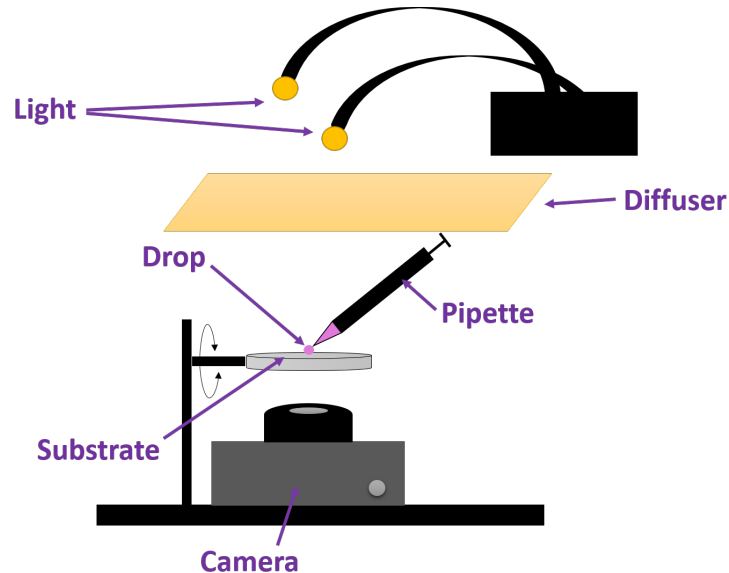


Figure 6.2: Setup with modified light to avoid heating of a droplet during its evaporation.

Fig. 6.3 presents the last stages of the drying process. The time in the top right corner

corresponds to the time (in minutes) since droplet deposition (the possible error is about $30\,\mathrm{s}$ which corresponds to the time between drop deposition and manually pressing "start" on a computer for image recording). During the first $38\,\mathrm{min}$ of evaporation, the contact line is pinned and the droplet appears in its entire shape as yellow disks and the pictures are similar to the first shown in Fig. 6.3 at the time $t = 38:30$. Starting from $t = 39\,\mathrm{min}$, the droplet depins from the coffee-ring at one side while remaining pinned on the other. By $42:30$, the droplet completely depins from the peripheral coffee-ring and forms an unstable deposit in the inside region of the droplet leftovers. The droplet leftover is presented in Fig. 6.1a in better quality (the difference in color is just due to the lighting that was changed when taking the high quality picture). One can
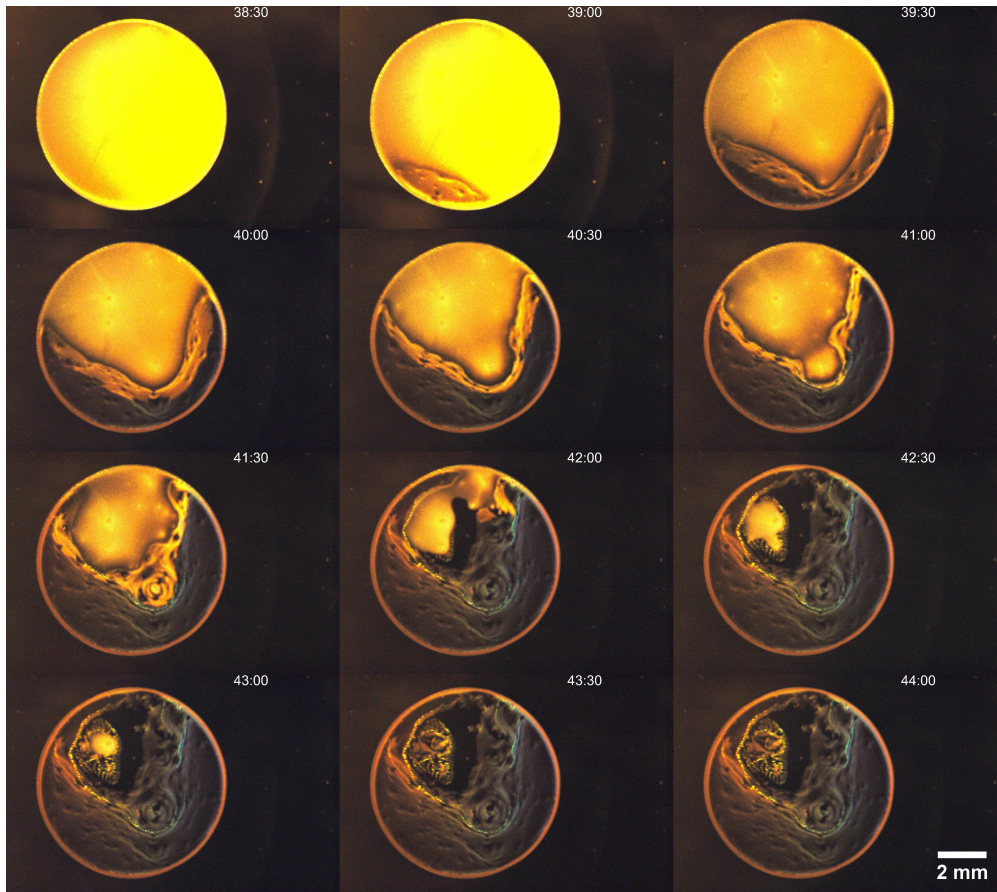


Figure 6.3: Timelapses of the droplet drying process. The photos are taken every $30\,\mathrm{s}$. The time in the top right corner corresponds to the time in minutes since droplet deposition.

note that the formation of instabilities is not very clear from Fig. 6.3 as the magnification is not sufficient. Therefore, we decided to observe these droplets more precisely under a microscope.

## 6.3 Microscopic observations

We observed the formation of instabilities using a microscope (Nikon Eclipse Ti2) with the magnification of x400 for a more detailed view and the magnification of x200 to see a larger area.

A detailed observation of the formation of the braids with a large magnification came, of course, at the expense of the size of the observed area. We therefore had to start our observations at some random point on the contact line with the hope that the instabilities would form at that point. Later in the run, we could move the point of observation to other regions of the droplet, e.g., in the central area, where the instabilities could also arise at a later stage of evaporation. Thereafter, we will treat "inner" and "outer" instabilities together, as the mechanism of their formation is similar. It will be shown in the following sections that the instabilities observed in our work arise from the motion of the contact line. The movement of a contact line is the key to the formation of both "inner" and "outer" instabilities.

### 6.3.1   Contact line

The initial contact line position, i.e., its equilibrium position soon after the drop deposition, is generally used as a point of reference for observations under the microscope since (i) the position is known at the beginning of the experiment and (ii) it also corresponds to the starting place of any eventual depinning. Regarding the formation of "inner" instabilities that can occur in any part of a droplet, we experienced difficulties in observing an area of the contact line already in motion that could develop an instability.

We analyzed the depinning of a contact line from videos showing the initial contact line position. Based on the patterns observed at the former initial contact line position after the droplet evaporation, we identified three classes of shapes that the contact line could form. These shapes could arise in different parts of the same droplet. Fig. 6.4 shows contact line pictures of three different droplets at the beginning (top line) and at the end (bottom line) of the experience. The pictures in this figure give typical examples of the three classes of shapes: *stable* (Fig. 6.4, left), *unstable* (Fig. 6.4, center), and *partially unstable* (Fig. 6.4, right). Again, it is important to emphasize that stable or partially unstable patterns obtained at a contact line position do not mean that the entire droplet would develop a pattern with the same characteristics. It only means that at this particular spot, the coffee-ring is stable or partially unstable. An unstable pattern is characterized by a slight increase in width and a significant and sudden motion of the contact line resulting in "broken" coffee-ring (Fig. 6.4, center). We will discuss the formation of unstable patterns in details later in this chapter. The partially unstable pattern appears when the contact line depins and starts moving, but pins again in usually several points shortly after depinning and stays there until the end of evaporation. In the case of a stable pattern, the contact line does not move, and accumulates particles (this is the classic coffee-stain effect [42]).

**Particle accumulation growth rate**

We measured the growth rate in width of the particles accumulating at the contact line during the first 10 min of a recording or until its depinning. To do so, we trace a line perpendicular to the contact line at a selected position, and we use the reslice option of ImageJ (Image $\longrightarrow$ Stacks $\longrightarrow$ Reslice) to generate a spatio-temporal diagram. The reslice option shows the pixels along the selected line (line width is 1 pixel) throughout the time, creating a spatio-temporal diagram. Fig. 6.5 schematically shows the work principle of the reslice function.

Fig. 6.6 presents an example of a spatio-temporal diagram created from the first 10 min of evaporation. This part of the droplet produces a stable pattern in the end. The horizontal direction of this image corresponds to time $t$ (in s). The vertical direction represents the coordinate $x$ (in µm) along the selected line perpendicular to the contact line. In Fig. 6.6, the first eight vertical lines (the white strip in the left part of the image) do not contain any information about the contact line. During this time, we were gently moving the stage holding the substrate to
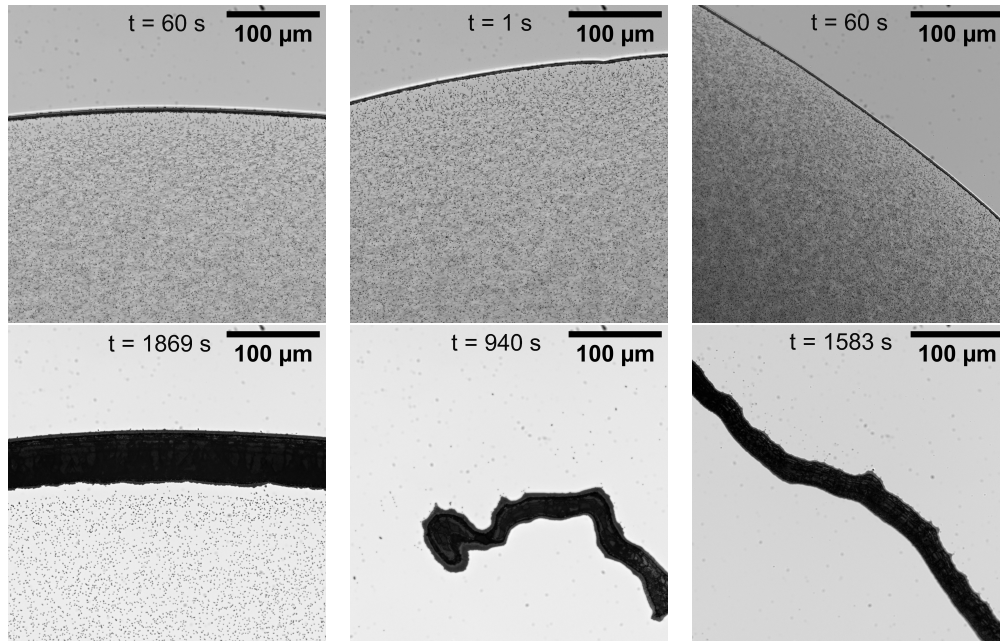
Figure 6.4: Beginning (top) and end (bottom) of formation of patterns obtained at the former contact line location: stable (left column), unstable (center) and partially unstable (right column).
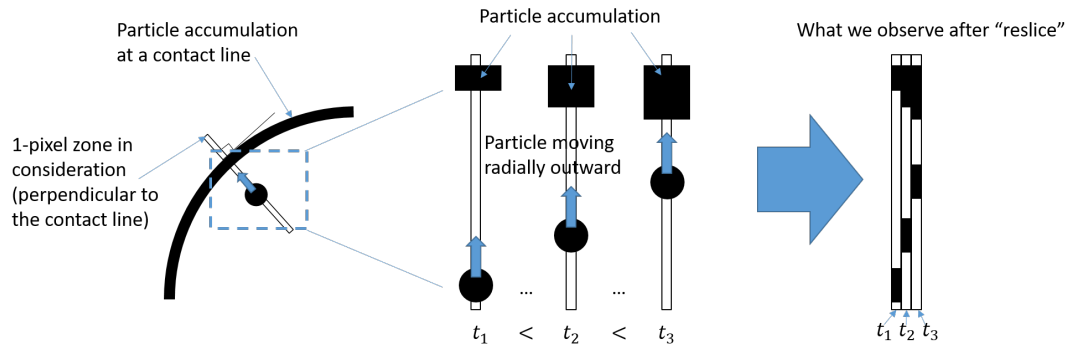


Figure 6.5: Work principle of the reslice function.

have the droplet edge under the microscope lens. Then, for about 40 s, we were searching for a focus, as the depth of field of the used microscope lens was very small. And although the substrate had no tilt (with an accuracy of less than 1°), even a small movement of a stage caused defocusing. Once the focus found, the stage position is fixed until depinning occurs (if present). In Fig. 6.6, we observe the thickening of the particle accumulation at the contact line over time. In particular, one can see that the width increases linearly with time and can be approximated by a linear function (red dotted line). In the figure, we can also observe some traces directed towards the contact line and having similar inclinations. These are particles moving radially outward following the capillary flow (at least until the break of symmetry at depinning). The explanation why these lines have an inclination is schematically given in Fig. 6.5. From the slopes of these lines in this spatio-temporal diagram, one can estimate the velocity of particles (about
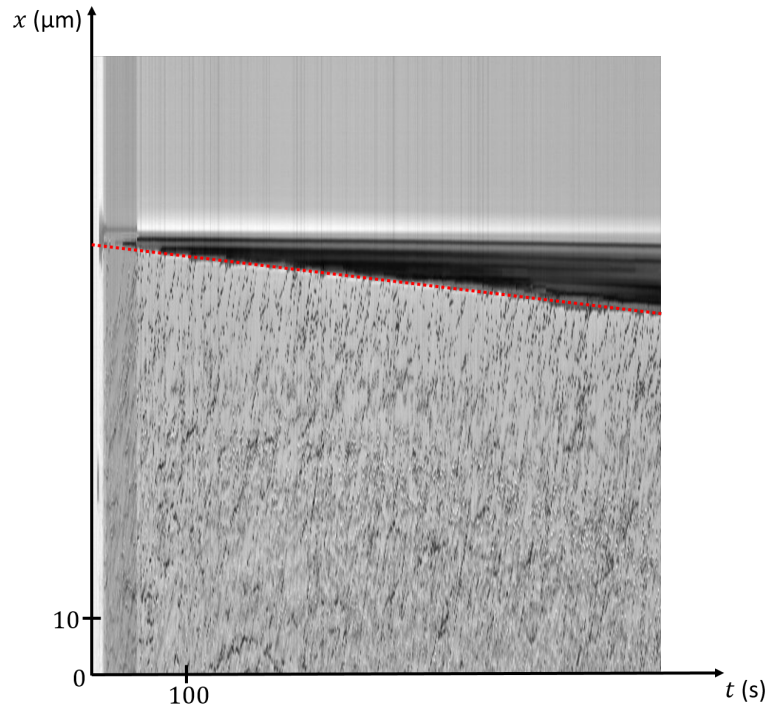
Figure 6.6: An example of a spatio-temporal diagram obtained for a droplet part producing a stable pattern in the end. The red dotted line shows the increase in the width of particles accumulated at the contact line, and its slope is the particle accumulation growth rate $q$.

3 µm/s) arriving at the contact line, which is consistent with the literature [119]. This estimation can only provide the order of magnitude but not accurate values, which would have required a spatio-temporal diagram constructed along the particle path. It is also to be noted that our particles are represented by either 3 or 6 pixels in diameter depending on the magnification, and what we see corresponds to the traces left by parts of different particles.

**Contact line depinning time**

In the majority of the videos, the droplet deposition time does not correspond to the start of the recording. Experimentally, two scenarios describe the beginning of the video recordings: the recording starts before the drop deposition, and the recording starts after the droplet has been deposited and the focus has been found. This yields a time difference of up to 2 min between the start of the recording and the drop deposition. To avoid the experimental error related to the delayed or advanced start of a video, the depinning time $t_d$ was calculated as the width of particles accumulated at the contact line before the depinning $w_d$ divided by the particle accumulation growth rate, $q$,:

$$t_d = \frac{w_d}{q} \tag{6.1}$$

**Results**

It appears that some correlation exists between the particle accumulation growth rate $q$ (i.e., "thickening" of the particle accumulation width per second) and the type of pattern observed at the initial contact line position. From Fig. 6.7, one can see that the stable patterns require a slow particle accumulation growth rate (below $0.022\,\mu\text{m/s}$). The unstable patterns are often (but not necessary) observed, when the particle accumulation growth is high (above $0.022\,\mu\text{m/s}$). The partially unstable patterns occur at both below $0.022\,\mu\text{m/s}$ and above $0.022\,\mu\text{m/s}$ particle accumulation growth rates. It is important to note that we analyze images from the bottom view, giving a 2D representation of the phenomena. This only provides information about the width of the particle accumulation at the contact line but not its height.
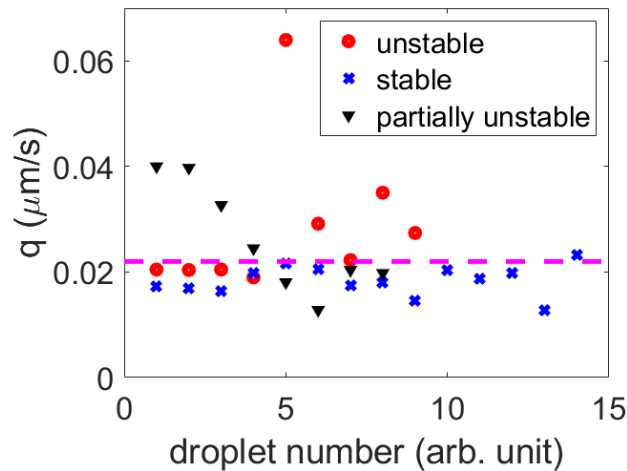


Figure 6.7: Growth rate of particles accumulated at the contact line for unstable (red dots), stable (blue crosses) and partially unstable (black diamonds) patterns observed at the initial contact line position.

We highlight in Fig. 6.8 this correlation through the plot of the depinning time $t_d$ and the width of particles accumulated at the contact line at depinning $w_d$. Naturally, the longer a contact line stays pinned, the thicker it will be (Fig. 6.8). The depinning of a contact line usually occurs between 1st and 8th minute after drop deposition. The coffee-ring width at depinning varies between $3\,\mu\text{m}$ and $14\,\mu\text{m}$. The particle accumulation growth rate lies between $0.019\,\mu\text{m/s}$ and $0.064\,\mu\text{m/s}$ for unstable patterns.

### 6.3.2  Formation of instabilities

**Structure of a contact line**

In addition to the 2D bottom view with the microscope, we performed measurements of the contact line height using Bruker 3D optical profiler to obtain the height of the deposit. Fig. 6.9 (top) presents an example of a 3D deposit image for an unstable pattern. Fig. 6.9 (bottom) shows the top 2D view of the same deposit and the variation of the deposit height along the red and blue profiles. We observe the peak of $6\,\mu\text{m}$ at the height curve of the red profile. This is the height of the coffee-ring. Along the blue profile, the coffee-ring heights are of $2\,\mu\text{m}$ and $3\,\mu\text{m}$. One also observes another two peaks of $4\,\mu\text{m}$ along the blue profile. These two peaks correspond to the
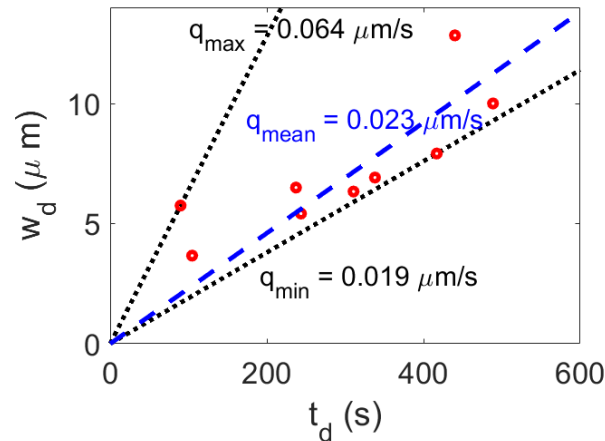
Figure 6.8: Particle accumulation width prior to the contact line motion as a function of the depinning time. The mean growth rate is calculated using least squares method.

height of the internal coffee-rings observed inside the deposit. One also notes that the coffee-ring is higher where the contact line did not depin (red arrows in Fig. 6.9 (top); next to the green triangle and green line in Fig. 6.9 (bottom left & right)). Meanwhile, the coffee-ring is the highest in the points where the internal "coffee-ring" merges with the external one (blue circles in Fig. 6.9 (top)).

The stable patterns tend to have the coffee-ring height between 5 µm and 8 µm, i.e., about 5 to 8 layers of 1 µm particles, while a significant variation in coffee-ring height (2 µm to 10 µm or 2 to 10 particle layers) is observed for unstable and partially unstable patterns.

The local coffee-ring structure was observed using a scanning electronic microscope (SEM), ZEISS Ultra55. The typical picture of the coffee-ring after complete evaporation (view from the top, perpendicular to the substrate) is presented in Fig. 6.10. One can see that (i) particles are densely packed, but there are still some void spaces, and (ii) there is no visible lateral deformation of particles when they are close to one another.

During the whole evaporation, particles arrive and pack themselves with more or less similar density (i.e., the fraction of the space filled with spheres). Indeed, the contact line appears to accumulate particles that become subsequently packed in a state of partial or complete immersion. This gradual accumulation allows the particles to "travel" along the contact line and rearrange themselves until they reach a very dense packing state where "travels" are not possible anymore. The motion of the contact line can either provoke (i) a deformation up to the rupture of this arrangement, (ii) move the entire structure all together, or (iii) just leave the particles in place and move beyond this structure and start again the particle collection.

**Depinning of the contact line & formation of instabilities**

With evaporation, when the loss of liquid becomes significant, the surface tension would tend to shrink the droplet, while the capillary force would rather keep the droplet attached to the particles at the contact line. If the surface tension wins in this trade, the contact line will begin to move.

The dynamics of the contact line motion are complex. On one hand, the capillary force tries to hold particles together through liquid bridges. On the other hand, several factors are contributing
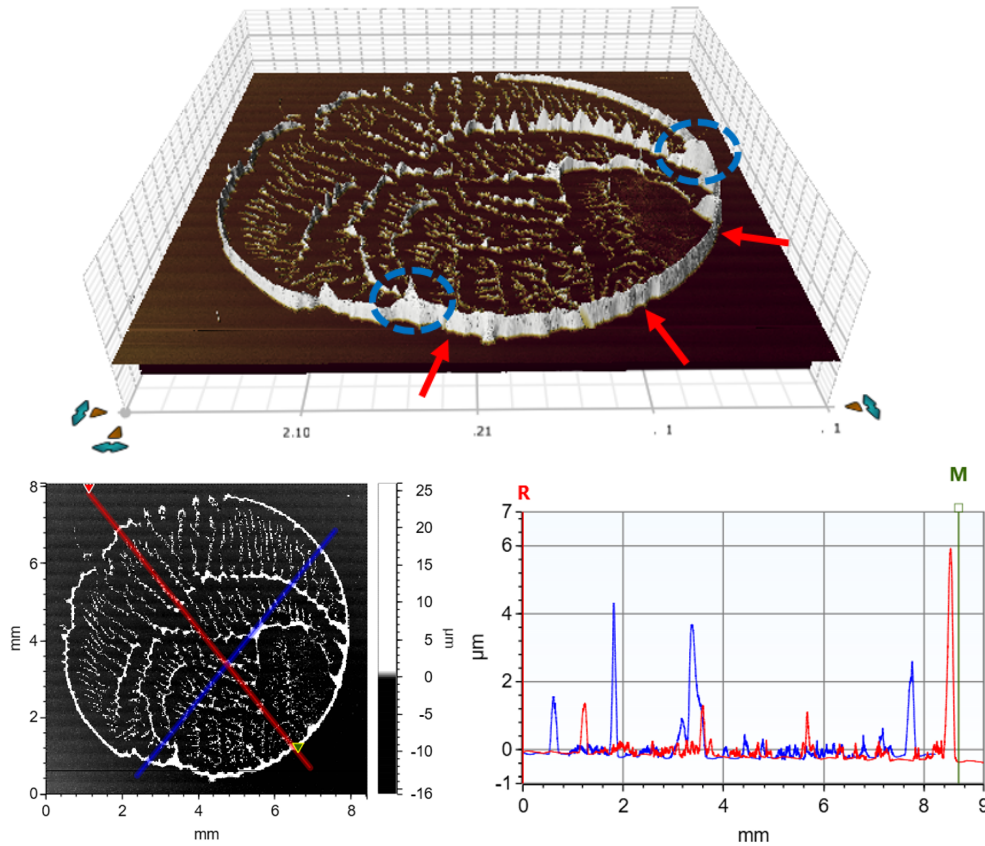
Figure 6.9: (top) 3D scan of the droplet. (bottom) 2D projection of the scan and the variation of height along the red and blue profiles.

to leaving particles behind. First, the geometrical constraints (i.e., packing density) imply that once the maximum packing density (which is equal to 0.74 for perfectly compacted same-size spheres and is about 0.63 for randomly compacted ones [178]) is achieved, the extra particles of the contact line must be left behind. Second, the friction between particles and a substrate (which includes particle-substrate adhesion) as well as surface heterogeneities met by the contact line on its way pull particles out of the contact line.

The observations show that a droplet typically depins on one side, while it remains pinned elsewhere until very late evaporation stage. When the contact line is in motion, its width increases faster as the contact line "rakes" particles on its way in addition to particles arriving at the contact line following radial flow. Based on our experimental observations, we have identified five different behaviors for a contact line in motion, which can be divided into two categories (Fig. 6.11) depending on whether the droplet shrinks with or without particles assembled on the contact line.

As it was mentioned above, if the droplet shrinks with particles assembled at its contact line, it always occurs within the first minutes of evaporation ($\sim 1-10\,\mathrm{min}$ for $10\,\mu\mathrm{L}$ droplet) for the present droplet volume of $10\,\mu\mathrm{L}$. This depinning was shown to partially correlate with the contact
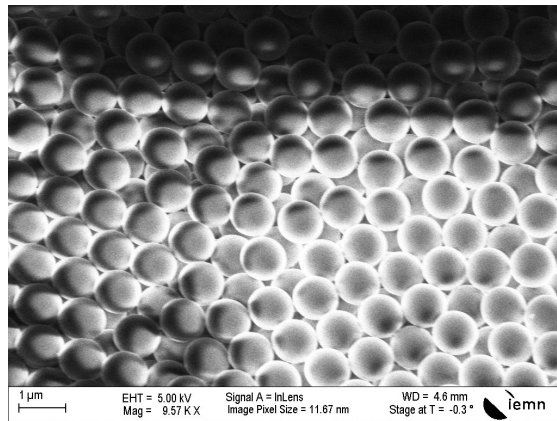
Figure 6.10: Packing of spheres on the top of a contact line. The packing is dense, but no particle deformation is observed.
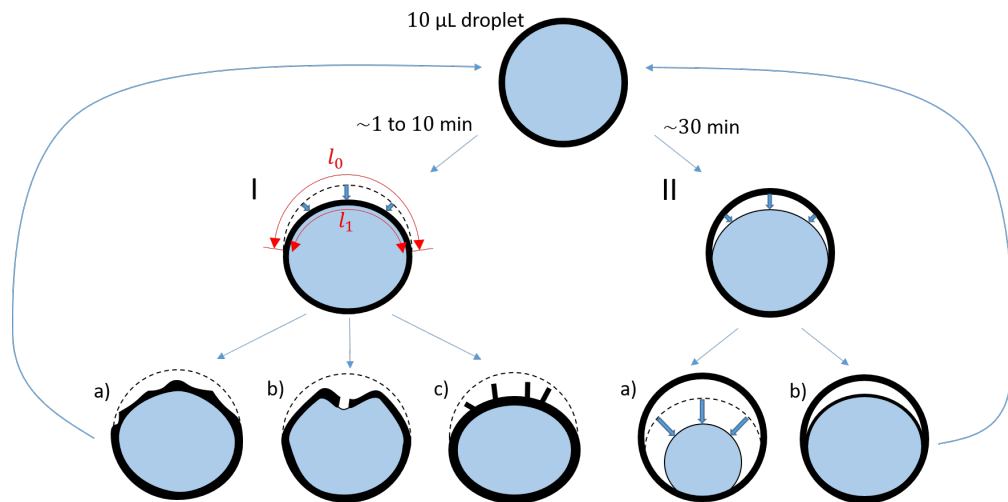


Figure 6.11: Possible behaviors of a contact line. The black solid lines represent particles, the blue area is water. The black dashed lines are the former positions of a contact line.

line growth rate $q$, and depending on whether this initial contact line depins or not, we classified the patterns in Fig. 6.4. As it was discussed above, the contact line first deforms and squeezes by compacting the particles. The particles assembled at the contact line and having an initial length $l_0$ (Fig. 6.11, I) move into a new position with a length $l_1 < l_0$ and same or more amount of particles because of newcomers. The periphery having the length $l_1$ is the minimum possible periphery that can accommodate all particles from the periphery $l_0$ and eventual newcomers. Once it is not possible for a contact line to squeeze anymore (packing density is close to its maximum), the contact line has three options.

First, the contact line can pin again and stay in this new position nearly until the end (Fig. 6.11, Ia). This is how partially unstable patterns (Fig. 6.4, right) are formed. In the late stage of evaporation, the droplet can depin again. In this case, it repeats the scheme presented in Fig. 6.11.

Second, the contact line only partially pins but breaks at one or several points (Fig. 6.11, Ib). Fig. 6.12 presents an example of this behavior. After some time of thickening, the contact line starts moving. It recedes and grows in width. The reason why the contact line is pinned at some points but not everywhere is not fully understood. Once a part of the contact line is pinned, "free" parts with less particles (red dashed circles in Fig. 6.12) arise. In these "free" parts, the contact line becomes thinner as it stretches faster than the particles replenish it. A decrease in the number of particles induce an acceleration of the contact line and the end of the process becomes really fast.
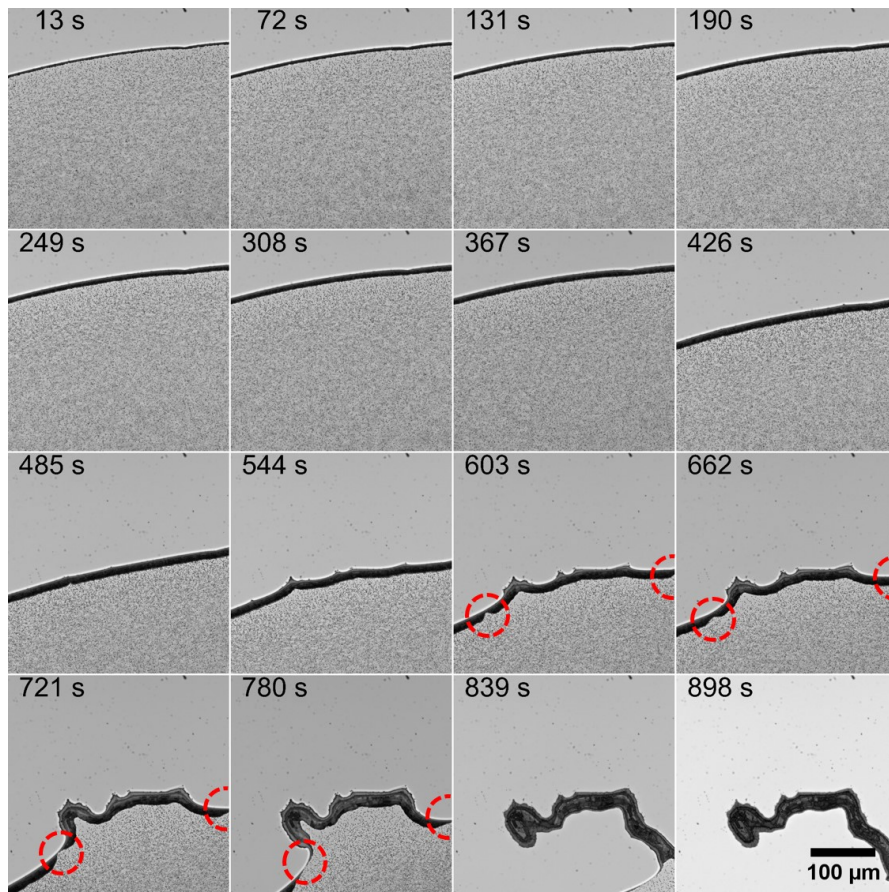


Figure 6.12: Formation of instability due to only partial pinning of contact line.

Third, the contact line can leave behind relatively large regular packets of particles ("braids") parallel to the contact line movement (Fig. 6.11 Ic; like those pictured in Fig. 6.1b). Since these "braids" are common in our unstable patterns, we will discuss them in detail in the next section.

In our observations, a droplet can shrink without particles assembled at the contact line (Fig. 6.11, II) only in the last stage of evaporation (after $\sim 30\,\text{min}$ of evaporation for $10\,\text{µL}$ droplet). In this case, there are two possible scenarios that can occur. In the first scenario, the droplet continues to shrink without collecting a large amount of particles at the contact line. Particles arriving at the contact line are generally quickly left behind. The contact line recedes so fast that the particles are unable to follow its speed. In this case, a coffee-ring with uniform deposition inside is observed after the droplet evaporation. In the second scenario, the particles arriving at a

contact line accumulate and slow down its movement. A new coffee-ring is formed. Starting from this point, the droplet behaves like an initial one (top droplet in Fig. 6.11). It can depin with (Fig. 6.11, I) or without (Fig. 6.11, II) particles collected at the contact line. For example, the droplet from Fig. 6.3 followed Fig. 6.11 IIb until a new coffee-ring was formed. Then, it followed Fig. 6.11 Ic regime to create the instabilities inside.

If, following one of the options from Fig. 6.11, the droplet was able to create a relatively even ring, it actually can switch to another option. For example, to create a pattern from Fig. 6.1b, the droplet first followed the option Fig. 6.11 Ic, and then Fig. 6.11 IIa.

### Braids & their properties

"Braids" are a frequent kind of instability both in the droplet center and at its edge. Often, several nearly parallel braids are formed at the same time. An example of braids is presented in Fig. 6.13.
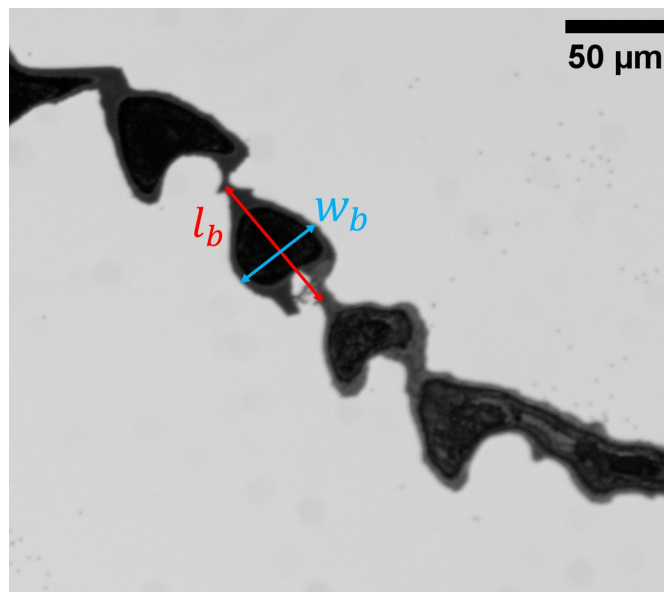


Figure 6.13: Braids instability. Each braid is characterized by its length $l_b$ and width $w_b$.

In Fig. 6.14, the step-by-step braids formation is shown. First, the pinning of a contact line occurs at some point (727 s). Second, the non-pinned part of the contact line continues to recede (730 s - 745 s). The contact line at the right and at the left of the pinning point deforms until it becomes parallel to the direction of motion of the contact line (748 s). While the contact line moves, it rakes particles in addition to those arriving at the contact line following outward capillary flow. However, this replenishment is not enough to maintain the contact line with the same width, and the contact line is depleted (blue and red arrows at 748 s). On the right side, however, the contact line still has some width (blue arrow), but on the left side, the contact line is completely depleted at some point (red arrow). After the complete depletion, the contact line ruptures, drives away from the braid, and "jumps" to a new position to form a new one (751 s). Then, a new braid is formed. The time between two "jumps" of the depleted side of the contact line is the time required to create a braid $t_b$. On the other non-depleted side of the contact line, there are still some particles, that will create a "neck" between two braids. It is seen in Fig. 6.14

that the neck is always closer to the right, which is a thicker side of the contact line.
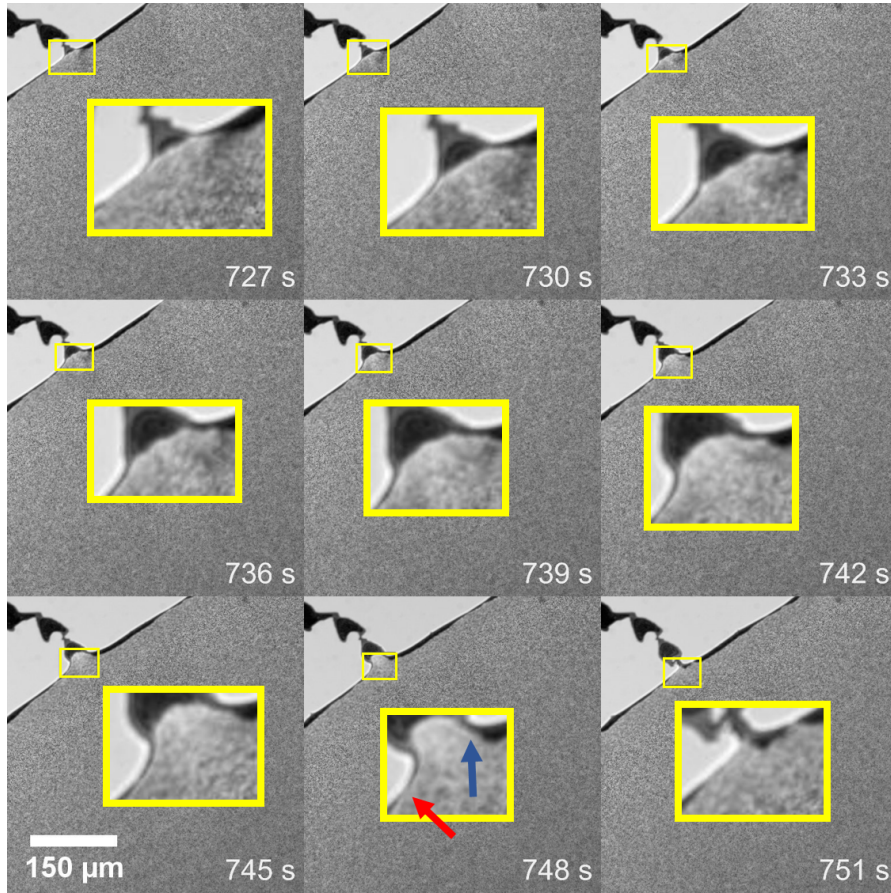


Figure 6.14: Formation of "braids". The insets are 4x zooms of the area in the vicinity of the forming braid.

We analyzed the time required to create a braid, $t_b$, as well as their lengths, $l_b$ (braid size along a direction perpendicular to the contact line, see Fig. 6.13), and their widths, $w_b$ (braid size along a direction tangential to the contact line, see Fig. 6.13). Fig. 6.15 (left) presents the time required to create a braid, $t_b$, as a function of braid length, $l_b$. We observe significant discrepancy for both, $t_b$ and $l_b$. The braid length $l_b$ varies from its minimum of about 20 µm to 101 µm. The braid length $l_b$ can be considered as the number of particles assembled in a radial direction (20 and 101 particles in our case). The time required to form a braid $t_b$ varies from 1 s to 105 s. Usually, the braids are formed faster in the late stage of droplet evaporation (after $\approx 27$ min of evaporation). There is no clear dependency of $t_b$ on $l_b$, but roughly, the more time it takes to form a braid, the longer it would be.

For each observed braid, we calculated the velocity of a braid formation, which is the ratio of the braid length to the time required to form it: $v_b = \frac{l_b}{t_b}$. Since the braid is formed right after the passage of the contact line, its formation velocity is close to the mean contact line velocity. Fig. 6.15 (right) presents the braid formation velocity as a function of the braid aspect ratio $\alpha_b$, which is calculated as $\alpha_b = \frac{l_b}{w_b}$.

Once again, the data are not 100% consistent, but on average it is likely to observe more elongated braids, if the formation velocity is faster and vice versa.
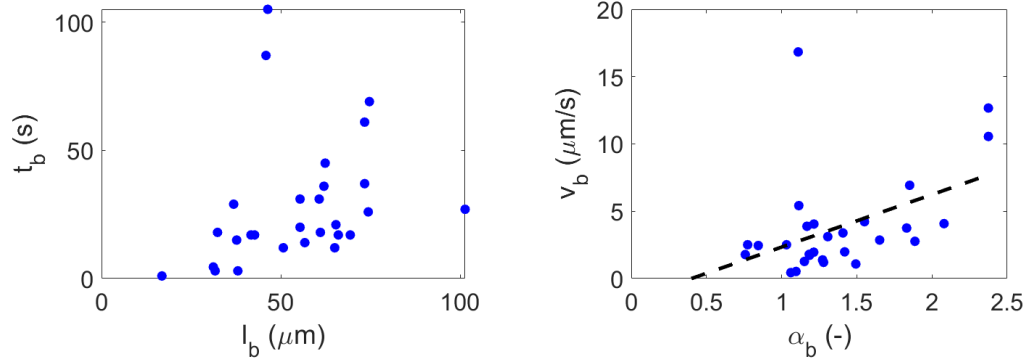


Figure 6.15: (left) Time required to create a braid as a function of braid length. (right) Braid formation velocity as a function of the braid aspect ratio. The black dashed line represents the fitting of the experimental data with the linear function.

## 6.4 Conclusion

In this chapter, we investigated the formation of various patterns. First, we showed that the early stage of evaporation (which is about 10 minutes for the considered droplet volume) is crucial for the contact line depinning and, consequently, for the resulting pattern. We measured the growth rate of particle accumulation at the contact line at the beginning of an evaporation process. We observed that the width of accumulated particles grows linearly with time. We also noticed that the formation of a stable pattern requires the contact line growth rate below $0.022\,\mu m/s$ in the first stage of evaporation of a $10\,\mu L$ droplet.

Second, we identified five scenarios of contact line behavior that we divided into two categories depending on whether the contact line depins with particles assembled on it (which usually occurs during the first stage of evaporation) or without them (which is typical for the late evaporation stage). Therefore, the affiliation to the category is decided by the contact line behavior at the early stage of evaporation.

Finally, we report qualitative observations of a unique pseudo-periodic pattern, named as braids, that was not previously reported. We analyzed the mechanism of their formation, the dependency of the time required to create a braid on its length, as well as the velocity of a braid formation as a function of its aspect ratio. We did not find a good correlation of data, but it is more likely to observe elongated braids with faster formation velocity and vice versa.

# Conclusion & perspectives

In the present work, we investigated the individual and collective behavior of microparticles. In the first part, we studied the detachment of immersed microparticles as well as the effect of a trapped air bubble on the particle detachment. The second part of this thesis was devoted to the collective dynamics of microspheres in an evaporating droplet that results in particle deposition onto a substrate.

We experimentally studied interactions of a hydrophobic particle with a hydrophilic substrate under different drying conditions using the adapted patch-clamp technique described in Chapter 2. The pipette tip is tailored to the particle size, which allows to manipulate microparticles of $1\,\mu$m in diameter or bigger. The maximum force that could be applied through the micropipette is of the order of $10\,$nN for $1\,\mu$m particles and $100\,$nN for $10\,\mu$m particles. This force depends on the pipette tip diameter, that should be smaller than the particle, and on the pump used. In our work, we used the pump that can produce the highest depression that we could find on the market, so no significant improvement for the maximum applied force is expected. The lower limit of the patch-clamp technique is of the order of $0.01\,$nN which was achieved when we manipulated hydrophilic particles placed on hydrophilic substrates (hydrophilic spores in Chapter 2 and hydrophilic particles in Chapter 3). One should be aware that the obtained results are on the limit of the patch-clamp technique and the measurements are less precise for the detachment force below $\approx 1\,$nN. The application range of the patch-clamp technique is similar to that of the AFM-based technique [108]. The patch-clamp technique has, however, an advantage for biological researchers, as it is a low-cost solution for single-particle detachment force measurements. Another benefit of the patch-clamp technique is the glass pipettes, that are hardly deformable compared to the cantilevers used in the AFM technique, whose deformation can raise an error in measurements. Besides, in the AFM technique, a proper attachment of a cell to the cantilever is a difficult task and can lead to inconsistent reading [117].

Based on the measured detachment forces, we calculated the contact radii using the widely used JKR [79] and DMT [49] models. These predicted contact radii were compared to those measured with SEM, but the difference between the predicted and experimental contact radii was found significant. Two possible explanations for this discrepancy were advanced. First, the deposition of particles onto the substrate was not gentle in our case, in contrast to the usually delicate deposition reported in the literature [17]. Indeed, we deposit a droplet containing particles onto a substrate and let it evaporate. At the very end stage of evaporation, a liquid bridge will form at the foot of any isolated particle, for which we would thereafter measure the detachment force. This bridge induces capillary and Laplace forces that act on the particle and can additionally deform it prior to our measurements. Second, it is possible that our particles are out of the application range of the considered models, especially if they have been exposed to plastic deformations during drying. Third, we speculate on the presence of an air bubble trapped under the particle when we pour liquid onto dry particles prior to patch-clamp measurements. The bubble trapped under the immersed particle can also, like liquid bridges, induce Laplace and

capillary forces on the particle, therefore yielding a measured detachment force that does not represent the sole particle-substrate interaction.

We found these trapped air bubbles particularly interesting and studied them in detail in Chapter 3. We developed a numerical model to estimate the bubble-induced force with respect to particle and substrate wetting characteristics. The model is quite simple and does not include advanced features such as non-equilibrium state or the imperfections of the surfaces. We found out that mostly the bubble facilitates the detachment of a hydrophilic particle, but can repel or retain a hydrophobic particle depending on the substrate wettability and the bubble volume. We also demonstrated that the entrapment of a bubble is unlikely, if both surfaces are hydrophilic. These results are of particular interest to, for instance, food industries where the contamination of surfaces of food processing lines by pathogens and spoilage bacteria is a major issue that still begs simple eco-friendly and low-cost solutions. Knowing that bacteria can present different degree of hydrophobicity [55], we can recommend to use only the equipment with hydrophilic walls having the contact angle below 50°. In this case, both hydrophobic and hydrophilic particles are repelled by any eventual trapped bubble. The simplicity of the presented model is an advantage and a disadvantage at the same time. The advantage is that it only requires the wettabilities of the involved surfaces and the surface tension of the liquid used, and so the model is very accessible to researchers and industry workers. However, many complexities were ignored. In the presented example of the food industry, the bacteria and spores are typically non-spherical objects sometimes with the mucous layer, and our estimations most likely do give not very accurate predictions for these microparticles and further associated research is needed.

In the second part of the thesis, we studied the collective dynamics of microspheres in an evaporating droplet and the obtained patterns. Since there is no common protocol in the literature, we focused on establishing our own and described it in Chapter 5. We then varied each step of the protocol to understand the sensitivity of patterns to changes in the protocol. We showed that the following protocol steps have the greatest influence on the obtained patterns: the washing of the suspension, the time between substrate cleaning and the start of the experiments, and the suspension age after washing. The drop deposition method and the mixing method of the suspension prior to drop deposition, on the other hand, did not seem to have any significant effect. We hope that our results would be helpful to the scientific community to understand how the experimental results obtained under different experimental conditions can be compared. Unfortunately, the relative humidity and the eventual air flows were out of our control throughout these experiments, and it would be interesting to repeat the same experiments in the glovebox with controlled temperature and humidity. These uncontrolled parameters could be the reason why we observed several types of patterns under the same experimental conditions.

We performed microscopic observations of various patterns arising from an evaporating droplet that we distinguished in Chapter 5. We identified five scenarios of contact line behavior resulting in different patterns depending on whether the contact line depins with or without particles assembled on it. We showed that the first stage (e.g., first 10 minutes in the case of 10 μL droplets) of evaporation is crucial for the contact line depinning and, consequently, for the resulting pattern. We measured the growth rate of particle accumulation at the contact line at the beginning of an evaporation process. It was found that the formation of the coffee-ring requires a low growth rate, while unstable and partially unstable patterns can form at any, low or high, growth rate. The particles are brought to the contact line by the capillary flow that develops inside the droplet in order to compensate the naturally higher evaporation rate at the droplet edge [42]. The low relative humidity would favor a faster evaporation of the droplet and, therefore, a faster liquid loss at the droplet edge, which in turn would require a stronger capillary flow. We assume that the latter would bring more particles per minute to the contact line. Therefore, we speculate that a low relative humidity would increase the percentage of the unstable patterns. A high relative

humidity, in contrast, would allow the formation of both, unstable and coffee-stain patterns. These results can be potentially interesting for the particle assembly solutions and for fundamental research, as we are still lacking a comprehensive understanding of the underlying mechanisms that decide the final pattern.

Among the developing patterns, one hitherto unreported in the literature has attracted our attention. We qualitatively made careful observations of the formation and the properties of this unique pseudo-periodic pattern, named as braids. The characteristic size of one braid was found to be of the order of ten particle diameters in length and width, and we typically observed at least three subsequent braids. We analyzed the mechanism of their formation, the dependency of time required to create a braid on its length, as well as the velocity of a braid formation as a function of its aspect ratio. However, no clear trend was found. This study needs to be completed with more experimental data and conditions (temperature, humidity, particle size, etc.) that could help to both understand the underlying physics and develop a theoretical model. The potential industrial application of braids is once again the study of particle assemblies.

# Appendix I

As we can observe, there is a wide data scattering in the measured detachment forces. To quantify this scattering, we introduce the probability density function. This function shows the change in the probability of detaching a particle from its substrate. The probability density function is, in fact, the derivative of the probability of detaching a particle. Consequently, the integral of this function from $-\infty$ to $x$ means the probability to detach a particle by applying a force $x$. In addition, it is to note that the area under the probability density function is equal to 1.

In our case, we define the probability density function as a derivative of the fitting curve (Eq.(2.3)) with the opposite sign. The change in sign comes from the fact that originally this curve was the probability of NOT removing a particle.

Fig. I1 (right) shows the probability density function for the 12 µm particles dried for 24 h at 40°C and 50°C. In this graph, we first observe a "plateau". Although the function seems to be constant, it is actually slowly rising during the whole interval. Then, we observe a peak (red curve) or very slight increase (blue curve) followed by a falling. Physically, the presence of "plateau" means that there is a chance of removing a particle even if a very small force is applied. As the probability of removing a particle is the integral of the probability density function, the former constantly increases with the growth of the applied force, i.e., along the "plateau". The presence of a peak indicates that in a specific force range, the probability of removing a particle rises very fast with the increase of the applied force. So, most of the detachment forces that we measure will belong to this interval. After the peak of the red curve or "plateau" of the blue curve, the probability density function falls down to 0, which means that no probability of removing a particle will be added if we continue to increase the applied force. For both curves, this maximum applied force is around 100 nN.

The presence or absence of a peak is translated by the slope of the fitting curve and, consequently, the scattering of experimental points in Fig. I1 (left). The central part (i.e., the zone between "almost 100% of attached particles" and "almost 0% of attached particles") of the red curve is more "vertical" with respect to the central part of the blue curve, and that is why we observe the peak. Moreover, one can see from Fig. I1 (left) that the red curve is very close to 0 at the applied force of about 80 nN. The probability density curve approaches 0 at the same applied force.

In the ideal case of particles that are all detached at the same applied force, we will have the Dirac delta function as the probability density distribution. So, the function, having a high peak, is closer to the ideal situation. In this regard, the 12 µm particles dried for 24 h at 40°C are more "ideal" (i.e., less scattered) than the same particles dried at 50°C. We can only suggest that this can arise due to the higher deformation experienced by the particles at the higher temperature.

Fig. I2 (right) shows the probability density distribution for 12 µm particles dried at 50°C for 1 h, 24 h, 48 h, or 72 h. We observe the peaks for all drying times except for 24 h. By comparing Fig. I2 (right) and Fig. I2 (left), one can note that the detachment curve for 24 h of drying is the
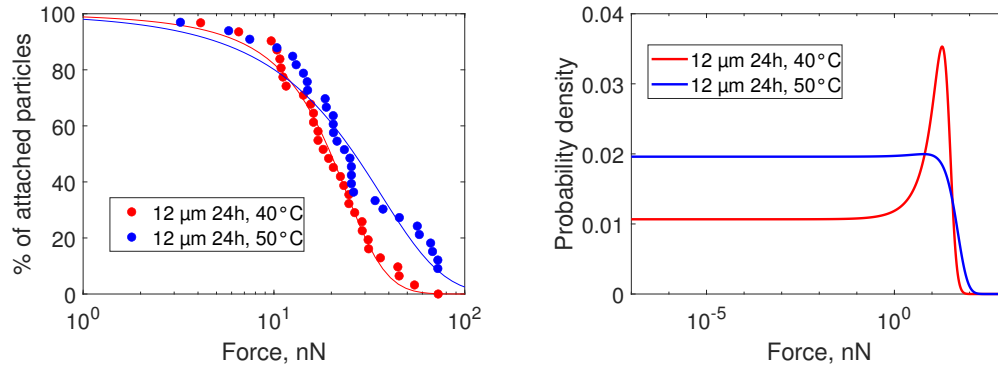
Figure I1: (left) Percentage of attached particles as a function of applied force for 12 µm particles dried for 24 h at different drying temperatures of 40°C and 50°C. (right) Probability density functions.

most scattered, which can explain the absence of a "peak" in this case. If we look closer at the probability density functions, we can note that 72 h case is the closest to the ideal situation, as it has the lowest "plateau" and a peak. The second closest to the ideal case is the 48 h, and the last one is the 1 h. From these results, we can speculate that the drying time tends to unify the contact between a particle and its substrate, reducing the gap between the measured detachment forces.
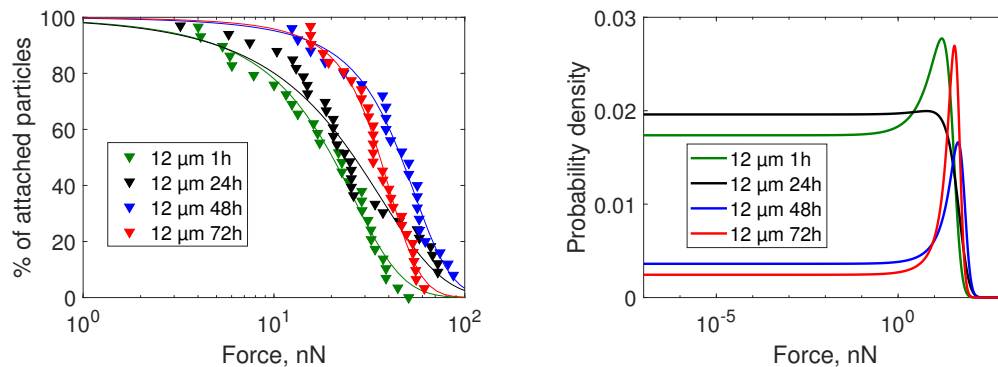


Figure I2: (left) Percentage of attached particles as a function of applied force for 12 µm particles dried at 50°C for 1 h, 24 h, 48 h or 72 h. (right) Probability density functions.

Fig. I3 (right) shows the probability density distribution for 1 µm, 6 µm and 12 µm particles dried at 50°C for 24 h. None of these graphs has a significant peak, which means that the slopes of all curves are subtle. We cannot state with certainty why this happens, but from the previous discussion about the drying times, we can suggest that 24 h was not enough to unify a particle-substrate contact.
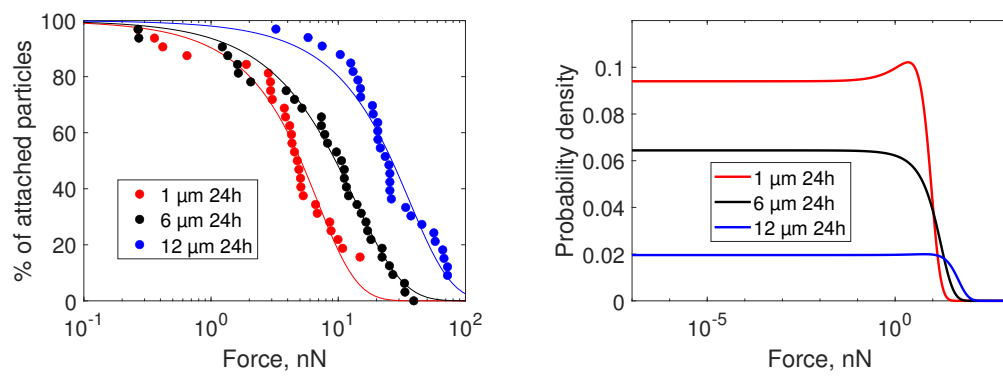
Figure I3: (left) Percentage of attached particles as a function of applied force for $1\,\mu m$, $6\,\mu m$, $12\,\mu m$ particles dried at $50\,°C$ for $24\,h$. (right) Probability density functions.

# Appendix II

To obtain the probability density function for the graphs from Chapter 3, we take a derivative of the fitting curve (Eq.(3.18)). For a more detailed explanation of the application of probability density distribution to our experiments, please refer to Appendix I.

Fig. II1 (right) shows the probability density distribution for hydrophobic particles placed on a hydrophobic substrate for different degassing times. None of these curves has a peak, which means that there is wide data scattering no matter the degassing time. In terms of bubbles, we can suggest that if there were bubbles of different volumes trapped under the particles (which is highly likely when both surfaces are hydrophobic), they would not all disappear nor become identical to each other (by losing different substance quantities) after degassing.
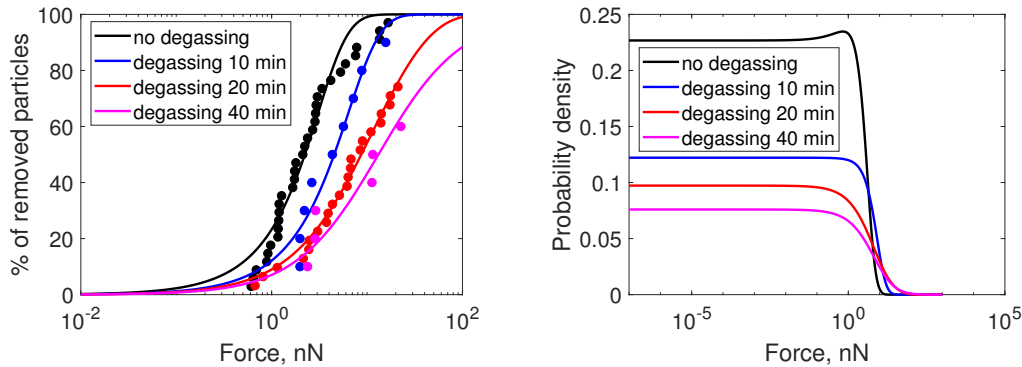


Figure II1: Hydrophobic particles placed on a hydrophobic substrate: (left) experimental curves and (right) probability density functions.

Fig. II2 (right) shows the probability density distribution for hydrophobic particles placed on a hydrophilic substrate. We distinguish peaks for all degassing times. If we suppose that bubbles were present under the particles, the presence of peaks would mean that the bubbles were relatively identical to each other before degassing and remained identical to each other regardless of the changes in the degassing time.

The probability density distribution for hydrophilic particles placed on a hydrophobic substrate is shown in Fig. II3 (right). We observe peaks after $20\,\mathrm{min}$ and $40\,\mathrm{min}$ of degassing, while no degassing and $10\,\mathrm{min}$ of degassing do not have any peaks. We can conclude that the degassing tends to unify the detachment force, i.e., unify (or even make completely disappear) the bubbles in this case.

Finally, the probability density distribution for hydrophilic particles placed on a hydrophilic substrate is presented in Fig. II4 (right). Although the given curves show a high data scattering
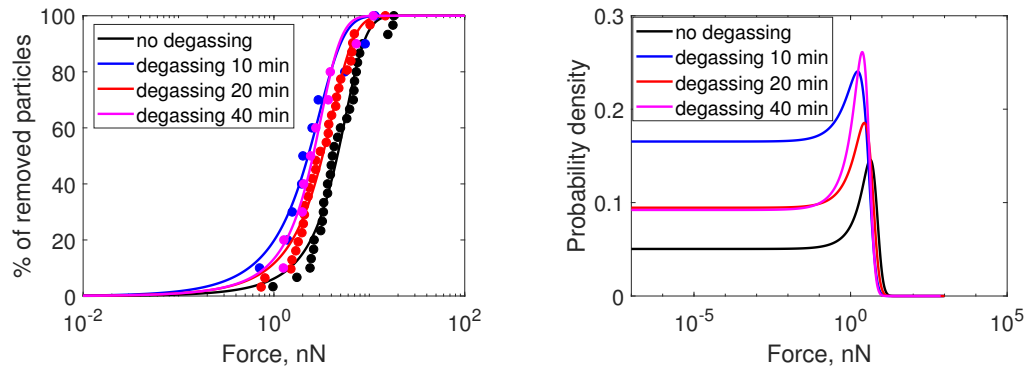
Figure II2: Hydrophobic particles placed on a hydrophilic substrate: (left) experimental curves and (right) probability density functions.
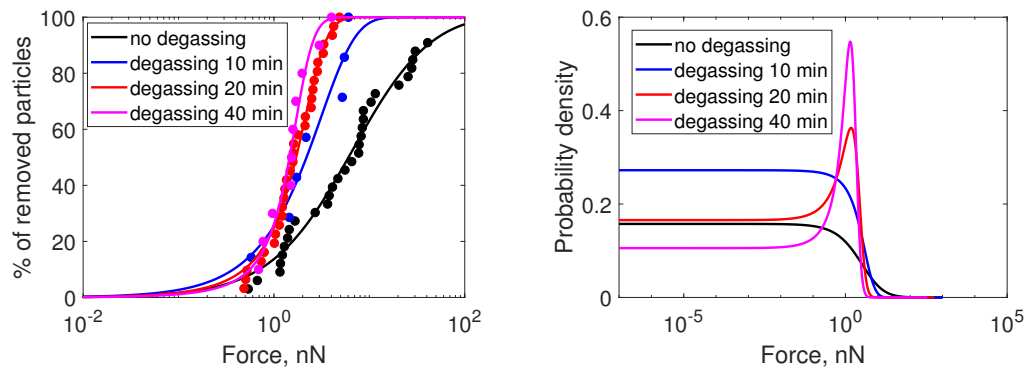


Figure II3: Hydrophilic particles placed on a hydrophobic substrate: (left) experimental curves and (right) probability density functions.

regardless of the degassing time, we refrain from any conclusions in this case, as the detachment force measurements are at the limit of the patch-clamp technique.

From the presented graphs, we can conclude that the degassing time can either unify the bubbles (if the latter are present) or not contribute to their syncronization. Moreover, the least data scattering (i.e., the most uniform bubbles) is observed for two surfaces having different wettabilities after degassing. In contrast, when both surfaces are hydrophobic, the data is highly scattered for any degassing time.
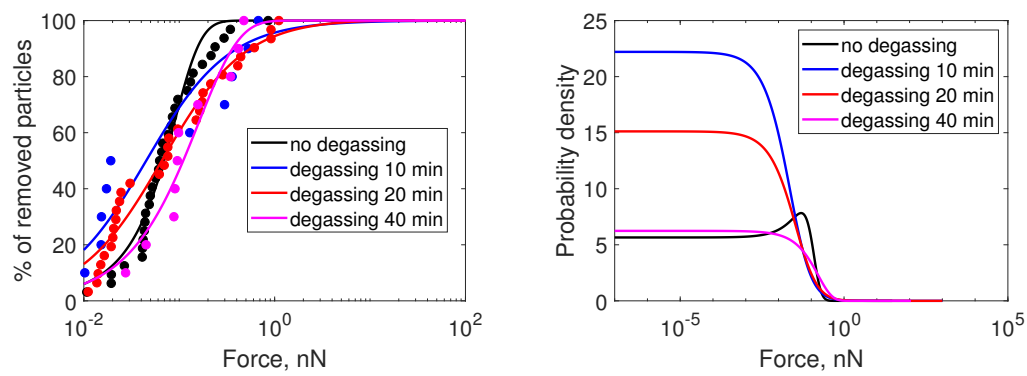
Figure II4: Hydrophilic particles placed on a hydrophilic substrate: (left) experimental curves and (right) probability density functions.

# Bibliography

[1] D. M. Anderson and S. H. Davis. The spreading of volatile liquid droplets on heated surfaces. Physics of Fluids, 7(2):248–265, February 1995.

[2] Manos Anyfantakis, Zheng Geng, Mathieu Morel, Sergii Rudiuk, and Damien Baigl. Modulation of the Coffee-Ring Effect in Particle/Surfactant Mixtures: the Importance of Particle–Interface Interactions. Langmuir, 31(14):4113–4120, April 2015.

[3] Surachet Aramrak, Markus Flury, and James B. Harsh. Detachment of Deposited Colloids by Advancing and Receding Air–Water Interfaces. Langmuir, 27(16):9985–9993, August 2011.

[4] Alexandros Askounis, Khellil Sefiane, Vasileios Koutsos, and Martin E.R. Shanahan. Effect of particle geometry on triple line motion of nano-fluid drops and deposit nano-structuring. Advances in Colloid and Interface Science, 222:44–57, August 2015.

[5] Kellar Autumn, Metin Sitti, Yiching A Liang, Anne M Peattie, Wendy R Hansen, Simon Sponberg, Thomas W Kenny, Ronald Fearing, Jacob N Israelachvili, and Robert J Full. Evidence for van der Waals adhesion in gecko setae. Proceedings of the National Academy of Sciences, page 5, 2002.

[6] Matthew J. Baker, Shawn R. Hussain, Lila Lovergne, Valérie Untereiner, Caryn Hughes, Roman A. Lukaszewski, Gérard Thiéfin, and Ganesh D. Sockalingum. Developing and understanding biofluid vibrational spectroscopy: a critical review. Chemical Society Reviews, 45(7):1803–1818, 2016.

[7] Margherita Basso, Michele Simonato, Riccardo Furlanetto, and Luigi De Nardo. Study of chemical environments for washing and descaling of food processing appliances: An insight in commercial cleaning products. Journal of Industrial and Engineering Chemistry, 53:23–36, September 2017.

[8] G. K. Batchelor. Sedimentation in a dilute dispersion of spheres. Journal of Fluid Mechanics, 52(2):245–268, 1972. Edition: 2006/03/29 Publisher: Cambridge University Press.

[9] J. P. Bearinger, D. G. Castner, S. L. Golledge, A. Rezania, S. Hubchak, and K. E. Healy. P(AAm- *co* -EG) Interpenetrating Polymer Networks Grafted to Oxide Surfaces: Surface Characterization, Protein Adsorption, and Cell Detachment Studies. Langmuir, 13(19):5175–5183, September 1997.

[10] M. Berry. The molecular mechanism of surface tension. Physics Education, 6, 1979.

[11] L Besra and M Liu. A review on fundamentals and applications of electrophoretic deposition (EPD). Progress in Materials Science, 52(1):1–61, January 2007.

[12] K. Bewilogua, G. Bräuer, A. Dietz, J. Gäbler, G. Goch, B. Karpuschewski, and B. Szyszka. Surface technology for automotive engineering. <u>CIRP Annals</u>, 58(2):608–627, 2009.

[13] Rajneesh Bhardwaj, Xiaohua Fang, Ponisseril Somasundaran, and Daniel Attinger. Self-Assembly of Colloidal Particles from Evaporating Droplets: Role of DLVO Interactions and Proposition of a Phase Diagram. <u>Langmuir</u>, 26(11):7833–7842, June 2010.

[14] Terry P. Bigioni, Xiao-Min Lin, Toan T. Nguyen, Eric I. Corwin, Thomas A. Witten, and Heinrich M. Jaeger. Kinetically driven self assembly of highly ordered nanoparticle monolayers. <u>Nature Materials</u>, 5(4):265–270, April 2006.

[15] Feodor M. Borodich. The Hertz-Type and Adhesive Contact Problems for Depth-Sensing Indentation. In <u>Advances in Applied Mechanics</u>, volume 47, pages 225–366. Elsevier, 2014.

[16] W. Bou Zeid and D. Brutin. Influence of relative humidity on spreading, pattern formation and adhesion of a drying drop of whole blood. <u>Colloids and Surfaces A: Physicochemical and Engineering Aspects</u>, 430:1–7, August 2013.

[17] R. C. Bowen, L. P. Demejo, and D. S. Rimai. A Method of Determining the Contact Area Between a Particle and Substrate Using Scanning Electron Microscopy. <u>The Journal of Adhesion</u>, 51(1-4):191–199, September 1995.

[18] R. Allen Bowling. An Analysis of Particle Adhesion on Semiconductor Surfaces. <u>Journal of The Electrochemical Society</u>, 132(9):2208–2214, September 1985.

[19] D. Brutin. Influence of relative humidity and nano-particle concentration on pattern formation and evaporation rate of pinned drying drops of nanofluids. <u>Colloids and Surfaces A: Physicochemical and Engineering Aspects</u>, 429:112–120, July 2013.

[20] D. Brutin, B. Sobac, B. Loquet, and J. Sampol. Pattern formation in drying drops of blood. <u>Journal of Fluid Mechanics</u>, 667:85–95, January 2011.

[21] Stefan Yoshi Buhmann and Dirk-Gunnar Welsch. Dispersion forces in macroscopic quantum electrodynamics. <u>Progress in Quantum Electronics</u>, 31(2):51–130, 2007. arXiv:quant-ph/0608118.

[22] A. B. D. Cassie and S. Baxter. Wettability of porous surfaces. <u>Transactions of the Faraday Society</u>, 40:546, 1944.

[23] Mickaël Castelain, Paul G. Rouxhet, Frédéric Pignon, Albert Magnin, and Jean-Michel Piau. Single-cell adhesion probed *in-situ* using optical tweezers: A case study with *Saccharomyces cerevisiae*. <u>Journal of Applied Physics</u>, 111(11):114701, June 2012.

[24] A. M. Cazabat, F. Heslot, S. M. Troian, and P. Carles. Fingering instability of thin spreading films driven by temperature gradients. <u>Nature</u>, 346(6287):824–826, August 1990.

[25] M.W.L. Chee, T.V. Ahuja, R.K. Bhagat, N. Taesopapong, S.A. Wan, R.L. Wigmore, and D.I. Wilson. Impinging jet cleaning of tank walls: Effect of jet length, wall curvature and related phenomena. <u>Food and Bioproducts Processing</u>, 113:142–153, January 2019.

[26] Viral H. Chhasatia, Abhijit S. Joshi, and Ying Sun. Effect of relative humidity on contact angle and particle deposition morphology of an evaporating colloidal drop. <u>Applied Physics Letters</u>, 97(23):231909, December 2010.

[27] Yongjoon Choi, Jeongin Han, and Chongyoup Kim. Pattern formation in drying of particle-laden sessile drops of polymer solutions on solid substrates. Korean Journal of Chemical Engineering, 28(11):2130–2136, November 2011.

[28] Chan Hee Chon, Sokwon Paik, Joseph B. Tipton, and Kenneth D. Kihm. Effect of Nanoparticle Sizes and Number Densities on the Evaporation and Dryout Characteristics for Strongly Pinned Nanofluid Droplets. Langmuir, 23(6):2953–2960, March 2007.

[29] Kevin V. Christ and Kevin T. Turner. Methods to Measure the Strength of Cell Adhesion to Substrates. Journal of Adhesion Science and Technology, 24(13-14):2027–2058, January 2010.

[30] Douglas W. Cooper. Particulate Contamination and Microelectronics Manufacturing: An Introduction. Aerosol Science and Technology, 5(3):287–299, January 1986.

[31] M. Cristina Dejesus, Jason A. Morgan, and D. S. Rimai. Time-Dependence of the Adhesion of Micrometer-Size Particles to Substrates: Correlation with Postdeposition Particle Rotation. The Journal of Adhesion, 82(7):697–712, June 2006.

[32] A. Crivoi and Fei Duan. Evaporation-Induced Branched Structures from Sessile Nanofluid Droplets. The Journal of Physical Chemistry C, 117(15):7835–7843, April 2013.

[33] Mina Dadjoo, Nasrin Etesami, and Mohsen Nasr Esfahany. Influence of orientation and roughness of heater surface on critical heat flux and pool boiling heat transfer coefficient of nanofluid. Applied Thermal Engineering, 124:353–361, September 2017.

[34] Heni Dallagi, Christine Faille, Laurent Bouvier, Maureen Deleplace, Thomas Dubois, Fethi Aloui, and Thierry Benezech. Wet foam flow: A suitable method for improving surface hygiene in the food industry. Journal of Food Engineering, 322:110976, June 2022.

[35] Zoey S Davidson. Deposition and drying dynamics of liquid crystal droplets. Nature Communications, page 7, 2017.

[36] S H Davis. Thermocapillary Instabilities. Annual Review of Fluid Mechanics, 19(1):403–435, January 1987.

[37] Raf De Dier, Wouter Sempels, Johan Hofkens, and Jan Vermant. Thermocapillary Fingering in Surfactant-Laden Water Droplets. Langmuir, 30(44):13338–13344, November 2014.

[38] P. G. de Gennes. Wetting: statics and dynamics. Reviews of Modern Physics, 57(3):827–863, July 1985.

[39] D.P. Debrincat, C.B. Solnordal, and J.S.J. Van Deventer. Characterisation of inter-particle forces within agglomerated metallurgical powders. Powder Technology, 182(3):388–397, March 2008.

[40] E. L. Decker and S. Garoff. Contact Line Structure and Dynamics on Surfaces with Contact Angle Hysteresis. Langmuir, 13(23):6321–6332, November 1997.

[41] Robert D. Deegan. Pattern formation in drying drops. Physical Review E, 61(1):475–485, January 2000.

[42] Robert D. Deegan, Olgica Bakajin, Todd F. Dupont, Greb Huber, Sidney R. Nagel, and Thomas A. Witten. Capillary flow as the cause of ring stains from dried liquid drops. Nature, 389(6653):827–829, October 1997.

[43] Robert D. Deegan, Olgica Bakajin, Todd F. Dupont, Greg Huber, Sidney R. Nagel, and Thomas A. Witten. Contact line deposits in an evaporating drop. Physical Review E, 62(1):756–765, July 2000.

[44] M Cristina Dejesus, Jason A Morgan, and D S Rimai. Time-Dependence of the Adhesion of Micrometer-Size Particles to Substrates: Correlation with Postdep. The Journal of Adhesion, page 17, 2006.

[45] M. Cristina Dejesus, Donald S. Rimai, and David J. Quesnel. Effect of Young's Modulus on the Detachment Force of 7 μm Particles. Langmuir, 22(2):729–735, January 2006.

[46] L.P. Demejo, D.S. Rimai, and R.C. Bowen. Adhesion-induced deformations of polyurethane substrates in contact with spherical glass particles: the effect of particle size on the radius of contact. Journal of Adhesion Science and Technology, 5(11):959–972, January 1991.

[47] B Derjaguin and L Landau. Theory of the stability of strongly charged lyophobic sols and of the adhesion of strongly charged particles in solutions of electrolytes. Progress in Surface Science, 43(1-4):30–59, May 1993.

[48] B. V. Derjaguin, V. M. Muller, and Yu P. Toporov. On the role of molecular forces in contact deformations (critical remarks concerning Dr. Tabor's report). Journal of Colloid and Interface Science, 67(2):378–379, 1978.

[49] B.V Derjaguin, V.M Muller, and Yu.P Toporov. Effect of contact deformations on the adhesion of particles. Journal of Colloid and Interface Science, 53(2):314–326, November 1975.

[50] Yanjun Ding, Jiang Ling, Yuchun Qiao, Zhengjian Li, Zongzhao Sun, Jifeng Cai, Yadong Guo, and Hua Wang. A high-throughput fluorimetric microarray with enhanced fluorescence and suppressed "coffee-ring" effects for the detection of calcium ions in blood. Scientific Reports, 6(1):38602, December 2016.

[51] Weerapun Duangthongsuk and Somchai Wongwises. Measurement of temperature-dependent thermal conductivity and viscosity of TiO2-water nanofluids. Experimental Thermal and Fluid Science, 33(4):706–714, April 2009.

[52] Athanase M. Dupré and Paul Dupré. Théorie mécanique de la chaleur. Gauthier-Villars, 1869.

[53] B.D. Edmonstone, O.K. Matar, and R.V. Craster. Surfactant-induced fingering phenomena in thin film flow down an inclined plane. Physica D: Nonlinear Phenomena, 209(1-4):62–79, September 2005.

[54] H. Yildirim Erbil. The debate on the dependence of apparent contact angles on drop contact area or three-phase contact line: A review. Surface Science Reports, 69(4):325–365, December 2014.

[55] Christine Faille, Celine Jullien, Francoise Fontaine, Marie-Noelle Bellon-Fontaine, Christian Slomianny, and Thierry Benezech. Adhesion of *Bacillus* spores and *Escherichia coli* cells to inert surfaces: role of surface hydrophobicity. Canadian Journal of Microbiology, 48(8):728–738, August 2002.

[56] Christine Faille, Christelle Lemy, Audrey Allion-Maurer, and Farzam Zoueshtiagh. Evaluation of the hydrophobic properties of latex microspheres and Bacillus spores. Influence of the particle size on the data obtained by the MATH method (microbial adhesion to hydrocarbons). Colloids and Surfaces B: Biointerfaces, 182:110398, October 2019.

[57] Xin Feng. Investigation on JKR surface energy of high-humidity maize grains. Powder Technology, page 14, 2021.

[58] Robert Fletcher, Nathanael Briggs, Erin Ferguson, and Greg Gillen. Measurements of Air Jet Removal Efficiencies of Spherical Particles from Cloth and Planar Surfaces. Aerosol Science and Technology, 42(12):1052–1061, October 2008.

[59] K. N. G. Fuller and D. Tabor. The Effect of Surface Roughness on the Adhesion of Elastic Solids. Proceedings of the Royal Society of London. Series A, Mathematical and Physical Sciences, 345(1642):327–342, 1975.

[60] Andrés J. García, Paul Ducheyne, and David Boettiger. Quantification of cell adhesion using a spinning disc device and application to surface-reactive materials. Biomaterials, 18(16):1091–1098, August 1997.

[61] Aaron S. Goldstein and Paul A. DiMilla. Application of fluid mechanic and kinetic models to characterize mammalian cell detachment in a radial-flow chamber. Biotechnology and Bioengineering, 55(4):616–629, August 1997.

[62] Patrick W Gordon, Anju D M Brooker, Y M John Chew, D Ian Wilson, and David W York. A scanning fluid dynamic gauging technique for probing surface layers. Measurement Science and Technology, 21(8):085103, August 2010.

[63] A. Grandillo and S. Tatianchenko. Optimization of Clean-In-Place Sanitation Systems for McCain Supply Chain. Technical report, McGill University, 2020.

[64] O. P. Hamill, A. Marty, E. Neher, B. Sakmann, and F. J. Sigworth. Improved patch-clamp techniques for high-resolution current recording from cells and cell-free membrane patches. Pflügers Archiv - European Journal of Physiology, 391(2):85–100, August 1981.

[65] Dorian Hanaor, Marco Michelazzi, Cristina Leonelli, and Charles C. Sorrell. The effects of carboxylic acids on the aqueous dispersion and electrophoretic deposition of ZrO2. Journal of the European Ceramic Society, 32(1):235–244, January 2012.

[66] H. Hertz. On the Contact of Rigid Elastic Solids and on Hardness. Macmillan and Co., New York., 1882.

[67] Poornima G. Hiremath, Rajashekhara S, Prakash Binnal, and Thomas Theodore. Chapter 9 - Fluoride Contamination in Underground Water and Its Treatment. In Pardeep Singh, Chaudhery Mustansar Hussain, and Sanchayita Rajkhowa, editors, Management of Contaminants of Emerging Concern (CEC) in Environment, pages 249–280. Elsevier, 2021.

[68] T. A. Horbett, J. J. Waldburger, B. D. Ratner, and A. S. Hoffman. Cell adhesion to a series of hydrophili-hydrophobic copolymers studies with a spinning disc apparatus. Journal of Biomedical Materials Research, 22(5):383–404, May 1988.

[69] Hua Hu and Ronald G. Larson. Analysis of the Effects of Marangoni Stresses on the Microflow in an Evaporating Sessile Droplet. Langmuir, 21(9):3972–3980, April 2005.

[70] Hua Hu and Ronald G. Larson. Analysis of the Microfluid Flow in an Evaporating Sessile Droplet. Langmuir, 21(9):3963–3971, April 2005.

[71] Hua Hu and Ronald G. Larson. Marangoni Effect Reverses Coffee-Ring Depositions. The Journal of Physical Chemistry B, 110(14):7090–7094, April 2006.

[72] Yin-Chun Hu, Qiong Zhou, Hai-Mu Ye, Yu-Feng Wang, and Li-Shan Cui. Peculiar surface profile of poly(ethylene oxide) film with ring-like nucleation distribution induced by Marangoni flow effect. Colloids and Surfaces A: Physicochemical and Engineering Aspects, 428:39–46, July 2013.

[73] Herbert E. Huppert. Flow and instability of a viscous current down a slope. Nature, 300(5891):427–429, December 1982.

[74] Mohammad J Inanlu, Behrooz Shojaan, Jafar Farhadi, and Vahid Bazargan. Effect of Particle Concentration on Surfactant-Induced Alteration of the Contact Line Deposition in Evaporating Sessile Droplets. Langmuir, page 9, 2021.

[75] R. Iqbal, Atsushi Matsumoto, A. Sudeepthi, Amy Q. Shen, and A. K. Sen. Substrate stiffness affects particle distribution pattern in a drying suspension droplet. Applied Physics Letters, 114(25):253701, June 2019.

[76] Jacob N. Israelachvili and Michelle L. Gee. Contact angles on chemically heterogeneous surfaces. Langmuir, 5(1):288–289, January 1989.

[77] H. Jeong, J. van Tiem, Y.B. Gianchandani, and J. Park. Nano-Particle Separation Using Marangoni Flow in Evaporating Droplets. In 2014 Solid-State, Actuators, and Microsystems Workshop Technical Digest, pages 223–226, Hilton Head, South Carolina, USA, May 2014. Transducer Research Foundation.

[78] K.L. Johnson, K. Kendall, and A.D. Roberts. Surface energy and the contact of elastic solids. Proceedings of the Royal Society of London, page 13, 1971.

[79] Rulon E Johnson, Robert H Dettre, and Dale A Brandreth. Dynamic contact angles and contact angle hysteresis. Journal of Colloid and Interface Science, 62(2):205–212, November 1977.

[80] Mustafa A. Kadhim, Nikil Kapur, Jonathan L. Summers, and Harvey Thompson. Experimental and Theoretical Investigation of Droplet Evaporation on Heated Hydrophilic and Hydrophobic Surfaces. Langmuir, 35(19):6256–6266, May 2019.

[81] Kwan Hyoung Kang, Hee Chang Lim, Hee Woong Lee, and Sang Joon Lee. Evaporation-induced saline Rayleigh convection inside a colloidal droplet. Physics of Fluids, 25(4):042001, April 2013.

[82] M Karabulut, E Melnik, R Stefan, G.K Marasinghe, C.S Ray, C.R Kurkjian, and D.E Day. Mechanical and structural properties of phosphate glasses. Journal of Non-Crystalline Solids, 288(1-3):8–17, August 2001.

[83] Takeo Kawase, Henning Sirringhaus, Richard H Friend, and Tatsuya Shimoda. Inkjet Printed Via-Hole Interconnections and Resistors for All-Polymer Transistor Circuits. Advanced Materials, page 5, 2001.

[84] Anthony A. Killeen, Natalya Ossina, Ronald C. McGlennen, Sharon Minnerath, John Borgos, Vadim Alexandrov, and Armen Sarvazyan. Protein Self-Organization Patterns in Dried Serum Reveal Changes in B-Cell Disorders. Molecular Diagnosis & Therapy, 10(6):371–380, November 2006.

[85] Hyoungsoo Kim, François Boulogne, Eujin Um, Ian Jacobi, Ernie Button, and Howard A. Stone. Controlled Uniform Coating from the Interplay of Marangoni Flows and Surface-Adsorbed Macromolecules. Physical Review Letters, 116(12):124501, March 2016.

[86] Ajeet Kumar and Chandra Kumar Dixit. Methods for characterization of nanoparticles. In Advances in Nanomedicine for the Delivery of Therapeutic Nucleic Acids, pages 43–58. Elsevier, 2017.

[87] Daniel M. Kuncicky and Orlin D. Velev. Surface-Guided Templating of Particle Assemblies Inside Drying Sessile Droplets $^{\dagger}$. Langmuir, 24(4):1371–1380, February 2008.

[88] Sang M. Kwark, Ratan Kumar, Gilberto Moreno, Jaisuk Yoo, and Seung M. You. Pool boiling characteristics of low concentration nanofluids. International Journal of Heat and Mass Transfer, 53(5-6):972–981, February 2010.

[89] Ralph I. Larsen. The Adhesion and Removal of Particles Attached to Air Filter Surfaces. American Industrial Hygiene Association Journal, 19(4):265–270, August 1958.

[90] H.H. Lee, S.C. Fu, C.Y. Tso, and Christopher Y.H. Chao. Study of residue patterns of aqueous nanofluid droplets with different particle sizes and concentrations on different substrates. International Journal of Heat and Mass Transfer, 105:230–236, February 2017.

[91] Shuying Li, Minmin Dong, Rui Li, Liyan Zhang, Yuchun Qiao, Yao Jiang, Wei Qi, and Hua Wang. A fluorometric microarray with ZnO substrate-enhanced fluorescence and suppressed "coffee-ring" effects for fluorescence immunoassays. Nanoscale, 7(44):18453–18458, 2015.

[92] Yanan Li, Qiang Yang, Mingzhu Li, and Yanlin Song. Rate-dependent interface capture beyond the coffee-ring effect. Scientific Reports, 6(1):24628, April 2016.

[93] Yanshen Li, Cunjing Lv, Zhaohan Li, David Quéré, and Quanshui Zheng. From coffee rings to coffee eyes. Soft Matter, 11(23):4669–4673, 2015.

[94] Yueh-Feng Li, Yu-Jane Sheng, and Heng-Kwong Tsao. Evaporation Stains: Suppressing the Coffee-Ring Effect by Contact Angle Hysteresis. Langmuir, 29(25):7802–7811, June 2013.

[95] Basavaraj Madivala, Steven Vandebril, Jan Fransaer, and Jan Vermant. Exploiting particle shape in solid stabilized emulsions. Soft Matter, 5(8):1717, 2009.

[96] I.M. Mahbubul. Stability and Dispersion Characterization of Nanofluid. In Preparation, Characterization, Properties and Application of Nanofluid, pages 47–112. Elsevier, 2019.

[97] I.M. Mahbubul, Elif Begum Elcioglu, R. Saidur, and M.A. Amalina. Optimization of ultrasonication period for better dispersion and stability of TiO2–water nanofluid. Ultrasonics Sonochemistry, 37:360–367, July 2017.

[98] Mainak Majumder, Clint S. Rendall, J. Alexander Eukel, James Y. L. Wang, Natnael Behabtu, Cary L. Pint, Tzu-Yu Liu, Alvin W. Orbaek, Francesca Mirri, Jaewook Nam, Andrew R. Barron, Robert H. Hauge, Howard K. Schmidt, and Matteo Pasquali. Overcoming the "Coffee-Stain" Effect by Compositional Marangoni-Flow-Assisted Drop-Drying. The Journal of Physical Chemistry B, 116(22):6536–6542, June 2012.

[99]  Selin Manukyan, Hans M. Sauer, Ilia V. Roisman, Kyle A. Baldwin, David J. Fairhurst, Haida Liang, Joachim Venzmer, and Cameron Tropea. Imaging internal flows in a drying sessile polymer dispersion drop using Spectral Radar Optical Coherence Tomography (SR-OCT). Journal of Colloid and Interface Science, 395:287–293, April 2013.

[100] Carlo Marangoni. Sul principio della viscosita' superficiale dei liquidi stabilito dalsig. J. Plateau. Il Nuovo Cimento (1869-1876), 5(1):239–273, December 1871.

[101] Antonin Marchand, Joost H. Weijs, Jacco H. Snoeijer, and Bruno Andreotti. Why is surface tension a force parallel to the interface? American Journal of Physics, 79(10):999–1008, October 2011.

[102] Alvaro Marin, Stefan Karpitschka, Diego Noguera-Marín, Miguel A. Cabrerizo-Vílchez, Massimiliano Rossi, Christian J. Kähler, and Miguel A. Rodríguez Valverde. Solutal Marangoni flow as the cause of ring stains from drying salty colloidal drops. Physical Review Fluids, 4(4):041601, April 2019.

[103] M. Mauermann, U. Eschenhagen, Th. Bley, and J.-P. Majschak. Surface modifications – Application potential for the reduction of cleaning costs in the food processing industry. Trends in Food Science & Technology, 20:S9–S15, January 2009.

[104] D. Maugis and H.M. Pollock. Surface forces, deformation and adherence at metal microcontacts. Acta Metallurgica, 32(9):1323–1334, September 1984.

[105] Daniel Maugis. Adhesion of spheres: The JKR-DMT transition using a dugdale model. Journal of Colloid and Interface Science, 150(1):243–269, April 1992.

[106] Ali Mazloomi Moqaddam, Dominique Derome, and Jan Carmeliet. Dynamics of Contact Line Pinning and Depinning of Droplets Evaporating on Microribs. Langmuir, 34(19):5635–5645, May 2018.

[107] F. Melo, J. F. Joanny, and S. Fauve. Fingering instability of spinning drops. Physical Review Letters, 63(18):1958–1961, October 1989.

[108] Maximilian Mittelviefhaus, Daniel B. Müller, Tomaso Zambelli, and Julia A. Vorholt. A modular atomic force microscopy approach reveals a large range of hydrophobic adhesion forces among bacterial members of the leaf microbiota. The ISME Journal, 13(7):1878–1882, July 2019.

[109] J. Ross Moffat, Khellil Sefiane, and Martin E. R. Shanahan. Effect of TiO $_2$ Nanoparticles on Contact Line Stick-Slip Behavior of Volatile Drops. The Journal of Physical Chemistry B, 113(26):8860–8866, July 2009.

[110] Cécile Monteux and François Lequeux. Packing and Sorting Colloids at the Contact Line of a Drying Drop. Langmuir, 27(6):2917–2922, March 2011.

[111] P.H. Mott, J.R. Dorgan, and C.M. Roland. The bulk modulus and Poisson's ratio of "incompressible" materials. Journal of Sound and Vibration, 312(4-5):572–575, May 2008.

[112] C T Nguyen, G Roy, N Galanis, and S Suiro. Heat Transfer Enhancement by using Al2O3-Water Nanofluid in a Liquid Cooling System for Microprocessors. Heat Transfer, Thermal Engineering and Environment, page 6, 2006.

[113] Shuichi Nosé and Fumiko Yonezawa. Isothermal–isobaric computer simulations of melting and crystallization of a Lennard-Jones system. Journal of Chemical Physics, 84:13, 1986.

[114] Harald F. Okorn-Schmidt, Frank Holsteyns, Alexander Lippert, David Mui, Mark Kawaguchi, Christiane Lechner, Philipp E. Frommhold, Till Nowak, Fabian Reuter, Miquel Banchs Piqué, Carlos Cairós, and Robert Mettin. Particle Cleaning Technologies to Meet Advanced Semiconductor Device Process Requirements. ECS Journal of Solid State Science and Technology, 3(1):N3069–N3080, 2014.

[115] Daniel Orejon, Khellil Sefiane, and Martin E. R. Shanahan. Stick–Slip of Evaporating Droplets: Substrate Hydrophobicity and Nanoparticle Concentration. Langmuir, 27(21):12834–12843, November 2011.

[116] F. M. Orr, L. E. Scriven, and A. P. Rivas. Pendular rings between solids: meniscus properties and capillary force. Journal of Fluid Mechanics, 67(4):723–742, February 1975.

[117] Kidong Park, Jaesung Jang, Daniel Irimia, Jennifer Sturgis, James Lee, J. Paul Robinson, Mehmet Toner, and Rashid Bashir. 'Living cantilever arrays' for characterization of mass of single live cells in fluids. Lab on a Chip, 8(7):1034, 2008.

[118] Maryam Parsa, Souad Harmand, Khellil Sefiane, Maxence Bigerelle, and Raphaël Deltombe. Effect of Substrate Temperature on Pattern Formation of Nanoparticles from Volatile Drops. Langmuir, 31(11):3354–3367, March 2015.

[119] Maryam Parsa, Souad Harmand, Khellil Sefiane, Maxence Bigerelle, and Raphaël Deltombe. Effect of Substrate Temperature on Pattern Formation of Bidispersed Particles from Volatile Drops. The Journal of Physical Chemistry B, 121(48):11002–11017, December 2017.

[120] V. Adrian Parsegian. Van der Waals Forces: A Handbook for Biologists, Chemists, Engineers, and Physicists. Cambridge University Press, 1 edition, November 2005.

[121] Nagesh D. Patil, Prathamesh G. Bange, Rajneesh Bhardwaj, and Atul Sharma. Effects of Substrate Heating and Wettability on Evaporation Dynamics and Deposition Patterns for a Sessile Water Droplet Containing Colloidal Particles. Langmuir, 32(45):11958–11972, November 2016.

[122] E. Pauliac-Vaujour, A. Stannard, C. P. Martin, M. O. Blunt, I. Notingher, P. J. Moriarty, I. Vancea, and U. Thiele. Fingering Instabilities in Dewetting Nanofluids. Physical Review Letters, 100(17):176102, April 2008.

[123] Emmanuelle Pauliac-Vaujour and Philip Moriarty. Meniscus-Mediated Organization of Colloidal Nanoparticles. The Journal of Physical Chemistry C, 111(44):16255–16260, November 2007.

[124] J. R. A. Pearson. On convection cells induced by surface tension. Journal of Fluid Mechanics, 4(5):489–500, September 1958.

[125] P.G.C. Petean and M.L. Aguiar. Determining the adhesion force between particles and rough surfaces. Powder Technology, 274:67–76, April 2015.

[126] R.G Picknett and R Bexon. The evaporation of sessile or pendant drops in still air. Journal of Colloid and Interface Science, 61(2):336–350, September 1977.

[127] Eva Potthoff, Dario Ossola, Tomaso Zambelli, and Julia A. Vorholt. Bacterial adhesion force quantification by fluidic force microscopy. Nanoscale, 7(9):4070–4079, 2015.

[128] Tapan Kumar Pradhan and Pradipta Kumar Panigrahi. Thermocapillary convection inside a stationary sessile water droplet on a horizontal surface with an imposed temperature gradient. Experiments in Fluids, 56(9):178, September 2015.

[129] Polina Prokopovich and Stefano Perni. Comparison of JKR- and DMT-based multi-asperity adhesion model: Theory and experiment. Colloids and Surfaces A: Physicochemical and Engineering Aspects, 383(1-3):95–101, June 2011.

[130] José L. Pérez-Díaz, Marco A. Álvarez Valenzuela, and Juan C. García-Prada. The effect of the partial pressure of water vapor on the surface tension of the liquid water–air interface. Journal of Colloid and Interface Science, 381(1):180–182, September 2012.

[131] M. B. Ranade. Adhesion and Removal of Fine Particles on Surfaces. Aerosol Science and Technology, 7(2):161–176, January 1987.

[132] Elizaveta Rapis. A change in the physical state of a nonequilibrium blood plasma protein film in patients with carcinoma. Soviet technical physics, 72(4):4, 2002.

[133] L. Richert, Ph. Lavalle, D. Vautier, B. Senger, J.-F. Stoltz, P. Schaaf, J.-C. Voegel, and C. Picart. Cell Interactions with Polyelectrolyte Multilayer Films. Biomacromolecules, 3(6):1170–1178, November 2002.

[134] D. S. Rimai and A. A. Busnaina. The adhesion and removal of particles from surfaces. Particulate Science and Technology, 13(3-4):249–270, July 1995.

[135] D. S. Rimai, L. P. DeMejo, and R. C. Bowen. Adhesion-induced deformations of polymeric substrates: Particle size dependence of the contact area. Journal of Applied Physics, 66(8):3574–3578, October 1989.

[136] D. S. Rimai, L. P. DeMejo, and R. C. Bowen. Surface-force-induced deformations of monodisperse polystyrene spheres on planar silicon substrates. Journal of Applied Physics, 68(12):6234–6240, December 1990.

[137] D.S. Rimai, R.S. Moore, R.C. Bowen, V.K. Smith, and P.E. Woodgate. Determination of the dependence of the surface force induced contact radius on particle radius: Cross-linked polystyrene spheres on SiO $_2$ /silicon. Journal of Materials Research, 8(3):662–667, March 1993.

[138] W. D. Ristenpart, P. G. Kim, C. Domingues, J. Wan, and H. A. Stone. Influence of Substrate Conductivity on Circulation Reversal in Evaporating Drops. Physical Review Letters, 99(23):234502, December 2007.

[139] T. Rouxel, H. Ji, T. Hammouda, and A. Moréac. Poisson's Ratio and the Densification of Glass under High Pressure. Physical Review Letters, 100(22):225501, June 2008.

[140] Lord Rayleigh Sec R.S. LII. On the theory of surface forces. The London, Edinburgh, and Dublin Philosophical Magazine and Journal of Science, 30(187):456–475, 1890.

[141] Seul-a Ryu, Jin Young Kim, So Youn Kim, and Byung Mook Weon. Drying-mediated patterns in colloid-polymer suspensions. Scientific Reports, page 7, 2017.

[142] G. Sagvolden, I. Giaever, E. O. Pettersen, and J. Feder. Cell adhesion force microscopy. Proceedings of the National Academy of Sciences, 96(2):471–476, January 1999.

[143] B Sakmann. Patch Clamp Techniques for Studying Ionic Channels in Excitable Membranes. Annual Review of Physiology, page 21, 1984.

[144] Bert Sakmann and Erwin Neher. Geometric Parameters of Pipettes and Membrane Patches. In Single-Channel Recording, page 14. Springer, 1995.

[145] Tatsuo Sato and Shigeru Kohnosu. Effect of surfactant concentration on the stability of aqueous titanium dioxide suspensions. Journal of Colloid and Interface Science, 143(2):434–439, May 1991.

[146] R. Savino, D. Paterna, and N. Favaloro. Buoyancy and Marangoni Effects in an Evaporating Drop. Journal of Thermophysics and Heat Transfer, 16(4):562–574, October 2002.

[147] Leonard W. Schwartz and Stephen Garoff. Contact angle hysteresis on heterogeneous surfaces. Langmuir, 1(2):219–230, March 1985.

[148] Khellil Sefiane. On the Formation of Regular Patterns from Drying Droplets and Their Potential Use for Bio-Medical Applications. Journal of Bionic Engineering, 7(S4):S82–S93, December 2010.

[149] S. Semenov, V. M. Starov, M. G. Velarde, and R. G. Rubio. Droplets evaporation: Problems and solutions. The European Physical Journal Special Topics, 197(1):265, August 2011.

[150] Wouter Sempels, Raf De Dier, Hideaki Mizuno, Johan Hofkens, and Jan Vermant. Auto-production of biosurfactants reverses the coffee ring effect in a bacterial system. Nature Communications, 4(1):1757, June 2013.

[151] Kwangseok Seo, Minyoung Kim, and Do Hyun Kim. Re-derivation of Young's Equation, Wenzel Equation, and Cassie-Baxter Equation Based on Energy Minimization. In Mahmood Aliofkhazraei, editor, Surface Energy. InTech, December 2015.

[152] Zhang Shi, Yi Zhang, Mingchao Liu, Dorian A.H. Hanaor, and Yixiang Gan. Dynamic contact angle hysteresis in liquid bridges. Colloids and Surfaces A: Physicochemical and Engineering Aspects, 555:365–371, October 2018.

[153] H. Sirringhaus, T. Kawase, R. H. Friend, T. Shimoda, M. Inbasekaran, W. Wu, and E. P. Woo. High-Resolution Inkjet Printing of All-Polymer Transistor Circuits. Science, 290(5499):2123–2126, December 2000.

[154] Marcel Sperling and Michael Gradzielski. Droplets, Evaporation and a Superhydrophobic Surface: Simple Tools for Guiding Colloidal Particles into Complex Materials. Gels, 3(15):27, May 2017.

[155] K.-L. Paul Sung, Michael K. Kwan, Fausto Maldonado, and Wayne H. Akeson. Adhesion Strength of Human Ligament Fibroblasts. Journal of Biomechanical Engineering, 116(3):237–242, August 1994.

[156] Kuo-Li Sung, Lanping A. Sung, Mary Crimmins, Steven J. Burakoff, and Shu Chien. Determination of Junction Avidity of Cytolytic T Cell and Target Cell. Science, 234(4782):1405–1408, December 1986.

[157] Annie Sénéchal, Shawn D. Carrigan, and Maryam Tabrizian. Probing Surface Adhesion Forces of *Enterococcus f aecalis* to Medical-Grade Polymers Using Atomic Force Microscopy. Langmuir, 20(10):4172–4177, May 2004.

[158] D Tabor. Surface Forces and Surface Interactions. SURFACE FORCES, page 12, 1976.

[159] David Tabor. On the role of molecular forces in contact deformations (Critical remarks concerning Dr. Tabor's report). Journal of Colloid and Interface Science, 67(2):380, 1978.

[160] Y. Taga. Recent progress in coating technology for surface modification of automotive glass. Journal of Non-Crystalline Solids, 218:335–341, September 1997.

[161] Francois Tardif, Adrien Danel, and Olivier Raccurt. Understanding of wet and alternative particle removal processes in microelectronics: theoretical capabilities and limitations. Journal of Telecommunications and Information Technology, page 9, 2005.

[162] Ashish Kumar Thokchom, Rajaram Swaminathan, and Anugrah Singh. Fluid Flow and Particle Dynamics Inside an Evaporating Droplet Containing Live Bacteria Displaying Chemotaxis. Langmuir, 30(41):12144–12153, October 2014.

[163] Ashish Kumar Thokchom, Qitao Zhou, Dong-Joo Kim, Dogyeong Ha, and Taesung Kim. Characterizing self-assembly and deposition behavior of nanoparticles in inkjet-printed evaporating droplets. Sensors and Actuators B: Chemical, 252:1063–1070, November 2017.

[164] Rostyslav Tykhoniuk, Jürgen Tomas, Stefan Luding, Michael Kappl, Lars Heim, and Hans-Jürgen Butt. Ultrafine cohesive powders: From interparticle contacts to continuum behaviour. Chemical Engineering Science, 62(11):2843–2864, June 2007.

[165] A Tözeren, K L Sung, L A Sung, M L Dustin, P Y Chan, T A Springer, and S Chien. Micromanipulation of adhesion of a Jurkat cell to a planar bilayer membrane containing lymphocyte function-associated antigen 3 molecules. Journal of Cell Biology, 116(4):997–1006, February 1992.

[166] K. Uno, K. Hayashi, T. Hayashi, K. Ito, and H. Kitano. Particle adsorption in evaporating droplets of polymer latex dispersions on hydrophilic and hydrophobic surfaces. Colloid & Polymer Science, 276(9):810–815, October 1998.

[167] T. G. van Kooten, J. M. Schakenraad, H. C. Van der Mei, and H. J. Busscher. Development and use of a parallel-plate flow chamber for studying cellular adhesion to solid surfaces. Journal of Biomedical Materials Research, 26(6):725–738, June 1992.

[168] I. Vancea, U. Thiele, E. Pauliac-Vaujour, A. Stannard, C. P. Martin, M. O. Blunt, and P. J. Moriarty. Front instabilities in evaporatively dewetting nanofluids. Physical Review E, 78(4):041601, October 2008.

[169] E. J. W. Verwey and J. Th. G. Overbeek. Theory of the stability of lyophobic colloids. The Journal of Physical and Colloid Chemistry, 1948.

[170] José M. Vicaria, Encarnación Jurado-Alameda, Otilia Herrera-Márquez, Vanessa Olivares-Arias, and Alejandro Ávila Sierra. Analysis of different protocols for the cleaning of corn starch adhering to stainless steel. Journal of Cleaner Production, 168:87–96, December 2017.

[171] J. Visser. On Hamaker constants: A comparison between Hamaker constants and Lifshitz-van der Waals constants. Advances in Colloid and Interface Science, 3(4):331–363, December 1972.

[172] FengChao Wang and HengAn Wu. Molecular origin of contact line stick-slip motion during droplet evaporation. Scientific Reports, 5(1):17521, December 2015.

[173] Robert N. Wenzel. Resistance of solid surfaces to wetting by water. Industrial & Engineering Chemistry, 28(8):988–994, August 1936.

[174] Byung Mook Weon and Jung Ho Je. Capillary force repels coffee-ring effect. Physical Review E, 82(1):015305, July 2010.

[175] Byung Mook Weon and Jung Ho Je. Fingering inside the coffee ring. Physical Review E, 87(1):013003, January 2013.

[176] Tak-Sing Wong, Ting-Hsuan Chen, Xiaoying Shen, and Chih-Ming Ho. Nanochromatography Driven by the Coffee Ring Effect. Analytical Chemistry, 83(6):1871–1873, March 2011.

[177] J. T. Woodward, H. Gwin, and D. K. Schwartz. Contact Angles on Surfaces with Mesoscopic Chemical Heterogeneity. Langmuir, 16(6):2957–2961, March 2000.

[178] Yugong Wu, Zhigang Fan, and Yuzhu Lu. Bulk and interior packing densities of random close packing of hard spheres. Journal of Materials Science, page 7, 2003.

[179] Hui Xu and Leah B. Casabianca. Probing driving forces for binding between nanoparticles and amino acids by saturation-transfer difference NMR. Scientific Reports, 10(1):12351, December 2020.

[180] T.A. Yakhno, V.G. Yakhno, A.G. Sanin, O.A. Sanina, A.S. Pelyushenko, N.A. Egorova, I.G. Terentiev, S.V. Smetanina, O.V. Korochkina, and E.V. Yashukova. The informative-capacity phenomenon of drying drops. IEEE Engineering in Medicine and Biology Magazine, 24(2):96–104, March 2005.

[181] Quansan Yang, Ye Gao, Feng He, and Pengfei Hao. Patterning in colloidal droplets by forced airflow. Journal of Applied Physics, 129(2):024701, January 2021.

[182] Ying Yang, Eric A. Grulke, Z. George Zhang, and Gefei Wu. Thermal and rheological properties of carbon nanotube-in-oil dispersions. Journal of Applied Physics, 99(11):114307, June 2006.

[183] Thomas Young. An Essay on the Cohesion of Fluids. Philosophical Transactions of the Royal Society of London, pages 65–87, 1805.

[184] Peter J. Yunker, Tim Still, Matthew A. Lohr, and A. G. Yodh. Suppression of the coffee-ring effect by shape-dependent capillary interactions. Nature, 476(7360):308–311, August 2011.

[185] Xuehua Zhang, Jun Wang, Lei Bao, Erik Dietrich, Roeland C. A. van der Veen, Shuhua Peng, James Friend, Harold J. W. Zandvliet, Leslie Yeo, and Detlef Lohse. Mixed mode of dissolving immersed nanodroplets at a solid–water interface. Soft Matter, 11(10):1889–1900, 2015.

[186] Xin Zhong, Alexandru Crivoi, and Fei Duan. Sessile nanofluid droplet drying. Advances in Colloid and Interface Science, 217:13–30, March 2015.